Politecnico di Torino

ScuDo
Scuola di Dottorato ~ Doctoral School
WHAT YOU ARE, TAKES YOU FAR

Doctoral Dissertation
Doctoral Program in Mechanical Engineering (35^{th}cycle)

An Inflatable Robotic Manipulator for Space Applications

By

Pierpaolo Palmieri

******

Supervisor(s):
Prof. Stefano Mauro

Doctoral Examination Committee:
Prof. Benedetto Allotta, Referee, Università degli Studi di Firenze
Prof. Pierluigi Beomonte Zobel, Referee, Università degli Studi de L'Aquila

Politecnico di Torino
2023

Declaration

I hereby declare that, the contents and organization of this dissertation constitute my own original work and does not compromise in any way the rights of third parties, including those relating to the security of personal data.

Pierpaolo Palmieri
2023

* This dissertation is presented in partial fulfillment of the requirements for **Ph.D. degree** in the Graduate School of Politecnico di Torino (ScuDo).

Abstract

The rapid growth of the space sector encourages the research of cost-effective solutions to execute an increasing number of missions. Specifically, in-space servicing, assembly and manufacturing (ISAM) and active debris removal (ADR) activities require advanced robotic systems, capable of performing complex tasks, such as maintenance of satellites or assembly and construction of large and complex space structures. This work introduces a novel deployable and lightweight robotic manipulator with inflatable links for space applications. This system can be stored in a relatively small volume and deployed when required. It can be withdrawn when its employment is not needed. This solution allows to limit the manipulator weight and size at launch, aiming to reduce costs. The hybrid architecture, which integrates rigid joints with conventional electrical actuation, enables the application of standard control methods for the robot. This work offers design procedures and models for the development of the robotic arm, with particular focus on the critical load conditions which cause the appearance of wrinkles and the structure collapse. Candidate materials suitable for space are discussed, underlining the necessity of high tensile strength capabilities for the inflatable links. The theoretical background regarding inflatable structures is applied for the development of models for the inflatable robotic arm, useful for design and simulation purposes. Two dynamic models for robot are examined to account for link flexible behavior: one introduces virtual joints following a lumped-parameter approach and the other one uses finite elements according to the Euler-Bernoulli theory. A robot prototype for laboratory testing has been developed, validating the concept, after analyses run on inflatable link prototypes. In the current development phase, the robot can be controlled using teleoperation, enabling future implementation of advanced automatic controls. Different control techniques are proposed, identifying in visual servoing the key methodology to perform accurate positioning of the robot. Finally, the proposed vision-based control algorithms are integrated in a virtual environment, using the developed dynamic models. The first

simulation represents the prototype reaching a target using the model based on virtual joints validating the visual servoing. Then, a space application is simulated: a large-size inflatable robot is mounted on a spacecraft and correctly grasps a space debris recurring to visual servoing strategies. This work demonstrates the feasibility of the proposed technology, defining design and modeling methods, developing the proof-of-concept, identifying suitable control strategies and providing virtual simulations of the system. Further steps, aimed to enhance the technology readiness level, are identified in the development, testing and validation of a new prototype with suitable space materials and in relevant environment.

Contents

List of Figures

List of Tables

Nomenclature

Roman Symbols

$\boldsymbol{D}$	Damping matrix
$\boldsymbol{e}$	Pose error vector
$\boldsymbol{G}$	Gain matrix
$\boldsymbol{J}$	Jacobian matrix
$\boldsymbol{K}$	Stiffness matrix
$\boldsymbol{p}$	Pose vector
$\boldsymbol{q}$	Robot variable vector
$\boldsymbol{R}$	Rotation matrix
$\boldsymbol{x}$	Position vector
c	Damping coefficient
E	Young's Modulus
G	Shear Modulus
I	Second moment of area
k	Stiffness coefficient
L	Link length
p	Pressure

r Link radius

S Cross-sectional area

t Link thickness

v Link vertical deflection

Greek Symbols

$\boldsymbol{\delta}$ Robot link angular deflection variable vector

$\boldsymbol{\phi}$ Orientation vector

$\boldsymbol{\tau}$ Joint torque vector

$\boldsymbol{\theta}$ Robot joint variable vector

ν Poisson ratio

Ω Region occupied by links

ζ Damping ratio

Subscripts

0 Pre-stressed reference configuration

$\varnothing$ Natural refrence configuration

Other Symbols

$\boldsymbol{J}^{\dagger}$ Right pseudo-inverse of Jacobian matrix

E_P Equivalent Young's modulus depending on pressure

f_n Un-damped natural frequency

f_s Damped natural frequency

G_P Equivalent shear modulus depending on pressure

I_M Moment of Inertia

M_c Collapse Moment

M_w Wrinkling Moment

Acronyms / Abbreviations

ADAM American able deployable articulated mast

ADR Active Debris Removal

AMM Assumed Mode Method

BEAM Bigelow Expandable Activity Module

CAN Controller Area Network

CLU Camera and Lighting Unit

CNN Convolutional Neural Network

CTE Coefficient of Thermal Expansion

DARPA Defense Advanced Research Projects Agency

DEOS Deutsche Orbital Servicing Mission

DOF Degree of Freedom

ECSS European Cooperation for Space Standardization

EE End-Effector

ERA European Robotic Arm

EVA Extra-Vehicular Activity

FBM Flexible Body Model

FEA Finite Element Analysis

FEM Finite Element Model

FOV Field of View

FREND Frontend Robotics Enabling Near-Term Demonstration

FSS Floating Spacecraft Simulators

GERS Gateway External Robotic System

GNC Guidance, Navigation and Control

IAE Inflatable Antenna Experiment

IMU Inertial Measurement Unit

ISAM In-space Servicing, Assembly and Manufacturing

ISS International Space Station

JEMRMS Japanese Experiment Module Remote Manipulator System

KF Kalman Filter

LEO Low Earth Orbit

LIFE Large Integrated Flexible Environment

MLI Multi-Layer Insulation

MMOD Micrometeoroids and Orbital Debris

MSS Mobile Servicing System

NRL Naval Research Laboratory

OOS On-Orbit Servicing

PBVS Position-Based Visual Servoing

PID Proportional-Integral-Derivative

PRBM Pseudo-Rigid Body Model

PSD Power Spectral Density

PT Pressure transducer

RBM Rigid Body Model

ROS Robot Operating System

RSO Resident Space Object

RV Reducing Valve

SMC Shape Memory Composite

SRMS Shuttle Remote Manipulator System

SSRMS Space Station Remote Manipulator System

TPS Thermal Protection System

TRL Technology Readiness Level

URDF Unified Robot Description Format

Chapter 1

Introduction

The present dissertation introduces a novel inflatable robotic manipulator for space applications. This robot, called POPUP, consists of inflatable links and electric motors, and can be compactly stored until deployment is necessary. This hybrid architecture provides a significant reduction in both volume and weight, still maintaining good payload capacity and reliable control as that of conventional solutions, if the internal pressure is set properly.

This chapter aims to provide an overview of the background in which the proposed technology is situated. In particular, an in-depth review of space robotic manipulators and inflatable structures is presented, since POPUP merges both technologies. Then, the concept of the inflatable robotic manipulator is introduced, outlining the project motivations, objectives and applications. Finally, the thesis structure is described.

1.1 Background

Space sector is rapidly growing in recent years due to changes in the global landscape that involves and empowers private companies [1]. "NewSpace" is an umbrella term for a movement, associated with the emergent private spaceflight industry, working to develop new space technologies and promote policies that make space more accessible, affordable and sustainable. Within the past 20 years, numerous new aerospace companies have emerged, covering diverse areas such as satellite communications, Earth observation, launchers, manned spaceflight and space tourism

[2]. An essential part of any space exploration and utilization program is robotics. In the space environment, that is hostile and partially known, space robotics is crucial to operate tirelessly and cost-effectively without endangering humans. Space robotic systems are key enabling technologies to execute space missions, and they are required for the maintenance of existing space infrastructures and the construction of new ones [3]. They an increasingly important role as technological progress continues in computing, control, space systems engineering, and robotic autonomy.

Space robotics can be divided into orbital robotics and planetary robotics. Orbital robotics is concerned with orbiting space robotics systems, as a satellite equipped with a robotic manipulator to allow grasping and manipulation of orbiting objects for servicing, assembly of space stations or other large structures, and removal of orbital debris. Planetary robotics is concerned with space robotic systems operating on the surface of an extraterrestrial body, as a vehicle landing on the Moon or Mars and releasing a robotic rover for the exploration of the environment, that can be equipped with a manipulator for the execution of tests [4]. In [5] the history and evolution of space robotics is recapitulated, reporting orbital and planetary robotic missions.

The growing importance of advanced robotics capabilities is a fact for on-orbit applications envisaged in the next decades, that will focus on space debris removal, rescue, planned orbit raising, inspection and support to deployment, deployment and assembly aid, repair, refueling and orbit maintenance, mission evolution and adaptation, lifetime extension, and re- and deorbiting. In particular, ISAM (In-space Servicing, Assembly and Manufacturing) is a key enabling technology for the future utilization of Low Earth Orbit (LEO) since inspection, repair, upgrade, and refueling of satellites in orbit are essential to prolong their operational life [6]. It also enables the modular assembly and construction of large and complex systems and artifacts in space. In literature, the term On-Orbit Servicing (OOS) indicates a subset of ISAM that focuses on the maintenance of space systems in orbit, including repair, assembly, refueling and/or upgrade of spacecraft. A complete review of space robotics for OOS is proposed in [7]. Moreover, in [3] a complete survey on guidance, navigation and control (GNC) methodologies of in-orbit space robotic system is presented.

In general, robots interact with other objects in the space by using actively controlled mechanisms that enable manipulation or mobility [4]. In the case of OOS, typically, the satellite has a propulsion system and a robotic arm to accomplish tasks.

After a spacecraft is deployed into its operative orbit, it becomes difficult to access and is at risk of becoming space debris if it experiences a failure or runs out of propellant. To address this issue, interest in the development of OOS missions has increased in recent years. OOS involves orbital activities conducted by a space vehicle that performs up-close inspections or beneficial changes to other resident space objects. These activities include non-contact support, orbit maintenance or modification, refuelling and resources replenishment, upgrade, repair, assembly, and debris removal. By servicing a satellite in orbit, its operational life can be extended, potentially providing a greater return on investment [8]. In [9] a review of structures, verification, and calibration technologies of space robotic systems for OOS is proposed.

In [10] a complete survey about robotic manipulation and capture in space is proposed. Autonomous robotic capture is a crucial technology for OOS, in particular for Active Debris Removal (ADR) missions [11]. However, controlling a spacecraft-mounted manipulator can be challenging as it creates disturbance torques on the satellite. To overcome this issue, various minimum reaction control strategies have been developed in literature to achieve the desired EE position while minimizing the dynamic disturbances that the robotic arm transfers to the spacecraft [12].

Establishing a telemetry connection from earth-based stations in real-time to orbital and deep-space spacecrafts is not always possible. As a result, autonomous robotic systems have become increasingly important in space missions. Intelligent and resilient robotic systems can make local decisions, reducing the need of teleoperation. Space manipulators have emerged as the most prominent autonomous robotic systems in space exploration and exploitation [7, 3].

1.1.1 Space Manipulators

Robotic manipulators are widely used devices for OOS missions. Since the deployment in 1981 of the first Shuttle Remote Manipulator System (SRMS), also known as Canadarm [13], several missions have used robotic manipulators to perform operations such as assembly, inspection, maintenance, capture of cooperative or non-cooperative objects such as space debris, repair, replacement of parts, refueling, berthing, extravehicular activity support [14].

Robotic arms can be large in size if developed for the execution of large-scale movements and manipulation of heavy payloads, especially for use on space stations. This category includes the aforementioned SRMS and its evolution, the Space Station Remote Manipulator System (SSRMS), also known as Canadarm2 [15], shown in Fig. 1.1 mounted on the International Space Station (ISS).

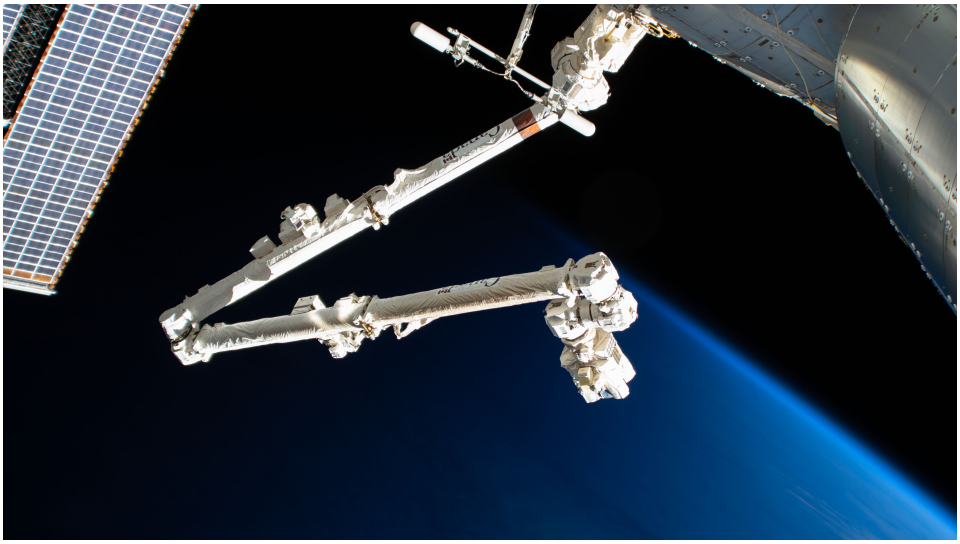

Fig. 1.1 The International Space Station's 57.7-foot-long robotic arm, also known as the Canadarm2, is pictured attached to the Harmony module as the orbital complex flies into an orbital sunrise above the Pacific Ocean. (credit: NASA)

The construction and operational needs of the ISS strongly promote the development of space robotic technology, where the following space manipulator systems have been tested: the Canadian Mobile Servicing System (MSS) launched in 2001, the Japanese Experiment Module Remote Manipulator System (JEMRMS) launched in 2008 and the European Robotic Arm (ERA) launched in 2021. In [16] a comparative study between these systems is proposed. The MSS is composed of three components: the aforementioned Canadarm2, the Mobile Remote Servicer Base System (MBS) and the Special Purpose Dexterous Manipulator (SPDM) also known as "Dextre" or "Canada hand" [17]. Canadarm2 has 7 degrees of freedom (DOFs), length of 17 m, mass of 1500 kg, diameter of 350 mm, speed of operation of 37 cm/s if unloaded, 2 cm/s during ground control and 15 cm/s during spacewalk support activities. It is controlled from the ground or by astronauts on the ISS and has four colour cameras: one on each side of the elbow and the other two on the end-effector (EE) [18]. The JEMRMS is composed of two arms, the Main Arm (MA) and the Small Fine Arm (SFA), having both 6 DOF. [19]. The main arm has length of 10

m, mass of 780 kg, handling capability of 7000 kg, maximum tip force of 30 N, position accuracy of 50 mm in position and 1.8 deg in orientation, speed in the range $2-6$ cm/s depending on the payload [20]. The ERA has two EEs which can act as a base, enabling either ends to be used as the shoulder. It has a length of over 11 m, 7 DOF, handling capability of 8000 kg, maximum speed of operation of 10 cm/s, accuracy of 5 mm and lauch mass of 630 kg. It has the ability to perform many tasks automatically or semi-automatically, can be directed either from inside or outside the Station, and it can be controlled in real time or preprogrammed. It is equipped with four Camera and Lighting Units (CLU) one on each EE and one on either side of the elbow [21].

The Gateway External Robotic System (GERS), also known as Canadarm3, is currently under development and will be installed on board the Lunar Gateway. It will be able to travel and bring tools to the entire length of the Lunar Gateway. It has 7 DOFs, length of 8.5 m, estimated mass of 715 kg, diameter of 23 cm, speed of operation of 10 cm/s when unloaded. It will be primarily controlled autonomously, however it can also be controlled from the ground or by astronauts on the Lunar Gateway [18].

Robotic manipulators can be used mounted on spacecrafts for the execution of assembly and servicing operations. They have smaller size with respect to the large manipulators used on ISS. In this category, the 2-m-long robotic arm mounted on the ETS-VII (Engineering Test Satellite No.7) [22], a satellite developed by the National Space Development Agency of Japan (NASDA) and launched in 1997, shown in Fig. 1.2. The robotic arm is tele-operated from ground and has 6 DOF, an end-effector and equipped with cameras on the first joint and on the end-effector.

In 2007, the Orbital Express mission by the Defense Advanced Research Projects Agency (DARPA) demonstrated that a robotic spacecraft could safely and cost-effectively service a satellite while on-orbit, using a 6-DOF robotic arm [23]. Other example of robotic manipulators for spacecrafts are: the Frontend Robotics Enabling Near-Term Demonstration (FREND) [24], the arm of the Phoenix program developed by the DARPA and Naval Research Laboratory (NRL) currently under testing [25] and the arm developed by the German space agency DLR for the Deutsche Orbital Servicing Mission (DEOS) [26], a mission which was later cancelled after the definition phase, that would have employed two satellites and launched in 2018. On-orbit Servicing, Assembly, and Manufacturing 1 (OSAM-1) is a robotic spacecraft

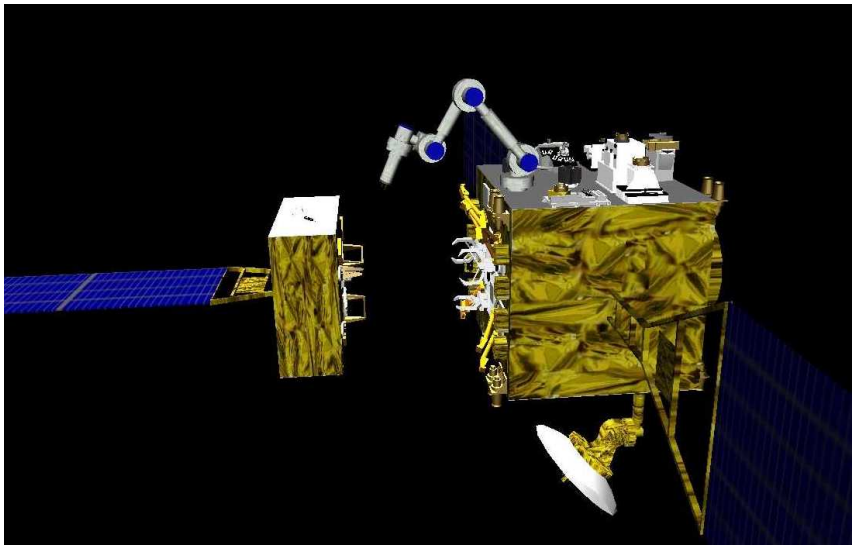

Fig. 1.2 Computer graphics simulation for the target capture by the manipulator arm by integrating technologies verified by ETS-VII. (credit: Space Robotics Laboratory, Tohoku University)

that has completed its critical review in 2022 [27]. The spacecraft is equipped with the Space Infrastructure Dexterous Robot (SPIDER) that includes a 5-meter robotic arm. The mission plans the assembly of a large 3-meter communications antenna, as shown in Fig. 1.3 [28].

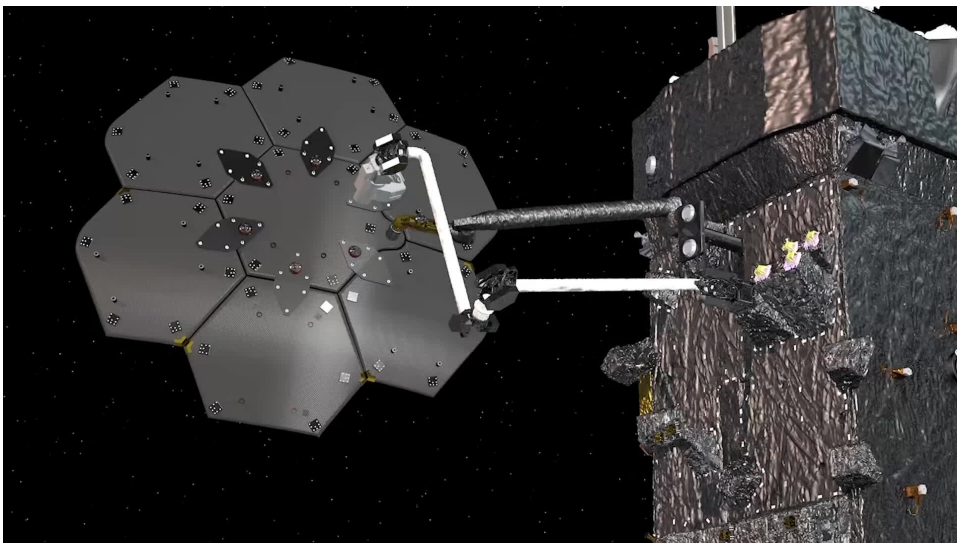

Fig. 1.3 SPIDER will demonstrate in-orbit assembly of an antenna. Credit: Maxar Technologies.

The verification and validation of space robots on the ground is a challenging task since they are designed for the space environment. As such, it is difficult to perform physical tests to verify all operating conditions under the standard gravitational conditions. Furthermore, the coupling effect of multiple environmental factors, such as vacuum, microgravity, low gravity, high and low temperatures, and other on-orbit conditions, is difficult to replicate on Earth. Different approaches can be considered to emulate zero-gravity conditions for the development of robotic system for OOS missions. They include air-baering supported floating, parabolic flight, free fall, force compensation, hardware-in-the-loop systems. However, the most commonly used technology for emulating zero-gravity is to use an air-bearing based floating test facility [7]. An example is shown in Fig. 1.4, where the air bearing test bed consists of a smooth and horizontally leveled 4-by-4 meter granite table and multiple Floating Spacecraft Simulators (FSS) [29].

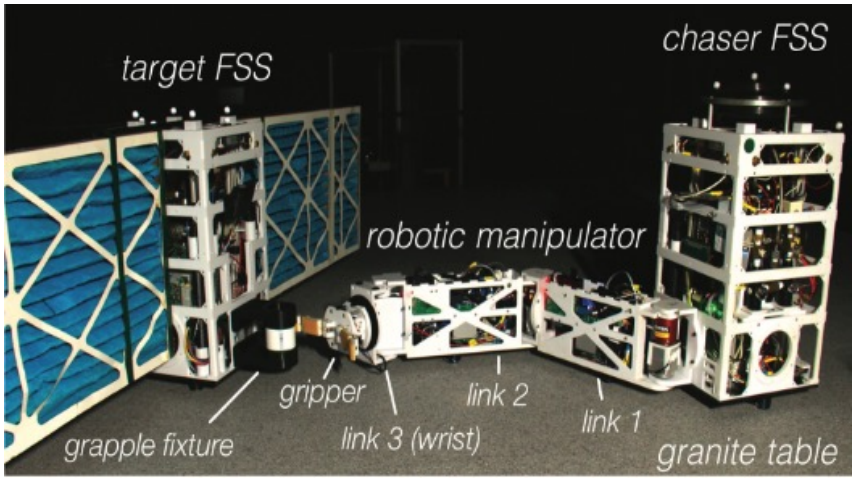

Fig. 1.4 Floating Spacecraft Simulators used during the experiments at the Spacecraft Robotics Laboratory POSEIDYN planar air bearing test bed of the Naval Postgraduate School.

1.1.2 Deployable structures

Deployable structures are used in several applications, from space structures to temporary architecture and medical devices [30]. Since the launchers' capability is a major constraint in spacecraft design, the employment of deployable structures allows to overcome constraints in size and mass.

In [31] a detailed analysis of gossamer structures is presented. The term gossamer structure is used to indicate the category of space ultra-low-mass structures, such as inflatables or other form of expandables. Gossamer technologies have been applied in inflatable and rigidable solar array [32], the Mars Pathfinder inflatable airbag landing system [33], and modular inflatable membranes of James Webb Space Telescope [34]. One of the first relevant projects using inflatable booms was the Inflatable Antenna Experiment (IAE) [35], that remained inflated in orbit for ten years proving the feasibility and reliability of the project. However it showed criticality during the deployment related to the post-deployment stability.

Inflatable habitats, are suitable for several applications, from modules on the ISS to planetary system on Lunar or Mars surface. TransHab, short for Transit Habitation Vehicle, was a concept pursued by NASA for an inflatable habitat for the replacement of an existing ISS crew module [36]. Subsequently, NASA and Bigelow Aerospace have successfully tested the Bigelow Expandable Activity Module (BEAM) attached to the International Space Station in 2016, as shown in Fig. 1.5, with a inflatable restraint layer composed of Kevlar. Sierra Space is developing LIFE (Large Integrated Flexible Environment), where inflatable pressure shell layer is composed of Vectran fabric weave. It is designed to support LEO applications and for long-duration missions, including Lunar and Mars surface habitation [37].

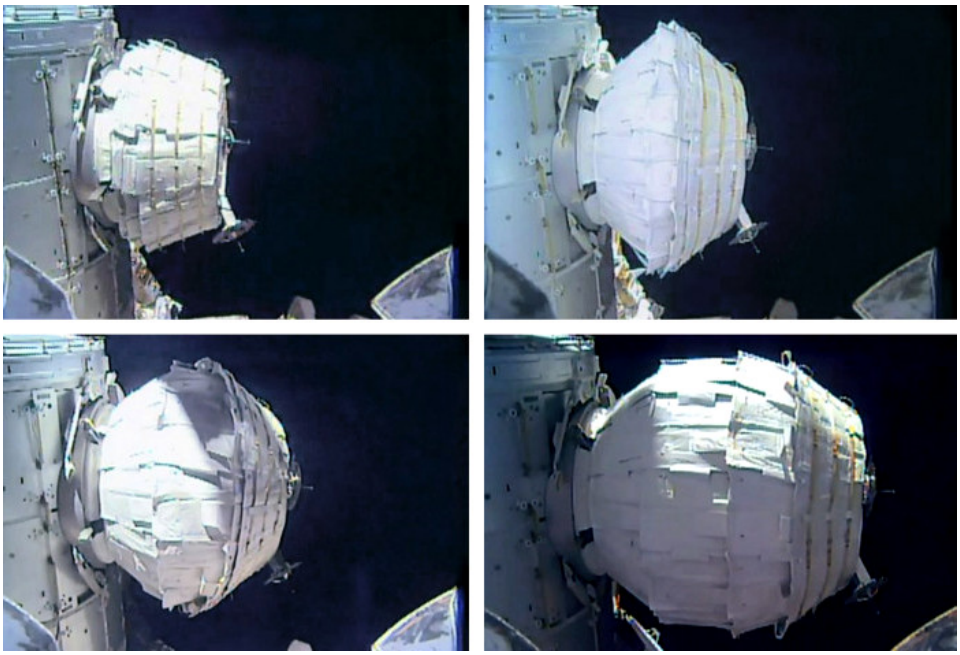

Fig. 1.5 BEAM expansion progress. Credit: NASA.

Deployable booms can be classified depending on the deployment technology used. Inflatable and rigidable booms have the advantage of being extremely lightweight with a great packaging ratio, defined as the deflated structure volume divided by the inflated structure volume, that can reach 1/45. However, they generally have relatively low deployment accuracy and post-deployment stability. Telescopic booms are typically much stiffer than most other deployable solutions, besides being more precise and stable, but they are heavier and have a low packaging ratio. Shape memory composite (SMC) booms cannot deploy heavy structure, and have relatively low deployment accuracy and post-deployment stability. Articulated booms include space manipulators and are used in several missions as already described. Deployable truss structures provide several degrees of freedom for storage and deployment of the structure itself, using pinned joints instead of rigid joints: in this category the American able deployable articulated mast (ADAM) has been flight proven for extensions up to 60 m. Finally, coilable booms were designed for applications up to 100 m, working on the principles of full length longerons coiled as springs in the stowed configuration [38]. Based on studies shown in [38], limited to existing technologies in 2010, a comparison between the described technologies is shown in Fig. 1.6 considering packaging ratio, boom mass and boom diameter.

In general, inflatable booms show great performance in relation to articulated structures, being able to ensure same deployable length and adding advantages in terms of mass and packaging ratio. Moreover inflatable boom can have similar diameter and overall size. This aspect is crucial in the following dissertation, since allows to imagine a space manipulator having as link inflatable booms in order to meet the advantages of both the technologies.

1.1.3 Foldable and Soft Robots

In [39] future prospects of space robotics are investigated. Soft robots are a novel kind of robot that has lightweight, high adaptability to the target shape and low collision force with the environment. Some of the potential space applications of soft robots can be:

- adaptive capture of space target, such as space debris and failed satellites, especially rotating ones, with less demand for target measurement accuracy

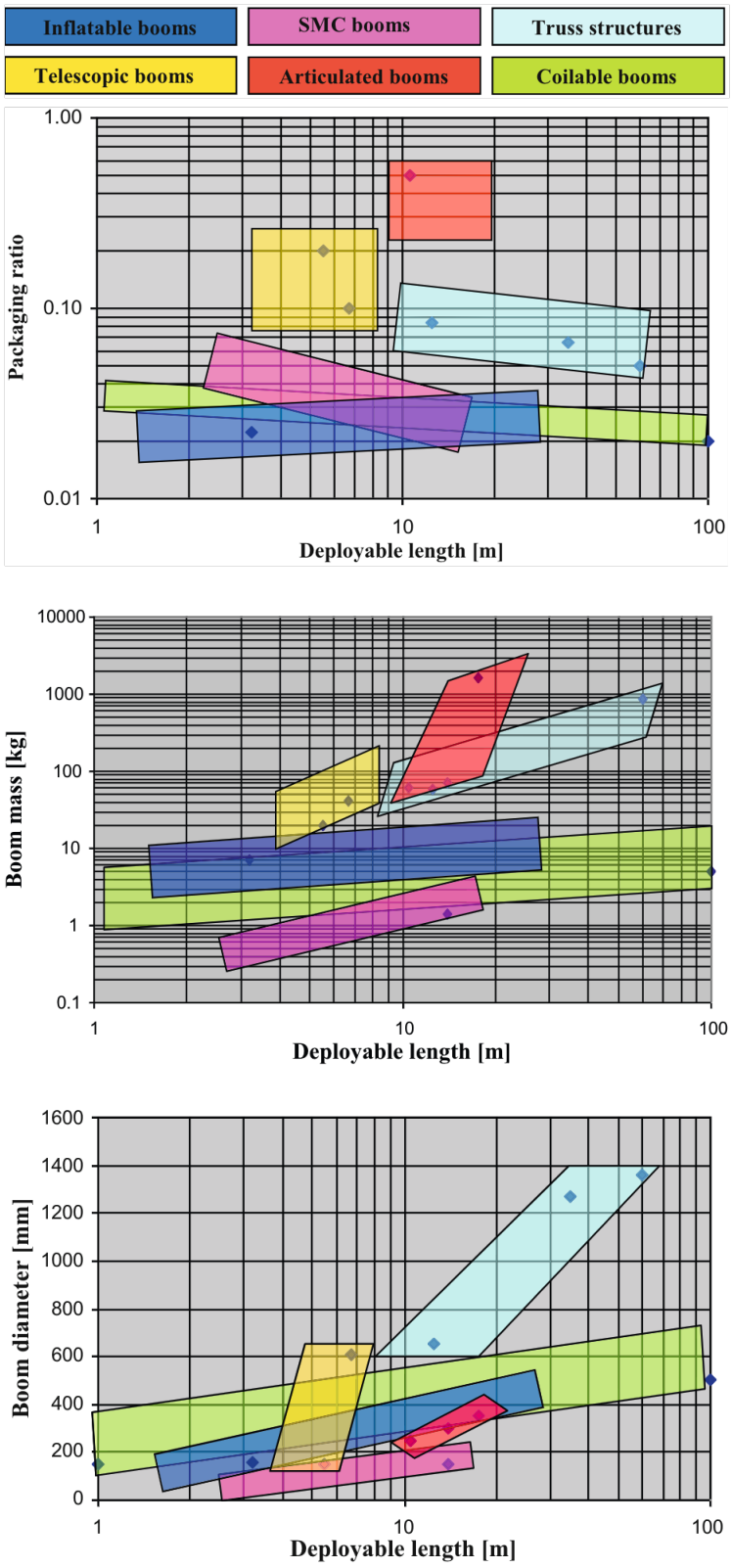

Fig. 1.6 Deployable boom comparison: deployable length versus packaging ratio, boom mass and boom diameter. Credit: L. Puig et al.

and less impact load during the capture process, thus ensuring operational safety;

- narrow space operations, performing tasks such as spacecraft maintenance and space station module operation, which involve constraints such as limited operating space and large equipment interference that may result in equipment damage;

- long-distance handling of space facilities. Space is a microgravity environment, where the robot only needs to overcome the inertial force when handling objects. Therefore, using large-sized soft robots for long-distance handling of objects can be more cost-effective and efficient.

However, completely soft robots have the drawback of producing low forces and low precision, compared to traditional robots, due to having many degrees of freedom and high structural compliance [40].

As a subdomain of soft robots, inflatable robotic arms (IRAs) concepts have been developed using pneumatic actuation [41–43]. The main advantage of this type of actuation is that it can enhance the safety of human-robot interaction (HRI) by reducing the impact force in case of collision [43]. This is especially important for middle-sized IRAs that work closely with humans. Large-scale IRAs have been developed for the inspection of sensitive environments [44]. For on-board space applications, an inflatable humanoid robot has been developed [45] by Brigham Young University with the support of NASA. However, the pneumatic actuation has drawbacks, such as the complexity of the control system, that results in additional weight due to the hardware required for the pneumatic plant. Moreover, these systems share the same limitations of completely soft robots, such as low precision and low force exertion. A small-size robotic manipulator that combines inflatable links with electric motors has been proposed in [46]. In this concept, the stiffness-controllable links are made of low elastic modulus material to offer a compliant behavior for HRI. Even in this case, a complex pneumatic control is implemented.

Modular deployable and foldable robots, also known as robogami, represent another relevant trend especially for space applications [47]. These robots are composed of flat sheets of material that can fold into complex shapes and perform various tasks. However, they have different features in relation with the proposed concept.

1.2 POPUP Concept

This thesis discloses POPUP, a deployable and lightweight robotic arm for space applications, consisting in inflatable links and rigid electric-actuated joints. The concept is shown in Fig. 1.7. It can be stored in a relative small package and deployed when required, guaranteeing weight and volume savings. This feature is relevant for space applications, where it leads to reduced costs. The robot, appropriately packed, is also more resistant by its nature than a traditional rigid solution to the stresses of launch. Mass savings are guaranteed by using of high-specific strength materials for the inflatable links, such as Vectran™ or Kevlar™. The use of a traditional layout, with joints actuated by electric motors, facilitates the design of the robot, which can be configured and sized according to the mission requirements, and allows to adapt traditional control laws to the novel inflatable robot. The number of total DOFs depends on the mission: both 6 and 7 DOFs can be considered. It includes build-in sensors to enhance and facilitate the system control.

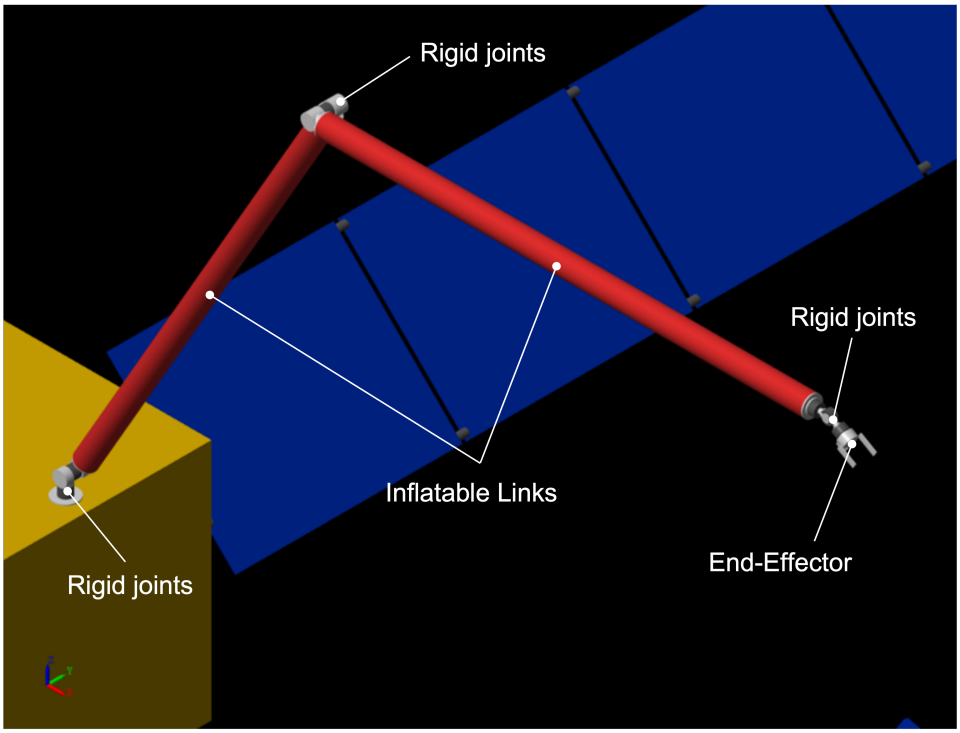

Fig. 1.7 Render of POPUP concept in off-board application.

1.2.1 Project Objectives and Applications

The robot is mainly designed for off-board applications, in particular for ISAM and debris removal missions. In this context, the project purpose is the development of a robotic manipulator with large inflatable links. The robot architecture is intended to be comparable to other space robotic manipulator, e.g., Canadarm [13], having two links longer than the other ones, and able to reach 6 DOFs or more adding suitable joints. This concept is based on the idea of having the two long links inflatable, since they represent the majority of volume occupied by the robot. Robots with inflatable links lead to a cost-effective solution for space missions, because of weight and volume savings.

In contrast with other inflatable robotic arms with pneumatic actuation, the use of traditional electric motors allows us to have simpler control and lower size of the pneumatic line. For POPUP robot, link inflation and deflation are an ON/OFF process with simple pneumatic control. Moreover, several inflation cycles can be performed. The air supply can be provided by a pressurized tank in composite materials having limited dimensions with respect to the robot. As an example, the dimensions of the first version of Canadarm robot embedded on the Space Shuttle [13], indicated in the following as Canadarm1, are taken as reference: assuming link length of 6 m, link radius of 165 mm, inner pressure of 100 kPa and tank pressure of 30 MPa, the tank volume per inflation cycle is 4 dm^3, that is, less than 0.4% of total robot volume. Finally, advantages in terms of volume savings grow with the increase of ratio of link lengths to joint sizes. For example, assuming a reduction of 75% of link volume when deflated, the overall volume savings would be of 60% for a POPUP with the structure of a Canadarm1, reducing the volume from 1.3 m^3 to 0.5 m^3.

The design parameter for link sizing is the wrinkling moment, that is, the bending load for which the first wrinkles appear on the link, resulting in non-linear behavior of the inflatable beam. Wrinkling moment formulations, further discussed in Section 2.3.1, allow preliminary analysis about dimensions, payload and pressure used during the operative stage of the robot when deployed. As an example, taking again as reference the Canadarm1 dimensions, assuming inner pressure of 100 kPa and neglecting robot inertia, POPUP could support 40 N of load applied on the end-effector (EE) without showing wrinkles, that means moving a the same payload of Canadarm1 of 15000 kg at 0.0025 m/s^2 in the space. Since inner pressure is

proportional to the achievable payload, it can be properly tuned according to the application.

A link of the Canadarm has a mass of 23 kg, while a link of the POPUP with same dimensions has a mass of about 3 kg [48]. This estimate considers the mass of a bladder layer and a structural layer made in Kevlar™. The mass saving is about 20 kg per link, for a total of 40 kg. Considering that a launch with the Vega launcher [49] has an estimated cost of 20 k$/kg [50], the economic saving would be about 800 k$. These values, appropriately scaled, can also be found for the launch of smaller arms.

The robot can be also used in onboard applications, where a soft collaborative robot can help the crew in its tasks [51]. In this case, the main advantage is the possibility of being closed and packed, as it would allow an optimal management of the limited space available inside the environment. Moreover, robots with intrinsic soft structure can improve safety in the event of an undesired collision and the use of low-pressure compressed air is common, for example, inside the ISS.

Finally, the possibility of obtaining payloads of 1–5 kg on Earth allows to consider the use of the robot in manipulation activities to be carried out on the Moon ($g = 1.62\ m/s^2$), on Mars ($g = 3.71\ m/s^2$) or on asteroids. Even in this case, the main advantage is weight and volume saving at launch.

1.2.2 Project Planning and TRL

The thesis activities are planned along two parallel paths, illustrated in Fig. 1.8. The design, modeling and control path is supported by the experimental part focused on the construction of a first robot prototype. After studying the basic principles of inflatable structures and defining the robot concept, the prototyping activities began producing link prototypes. This led to improvement in the prototype realization and the static and dynamic characterization of the inflatable links, confirming theoretical principles. CAD design and dynamic models were produced aiming for the design of a first robot prototype. Control techniques were studied and validated using the developed dynamic models, identifying the visual servoing as a solution. A teleoperation control is implemented and visual servoing control is currently under implementation. Finally, the simulation of a space application is proposed.

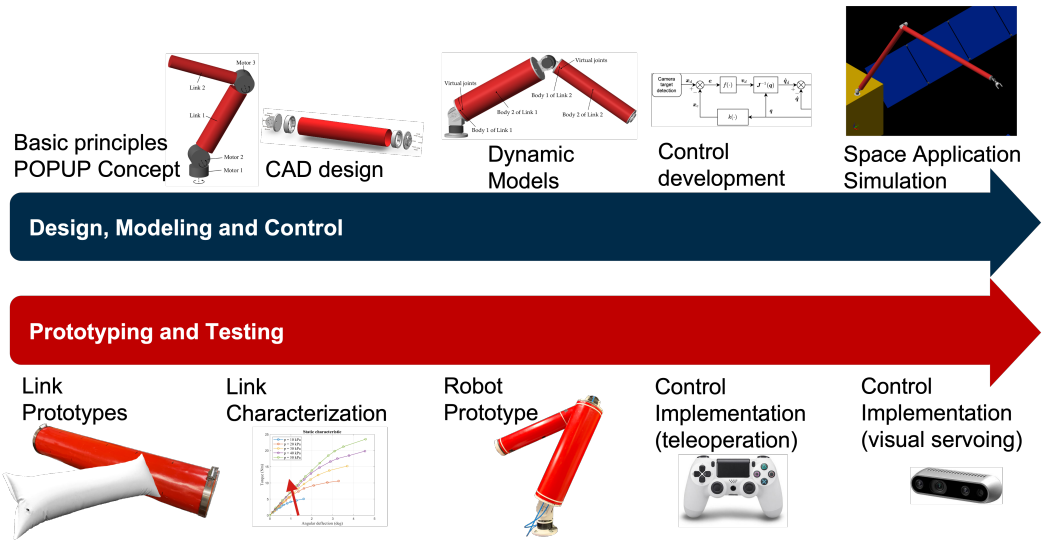

Fig. 1.8 Work plan.

This work thesis allowed to reach a TRL (Technology Readiness Level) between 3 and 4, that implies the realization of proof-of-concept and functional verification of the main components of the system. Technology Readiness Levels are different points on a scale used to measure the progress or maturity level of a technology. ESA uses the ISO 16290 TRL Scale, reported in a simplified version in Fig. 1.9.

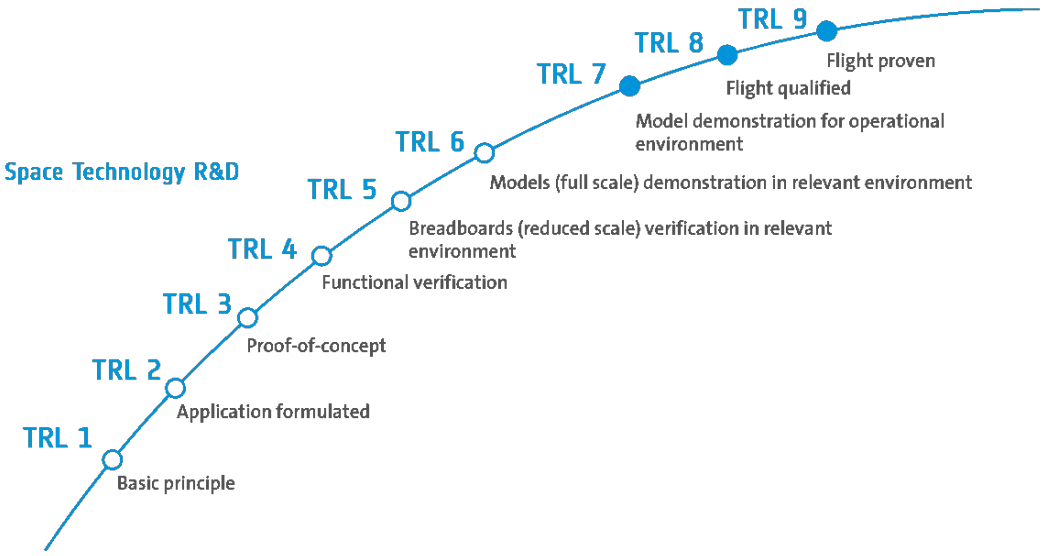

Fig. 1.9 Technology Readiness Level (TRL) scale levels applied to ESA's Technology Programmes. Credit: ESA.

Further information and guidelines are available in [52] thought the European Cooperation for Space Standardization (ECSS), a collaborative initiative of the European Space Agency, national space agencies and European industry associations that aims to create and maintain common standards. It provides documents intended to be used in space projects and applications as supporting material for ECSS Standards.

After this thesis work, the project has to increase the TRL by conducting further tests on the robot prototype, constructing it with materials for space, implementing advanced control algorithms, validating the deployment. Moreover, a new prototype for the execution of tests in relevant environment, testing movements in microgravity and performing tests in vacuum and high/low temperature conditions, will enable reaching TRL 6.

1.3 Overview of the thesis structure

The dissertation is divided in the following chapters.

Chapter 2 focuses on the design and modeling of the inflatable links and the robotic system. The chapter begins with the description of the inflatable robot, followed by a discussion on the space material selection and layer features. Then, the chapter delves into the theoretical analysis of inflatable beams with particular emphasis on collapse conditions, leading to the development of a set of design procedures for robot sizing for the intended application. Finally, different models are proposed to describe the dynamic behavior of the inflatable robot. These models include lumped parameter models, which are useful for obtaining simplified solutions to the system dynamics, and finite element models, which are more accurate but require more computational resources.

Chapter 3 presents the development of the proof of concept for the inflatable robotic manipulator. It covers the design and manufacturing of the inflatable links, which are made of polymeric materials to demonstrate the feasibility of the project and the validity of the theoretical models from the previous chapter. The inflatable links are then combined with rigid joints to form the robotic arm, and a teleoperated control scheme is implemented for initial testing. The sensorization and control

strategies for the manipulator are discussed, and the future steps for developing a micro-gravity test bench are mentioned.

Chapter 4 explores the control techniques for the robot with inflatable links. It examines the methods based on elastostatic models and link state estimation, and introduces the visual servoing as the main method for controlling the robot. Dynamic models are developed and used for the validation of the control. Finally, a space application is simulated where the robot with 7 DOFs is mounted on a spacecraft and grasps a debris using visual servoing. The results demonstrate the suitability and effectiveness of the control strategy for the inflatable robot and its readiness for prototype implementation.

Chapter 5 concludes the work by summarizing the main contributions and significance of the project, addressing the limitations and challenges, and highlighting future works and developments.

Chapter 2

Design and Modeling

This chapter intends to present design and modeling methods for the inflatable robot. The robotic system concept is concisely described, discussing the pneumatic line, deployment strategies and providing an analysis concerning the materials and layers to be used for the inflatable links. The theoretical background of inflatable beams is employed to derive models appropriate for inflatable links, that are integrated in the dynamic model of the robot. Theoretical formulations regarding the collapse of the inflatable links are presented and used for design purpose.

2.1 Robotic System Concept

The robot consists in two inflatable links and rigid revolute joints actuated by electric motors. A render of a 6 DOF robotic arm in its the extended configuration, mounted on a spacecraft, and with a grasping tool is shown in Fig. 2.1.

The critical and distinctive part of the project are the inflatable links, that are the main topic of this chapter. The links have cylindrical shape and are made of a soft materials fixed to rigid cups that are connected to the joints. They are designed according to considerations discussed in Section 2.3 about the influence of the internal pressure and size on the performances.

The joints consist of a rigid part, that includes the motors. Rigid parts can be manufactured in composite materials to minimize weight and guarantee load resistance. As an example, graphite-epoxy can be used as for Canadarm links [48].

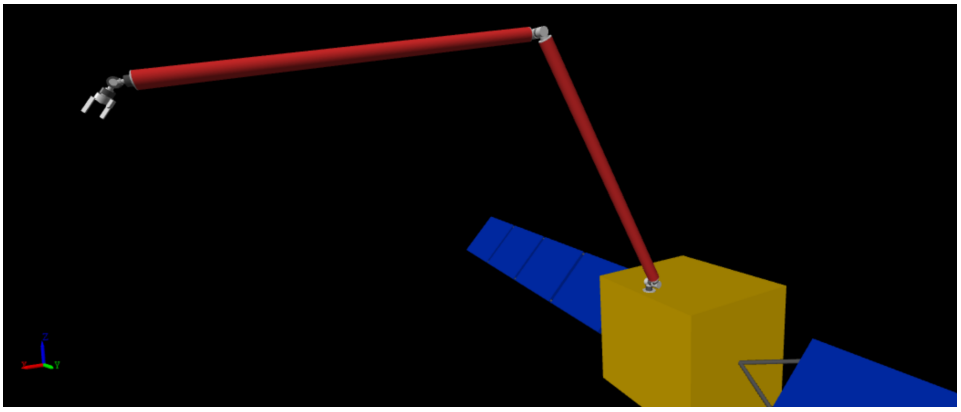

Fig. 2.1 Render of the inflatable robot in the space mounted on a spacecraft.

The system includes a pneumatic line, responsible of the deployment and withdrawal phases. Once reached the deployed configuration, the pneumatic supply is cut off and the robot is ready for the working phase. The pneumatic line and the deployment strategies are briefly discussed in the following.

2.1.1 Pneumatic line

A pneumatic line is designed to control the inflation and deflation stages [53]. It consists in a pressurized tank, a reducing valve and two digital valves for each link. Pressure gauges are expected to be positioned in critical points, e.g., the tank, after the reducing valve and inside the links. The system is schematized in Fig. 2.2.

The tank should be made of composite materials to reduce its weight. Commercial rigid tanks can reach pressure of $p_S = 30$ MPa. However, ESA is currently developing SISTEM (Small Inflatable Space Tank Engineering Model), an inflatable 13 litre tank for storage of gas and cryogenic liquids. The advantage is to provide low mass and volume solution, reaching pressure of $p_S = 6$ MPa [54]. This confirm the trend of researching inflatable solutions for the space.

Since links can show acceptable performance when pressure is higher than 10 kPa and the tank pressure is $p_S = 30$ MPa, the tank bulk is limited in relation to the dimension of the robot. In Section 1.2, an example is presented considering Canadarm dimensions. Additional details about the influence of pressure are provided in Section 2.3.

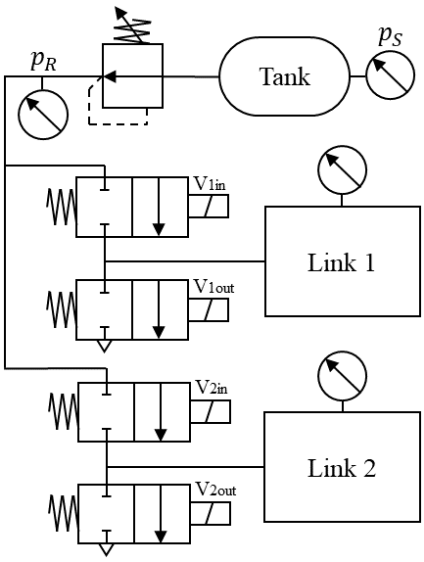

Fig. 2.2 Scheme of the pneumatic line, consisting of tank, reducing valve, four digital normally closed valves, pressure gauges and links.

The pressure p_S of the tank is regulated by a pressure reducing valve to the desired value p_R for the links. Moreover, having no requirements about the time needed for the inflation and deflation stages, small dimension digital valves can be selected. The valves are normally closed to ensure energy savings, as they are active only during the deployment or deflation phase. Each link is connected with a couple of valves. These valves allow the links to be isolated from the pneumatic line, inflated or deflated independently. As clarified in Fig. 2.2, the nomenclature, e.g., V_{1in}, of the valves allows to identify the link they are referred to (1 or 2) and the role they have when activated: "in" if they permit the inflation and "out" the deflation.

2.1.2 Deployment system

In literature, different packing techniques for space inflatable booms are proposed [55]. A common stowage method is coiling and wrapping: the uninflated boom is flattened before rolled into a coil or wrapped around a hub. Other category of methods is to use fold patterns. The simplest folding pattern is the z-fold, or zigzag: the 28-m-long booms of the IAE [35] were folded this way before flight testing. There is a number of folding schemes based on origami patters that allow rapid inflation and compact stowage. Lastly, the conical fold allows controlled and straight deployment and a load-bearing capacity during deployment.

Challenges include precise, controlled, predictable deployment and post-deployment stability of the booms. In literature, different studies are proposed: for example, in [56] the free inflation deployment dynamics of an inflatable tube is discussed and in [57] a deployment study of a 3-m-long inflatable boom made of carbon and Vectran™ is discussed.

The presented folding and packing techniques were developed specifically for inflatable booms. The challenge of having controlled deployment is significant in the case of a robot with inflatable links. The system has to be deployed and withdrawn in a regulated and reliable manner. It have to be simulated and verified on the ground, prior to operation in space. For this purpose, two deployment strategies are developed for POPUP. One strategy consists in a mechanical system under patent application and is therefore not disclosed in this work. The other strategy is inspired by wrapping methods and is proposed here for off-board applications.

The robotic system is stowed in a small box when the links are in the deflated configuration. Fig. 2.3 illustrates the stages of the deployment and withdrawing phases, considering a 3-DOF manipulator, without showing the wrist and end-effector. Fig. 2.3a shows the robotic system stowed in a small box with the links in the deflated configuration, and Fig. 2.3c shows the robot in its operational configuration.

Due to the flexibility of the materials, the links could be wrapped around the axis of the joint. Referring to the pneumatic line proposed in Fig. 2.2, the deployment of the robot consists of the following phases:

- in the starting configuration (Fig. 2.3a), link 1 and link 2 are deflated and wound around the shafts of joint 2 and joint 3, respectively;
- the link 2 is unrolled through the action of the motor of the joint 3, and it is inflated with the air supply, activating the valve V2in, to assume the deployed form (Fig. 2.3b);
- the link 1 is unwound utilizing the motor 2 and inflated (Fig. 2.3c), commuting the valve V_{1in}.

After the deployment phase, the robot reaches its working configuration (Fig. 2.3c). When the withdrawing of the robot is necessary, the following steps are expected:

- the link 2 is deflated, through the commutation of the valve V_{2out}, and rolled around the shaft of the joint by using the motor 3 (Fig. 2.3d);

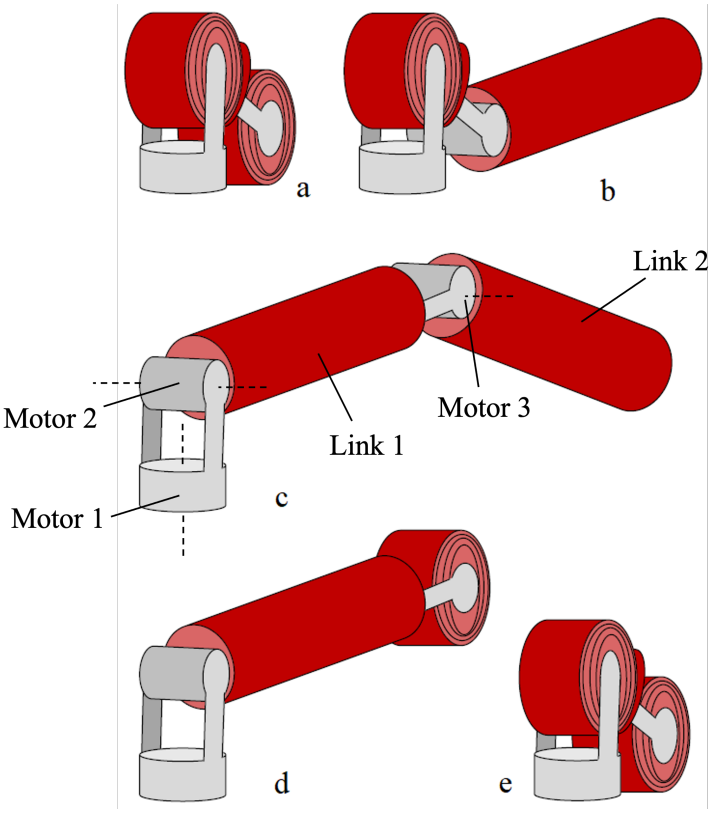

Fig. 2.3 Scheme of the stages for the deployment and withdrawing phases. a) deflated and withdrawn configuration of the robot before inflation; b) first stage of the inflation phase; c) deployed configuration; d) first stage of the withdrawing phase; e) deflated and withdrawn configuration after deflation.

- the link 1 is deflated activating the valve V_{1out}, and rolled around the shaft through the motor 2 (Fig. 2.3e).

The robot comes back to its starting configuration and can be stored in the box. The motors that enable to wind and unwind the links around the shaft are the same used for controlling the robotic arm.

For on-board applications, the withdrawal phase can be aided by the crew using a folding method, e.g., z-folding, in order to achieve a system with higher packaging ratio.

2.2 Material Selection and Layers

This section aims to identify the potential materials and layers to be employed in the final design of the inflatable links. For off-board applications, the most analogous systems to the proposed solution are the inflatable habitats. Hence, these systems serve as a reference for the construction of the inflatable links.

The shell assembly of inflatable habitats is composed of five primary layers including liner layer, bladder layer, restraint layer, micrometeoroid/orbital debris (MMOD) protection layer, and thermal protection layer [36, 58], as shown in Fig. 2.4 [59].

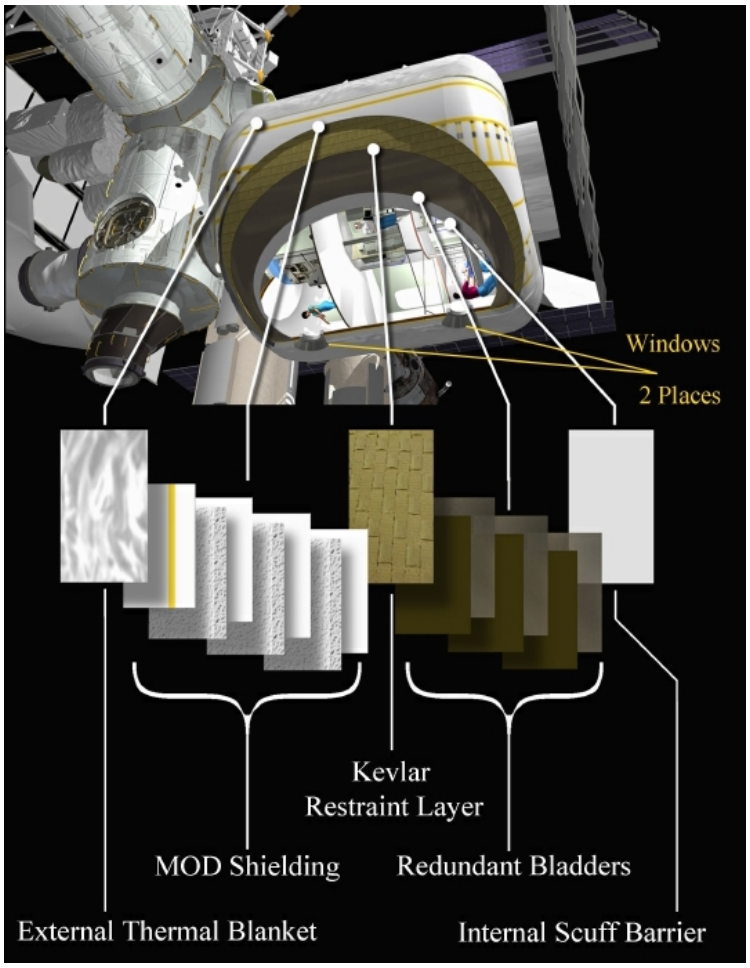

Fig. 2.4 Cutaway of the TransHab Module shell showing the various layers. Credit: NASA.

The liner layer shields the bladder from any damage caused by the crew and to offer a resilient and simple-to-clean surface for human touch. This layer is not required for the inflatable links.

The bladder layer contains the internal pressure, so it must be flexible, durable, and have low permeability at both high and low temperature ranges. This layer is critical for the inflatable links. More bladder layers can be employed to provide redundancy. The bladder layer is not subjected to load and therefore does not need high tensile strength. The bladder is oversized with respect to the restraint layer and it is indexed to prevent it from displacing and bearing load during the deployment. The bladder is composed of polymeric materials that can be folded, packed and bent without damage. Combitherm, a laminate consisting of multiple polyethylene, nylon, and EVOH (vinyl alcohol) layers was selected for TransHab [36].

The restraint layer, or structural layer, is the main structural component that supports the loads resulting from the inflation. Since it carries the hoop and axial loads, it must have high tensile strength capabilities. The restraint layer must be foldable, deployable and inflatable on orbit and preserve its structural integrity. The restraint layer, as the load bearing element of the shell, has to comply with the NASA structural design standard NASA-STD-5001 specifications, designing it with a Factor of Safety of 4.0. In [36] several materials were considered, however the most promising resulted Kevlar™ and Vectran™. For TransHab, Kevlar™ was chosen over Vectran™ because of its significant flight history, thoroughly well known properties, availability, and low cost. Nevertheless, Vectran™ fabric was selected by Sierra Space for LIFE [37] and Therefore, for the inflatable robot, Kevlar™ and Vectran™ are considered as materials for the restraint layer. In general they have similar properties. They have high tensile modulus: as an example, Vectran™ UM has $E = 103$ GPa [60], and Kevlar™ 49 has $E = 112$ GPa [61]. They both have density of 1.4 $\mathrm{g/cm^3}$. As a comparison, aluminum has $E = 70$ GPa and density of 2.8 $\mathrm{g/cm^3}$. Moreover, Kevlar™ shows great radiation shielding performances [62]. Other interesting properties are: near–zero coefficients of thermal expansion (CTE), resistance to high and low temperature ranges, abrasion, creep resistance. They offer vibration damping characteristics, particularly suitable for the inflatable link of the robot. Finally, they have high impact strength, a feature used in space application to offer debris shielding. Kevlar™ fibers are an emerging bumper shield material for space structures, tested against medium size debris [63]. Kevlar aramid fibre was initially used in addition to aluminium and ceramic materials, for the debris

shielding systems of the European permanently manned laboratory Columbus [64]. A 7 mm thick Vectran™ shield stopped a polycarbonate projectile with 14 mm in diameter and 1 g in mass at 6.45 km/s [65].

The MMOD layer is sized for the mission and has the main role is to shield the restraint and bladder layers from hypervelocity impact damage caused by MMOD. In general this layer is made of multi-material layup made of ceramic fabric bumper layers, separated by low-density foam, and a high strength fabric rear wall, e.g., Kevlar™ for TransHub. The total density and number of layers depends on the mission. For the inflatable robot, the MMOD is not a crucial layer, since debris protection can be provided by the restraint layer. The inflatable robot should be exposed for short periods of time to the space due to its ability to be deployed and retracted, reducing the debris collision probability.

The thermal protection system (TPS) is the outer layer of the shell and its function is to passively regulate the inner temperature. It employs multi-layer insulation (MLI), analogous to that of an extra-vehicular activity (EVA) space suit. This insulation consists of thin sheets of Nylon reinforced, double aluminized Mylar that are enclosed by an inner and outer layer of double aluminized polymide (Kapton) film [58]. The total number of layers is dependent on the mission: for the inflatable robot, the application of TPS should be assessed.

In [66] the material layers for an expandable lunar habitat are presented providing a similar analysis as previously reported.

In conclusion the critical layers for the construction of the inflatable links are the bladder and restraint layer, providing gas insulation and load bearing. As further explained in Section 2.3, the mechanical behavior of an inflated beam depends on the material used for the restraint layer. An effective technique to construct the restraint layer is braiding, that is a textile production process that is suitable for creating tubular structures. It allows fibers to be aligned along the axis of the beam, maximizing the flexural performances [67].

2.3 Inflatable Beam and Collapse Moment

This section presents the theoretical framework for the modeling and design of inflatable beams, which are used as the robot links in this study. The main parameters that govern the structural behavior of inflatable beams are the collapse moment and the wrinkling moment, which indicate the onset of instability and loss of stiffness under bending loads. These parameters are essential for the design of the inflatable robot, as they determine the optimal trade-off between payload, internal pressure and geometrical properties. Throughout this dissertation, the symbols M_c and M_w will denote the collapse moment and the wrinkling moment, respectively.

This section also reviews the Euler-Bernoulli and Timoshenko beam theories, which can be used to describe the load-deflection relations of inflatable beams, taking into account the effects of internal pressure. Finally, different models for simulating inflatable beams are introduced, with the aim of developing a comprehensive model for the whole robotic system.

2.3.1 Wrinkling and collapse moment

Consider a cantilevered cylindrical beam that is inflated and subjected to a load F at the tip, following the sign convention in Fig. 2.5.

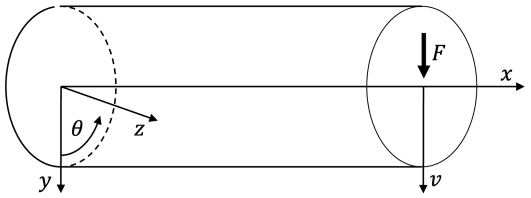

Fig. 2.5 Cylindrical beam sign convention: xyz reference frame, hoop coordinate θ, external tip load F and vertical displacement v.

The material is assumed to be a true membrane, i.e., having no out-of-plane bending stiffness. Assume that the cross-section of the beam remains constant during the deformation. Applying the Euler-Bernoulli beam theory and the force equilibrium condition, the expressions for the axial and hoop stresses are derived,

assuming that no wrinkling occurs in the wall of the beam:

$$\sigma_x = \frac{pr}{2t} - \frac{F(L-x)}{\pi r^2 t}\cos\theta, \tag{2.1}$$

$$\sigma_\theta = \frac{pr}{t}, \tag{2.2}$$

where p is the internal pressure, F is the external load applied at the tip, r, t, and L are the radius, thickness and length of the beam, σ_x and σ_θ are the axial and hoop stresses, respectively.

As the external load increases, for the membrane case wrinkles can be assumed to initiate when the lowest in-plane principal stress becomes zero, that is $\sigma_{x,min}$ at the fixed end of the beam, as shown in Fig. 2.6. Hence, the following expression can be obtained for the wrinkle moment of the inflated beam:

$$\sigma_{x,min} = \frac{pr}{2t} - \frac{FL}{\pi r^2 t} = 0 \quad \rightarrow \quad M_w = FL = \frac{\pi p r^3}{2}, \tag{2.3}$$

where M_w is the wrinkling moment based on the beam theory and stress-based wrinkle criterion.

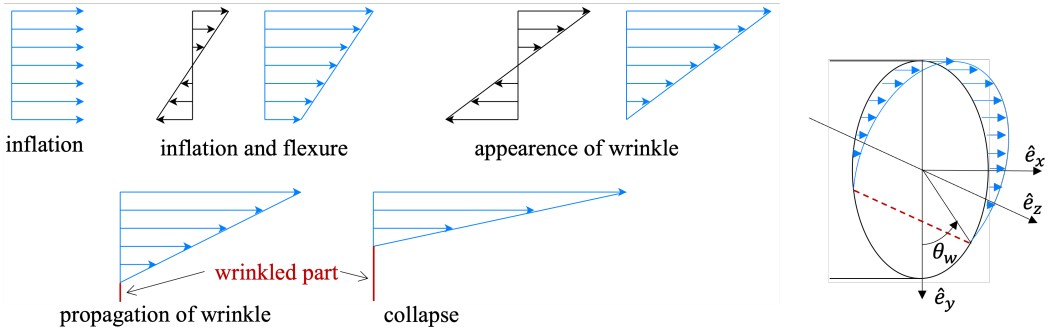

Fig. 2.6 Cases of stress σ_x distribution and wrinkle opening angle θ_w.

The wrinkling moment M_w is defined as the moment for which the first wrinkle occurs. The collapse moment M_c, at which collapse takes places, is regarded as the moment at which an increase in deflection does not result in an increase in moment. In general if the bending load in under the wrinkling moment $M \leq M_w$ the inflatable beam shows a linear behavior. In Fig. 2.7 a qualitative load-deflection diagram is shown.

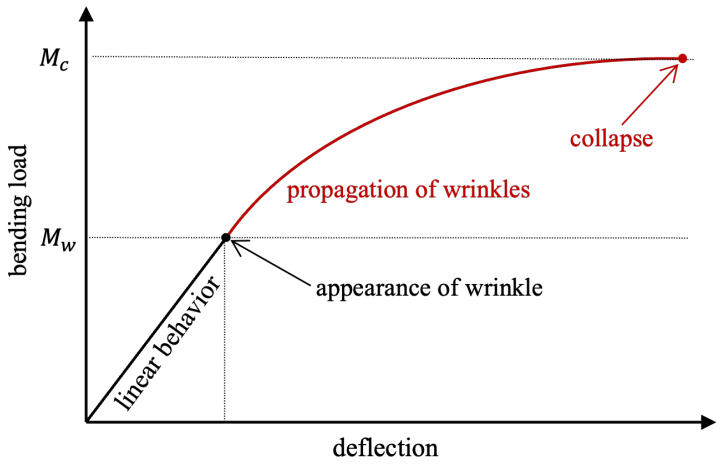

Fig. 2.7 Typical behavior of an inflatable beam with wrinkling moment M_w and collapse moment M_c.

Different formulations for the collapse moment exist in the literature, depending on whether the material is treated as a shell or a membrane, and whether it is isotropic or anisotropic. The subsequent formulations are classified according to the modeling methods employed:

- membrane: Stein (1961) [68], Wielgosz (2002) [69];
- thin shell: Brazier (1927) [70], Zender (1962) [71], NASA (1968) [72], Veldman (2005) [73, 67].

Stein et.al. (1961) [68] derived the collapse moment for a true membrane cylinder subjected to bending and internal pressure:

$$M_{c,Stein} = \pi p r^3, \tag{2.4}$$

that is twice the theoretical wrinkling moment. In literature, it is common to consider $M_c = 2M_w$ independently from the approach used for estimating the collapse moment [73]. The theoretical collapse moment cannot be reached unless large undesirable deformations occur [72], therefore semi-empirical approaches are often used. Wielsgosz et al. (2002) [69], proposed to reduced the value of the collapse moment to:

$$M_{c,Wielsgosz} = \frac{\pi}{4}\pi p r^3, \tag{2.5}$$

where $\pi/4 = 0.785$ is a design factor which is similar to the factor of 0.8 suggested by the NASA SP 8007 [72] explained below.

When the material is modeled as a shell instead of a membrane, a beam may have bending stiffness even when the pressure is zero.

Brazier (1927) [70] proposed a method to derive the collapse (or critical) bending moment for a shell by minimizing the strain energy per unit length, which is a function of the axial curvature. He applied this method to the case of infinitely long cylinders. For an unpressurized isotropic shell, he obtained the collapse moment as:

$$M_{c,Brazier} = \frac{2\sqrt{2}}{9} \frac{E\pi rt^2}{\sqrt{1-\nu^2}}, \tag{2.6}$$

where E and and ν are the Young's modulus and the Poisson's ratio of the material, respectively. Wood (1958) [74] extended the expression for the case of internal pressure:

$$M_{c,Wood} = \frac{2\sqrt{2}}{9} E\pi rt^2 \sqrt{\frac{1}{1-\nu^2} + 4 \cdot \frac{p}{E} \left(\frac{r}{t}\right)^3}. \tag{2.7}$$

Baruch et al. [75] modified the Brazier's expression for orthotropic materials:

$$M_{c,Baruch} = \frac{2\sqrt{2}}{9} \pi rt^2 \sqrt{\frac{E_x E_\theta}{1-\nu_{x\theta}\nu_{\theta x}}}, \tag{2.8}$$

The two expressions can be combined, obtaining:

$$M_{c,Wood\&Baruch} = \frac{2\sqrt{2}}{9} E_x \pi rt^2 \sqrt{\frac{E_\theta}{E_x}} \sqrt{\frac{1}{1-\nu_{x\theta}\nu_{\theta x}} + 4\frac{p}{E_\theta} \left(\frac{r}{t}\right)^2}. \tag{2.9}$$

Zender (1962) [71] derived a semi-empirical expression for the collapse moment of a pressurised cylindrical shell based on a membrane approach:

$$M_{c,Zender} = \pi pr^3 + \frac{\pi E rt^2}{2\sqrt{3(1-\nu^2)}}. \tag{2.10}$$

In NASA SP 8007 (1968) [72] the collapse moment is calculated following the approache used by Zender, by adding three components: the moment-carrying capability of a pressurized membrane cylinder (which is 80% of the theoretical value for design purposes), the collapse moment for the unpressurized cylinder, and an

increase in the critical moment due to pressurization.

$$M_{c,NASA} = 0.8\pi pr^3 + \pi rEt^2 \left(\frac{\gamma}{\sqrt{3(1-\nu^2)}} + \Delta\gamma \right), \tag{2.11}$$

where

$$\begin{cases} \gamma = 1 - 0.731(1 - e^{-\phi}), \\ \phi = \frac{1}{16}\sqrt{\frac{r}{t}} \quad \text{for} \quad \frac{r}{t} < 1500, \\ \Delta\gamma = f\left(\frac{p}{E}\left(\frac{r}{t}\right)^2\right). \end{cases} \tag{2.12}$$

where $\Delta\gamma$ is a function of the pressure parameter obtained by the Fig. 2.8.

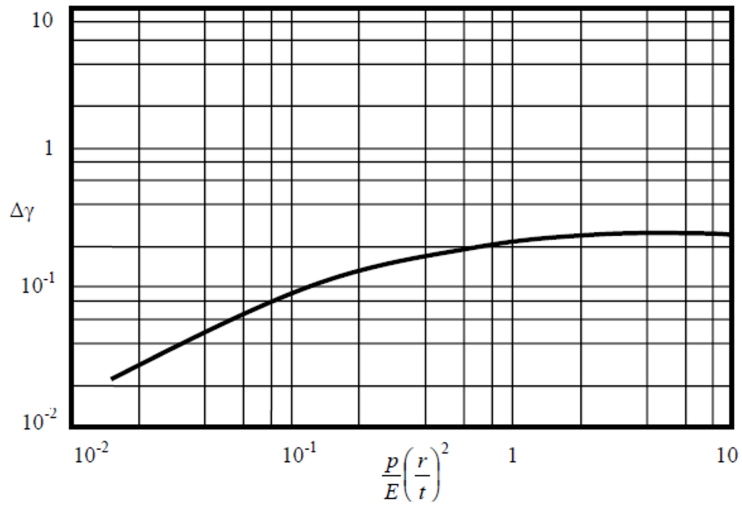

Fig. 2.8 Increase in axial-compressive buckling-stress coefficient of cylinders due to internal pressure.

The relation for orthotropic materials is:

$$M_{c,NASA} = 0.8\pi pr^3 + \pi rE_x t^2 \left(\frac{1 - 0.731(1 - e^{-\phi})}{\sqrt{3(1 - \nu_{x\theta}\nu_{\theta x})}} + \Delta\gamma \right), \tag{2.13}$$

Veldman (2005) [73, 67], using the approach of NASA, combined the formulation by Wielsgosz, Wood and Baruch, obtaining for pressurized orthotropic materials:

$$M_{c,Veldman} = \frac{\pi}{4}\pi pr^3 + \frac{2\sqrt{2}}{9}E_x\pi rt^2\sqrt{\frac{E_\theta}{E_x}}\sqrt{\frac{1}{1-\nu_{x\theta}\nu_{\theta x}} + 4\frac{p}{E_\theta}\left(\frac{r}{t}\right)^2}. \tag{2.14}$$

The parameter r/t is to the power 2 instead of 3. This expression is only valid for moderately long cylinders ($L/r > 20$).

Fig. 2.9 compares the collapse moment formulations by Stein in Eq. (2.4), Wielsgosz in Eq. (2.5) and Veldman in Eq. (2.14) for different pressure values.

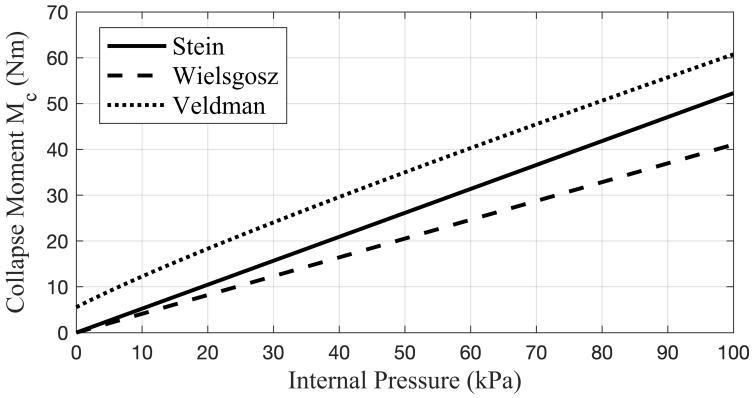

Fig. 2.9 Comparison of collapse moment formulations by Stein, Wielsgosz and Veldman depending on the pressure p. Assumed parameters: $r = 55$ mm, $t = 0.5$ mm, $E_x = E_\theta = 400$ MPa, $\nu = 0.2$.

In [76], Veldman proposed wrinkling prediction of cylindrical and conical inflated cantilever beams under torsion and bending, extending the presented formulation. However, in this dissertation only the wrinkling and collapse moment due to bending load are considered in order to design and sizing the robotic system.

2.3.2 Bending Load Model

The problem of an inflatable beam that is deformed by internal pressure and external loading is considered. The beam is made of a cylindrical membrane that undergoes two stages of loading: inflation to a given internal pressure p and application of a transverse force $F\widehat{\boldsymbol{y}}$ at end $x = L$. In the initial stress-free state, or natural configuration, the beam occupies the region $\Omega_\varnothing$. The inflation induces a pre-stressed state, or reference configuration, in which the beam occupies the region Ω_0. The indexes $\varnothing$ and 0 are used to indicate the quantities in the stress-free state and in the pre-stressed state, respectively. The actual, pressurized and bent configuration, don't make use of any index. The configurations are shown in Fig. 2.10.

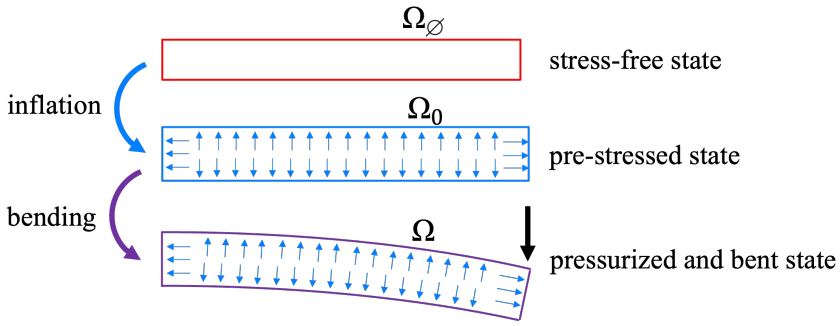

Fig. 2.10 Configurations of inflatable beam.

The beam is built-in at end $x = 0$ and lies in the xy-plane, as shown in Fig. 2.5. The linearized problem of an inflated cantilever beam under bending is performed in [77] with respect to a pre-stressed reference configuration. The deflection v and rotation δ are calculated as:

$$v(x) = \frac{F}{(E + P/S_0)I_0}\left(\frac{L_0 x^2}{2} - \frac{x^3}{6}\right) + \frac{Fx}{P + jGS_0}, \tag{2.15}$$

$$\delta(x) = \frac{F}{(E + P/S_0)I_0}\left(L_0 x - \frac{x^2}{2}\right), \tag{2.16}$$

where F is the external force, E the Young's modulus and G the shear modulus of the material, $P = pA_0 = p\pi r_0^2$ is the axial force produced by the internal pressure on the base of the cylinder, S_0 is the cross-section area, L_0 is the length and I_0 is the second moment of area of the beam. j is the correction shear coefficient, determined from the shape of the cross-section. The value usually found in the literature, e.g., in [78], for circular thin tubes is $j = 0.5$.

The solution is linear with respect to the external load F, but non-linear with respect to the pressure p. Moreover, the pressure affects the reference dimensions L_0, S_0 and I_0 although this effect may be negligible for most applications. When the internal pressure is zero, the Timoshenko's beam model gives the same results as these relations. However, unlike a classical beam, an inflatable beam is made of a membrane that requires some pressure to prevent it from collapsing, as explained in the previous section. More precisely, the solution is valid if $M = FL_0 \leq M_w$ that, using Eq. (2.3), leads to:

$$p \geq \frac{2FL_0}{\pi r_0^3}. \tag{2.17}$$

The inflation amounts to strengthen the Young's modulus and the shear modulus. In particular, when p tends to infinity, so do the equivalent material properties and the deflection and the rotation are identically zero. Equivalent Young's modulus E_p and shear modulus G_p can be defined as:

$$E_p(p) = E + p\frac{A_0}{S_0}, \tag{2.18}$$

$$G_p(p) = jG + p\frac{A_0}{S_0}, \tag{2.19}$$

that depend on the pressure p. These definitions allow to obtain the classical equations of Timoshenko's beam model:

$$v(x) = \frac{F}{E_p I_0}\left(\frac{L_0 x^2}{2} - \frac{x^3}{6}\right) + \frac{Fx}{G_p S_0}, \tag{2.20}$$

$$\delta(x) = \frac{F}{E_p I_0}\left(L_0 x - \frac{x^2}{2}\right). \tag{2.21}$$

In particular, at the tip of cantilever beam, that is for $x = L_0$:

$$v(L_0) = \frac{FL_0^3}{3E_p I_0} + \frac{FL_0}{G_p S_0} \tag{2.22}$$

$$\delta(L_0) = -\frac{FL_0^2}{2E_p I_0} \tag{2.23}$$

Timoshenko beam theory takes into account shear deformation and rotational inertia effects, whereas Euler-Bernoulli assumes that the beam cross-sections remain plane and normal to the deformed beam axis. However in many applications Euler-Bernoulli beam theory produces very similar result if the beam is slender enough and the structural wavelegth is much larger than the cross-section area. In this case, the shear deformation and rotational inertia effects are negligible and the Timoshenko beam theory converges to the Euler-Bernoulli beam theory [79].

The rotation expressed in Eq.(2.23) is the same using the Euler-Bernoulli beam theory. The equivalent stiffness is:

$$k = \frac{M}{\delta(L_0)} = \frac{FL_0}{\delta(L_0)} = \frac{2E_p I_0}{L_0}. \tag{2.24}$$

The deflection can be written isolating the shear effect:

$$v(L_0) = \frac{FL_0^3}{3E_pI_0}\left(1+\frac{3}{L_0^2}\frac{E_pI_0}{G_pS_0}\right) = \frac{FL_0^3}{3E_pI_0}\left(1+\frac{3}{\alpha}\right), \tag{2.25}$$

with

$$\alpha = \frac{G_pS_0L_0^2}{E_pI_0} \tag{2.26}$$

If $3/\alpha \sim 0$ the Euler-Bernoulli theory can be used, leading to:

$$v(L_0) = \frac{FL_0^3}{3E_pI_0}. \tag{2.27}$$

As said, the reference dimensions in pre-stressed configuration, length L_0, radius r_0 and thickness t_0, are computed as functions of the internal pressure by using the well-known elastic small strain analytical solution for thin tubes:

$$L_0 = L_\varnothing\left(1+\frac{1-2\nu}{2}\frac{pr_\varnothing}{Et_\varnothing}\right), \tag{2.28}$$

$$r_0 = r_\varnothing\left(1+\frac{2-\nu}{2}\frac{pr_\varnothing}{Et_\varnothing}\right), \tag{2.29}$$

$$t_0 = t_\varnothing - \frac{3\nu}{E}\frac{pr_\varnothing}{2}. \tag{2.30}$$

2.3.3 Non-linear post-wrinkling model

The proposed linearized model is convenient since it uses classical linear beam theory, such as Timoshenko and Euler-Bernoulli models, with adjustments accounting for the internal pressure. This assumption holds only for wrinkle-free cases, i.e., when Eq. 2.17 is satisfied. However, the post-wrinkling analysis of the deformation problem can provide valuable insights. Veldman proposed an approach to model the post-wrinkling behavior of the beam in [73]. Expressions of equilibrium of forces and moments in the taut region and in the wrinkled region are considered, following the same approach used by Stein [68] with minor modifications, leading to:

$$\frac{M}{pr^3-2tr^2\sigma_s} = \frac{\pi}{2}\frac{\pi-\theta_w+\cos(\theta_w)\sin(\theta_w)}{\sin(\theta_w)+(\pi-\theta_w)\cos(\theta_w)}, \tag{2.31}$$

where θ_w is the wrinkling opening angle, shown in Fig. 2.6, that measures the angular width of the wrinkles that occur in the wrinkled section at the x coordinate, and σ_s the collapse stress for a shell, that depends on the formulation of the moment at which collapse takes place. For a true membrane $\sigma_s = 0$. Veldman's assumption is that the beam collapses when wrinkles cover half of the cross-section: the wrinkling angle is $\theta_w = \pi$ and the right-hand side of equation approaches π; under this condition:

$$M_c = \pi r p^3 - 2\pi t r^2 \sigma_s. \tag{2.32}$$

The first part at the right hand side of the equation is the theoretical collapse load for Stein [68], that in Eq.(2.14) is reduced by the factor $\pi/4$. The second part at the right hand side of the equation is the component relative to the shell material, that correspond to the second part of Eq.(2.14). Therefore σ_s is assumed as:

$$\sigma_s = \frac{\sqrt{2}}{9} E_x \frac{t}{r} \sqrt{\frac{E_\theta}{E_x}} \sqrt{\frac{1}{1-\nu_{x\theta}\nu_{\theta x}} + 4\frac{p}{E_\theta}\left(\frac{r}{t}\right)^2}. \tag{2.33}$$

Finally, the magnitude of the wrinkling angle θ_w for a bending moment M can be obtained numerically from:

$$\begin{aligned} M = {} & \frac{\pi}{2} \frac{\pi - \theta_w + \cos(\theta_w)\sin(\theta_w)}{\sin(\theta_w) + (\pi - \theta_w)\cos(\theta_w)} \\ & \cdot \left(\frac{\pi}{4} p r^3 + \frac{2\sqrt{2}}{9} E_x r t^2 \sqrt{\frac{E_\theta}{E_x}} \sqrt{\frac{1}{1-\nu_{x\theta}\nu_{\theta x}} + 4 \cdot \frac{p}{E_\theta}\left(\frac{r}{t}\right)^2} \right). \end{aligned} \tag{2.34}$$

The wrinkling moment M_w is defined as the maximum bending moment that satisfies $\theta_w = 0$:

$$\begin{aligned} M_w &= \frac{1}{2}\left(\frac{\pi}{2}\right)^2 p r^3 + \frac{1}{2}\frac{2\sqrt{2}}{9} E_x \pi r t^2 \sqrt{\frac{E_\theta}{E_x}} \sqrt{\frac{1}{1-\nu_{x\theta}\nu_{\theta x}} + 4 \cdot \frac{p}{E_\theta}\left(\frac{r}{t}\right)^2} \\ &= \frac{1}{2} M_c, \end{aligned} \tag{2.35}$$

that is half the collapse moment. The following expression for the curvature parameter κ in the wrinkled region can be written:

$$\kappa = \frac{M}{E_x t r^3 \left(\pi - \theta_w + \cos(\theta_w)\sin(\theta_w)\right)} \quad \text{if } M > M_w. \tag{2.36}$$

In the taut region the wrinkling angle $\theta_w = 0$, and the curvature expression becomes:

$$\kappa = \frac{M}{\pi E_x t r^3} \quad \text{if } M \leq M_w. \tag{2.37}$$

The elastic curve can be obtained by integration of the well-know relation:

$$\frac{d^2y}{dx^2} = \frac{1}{\kappa}. \tag{2.38}$$

In Fig. 2.11 an example of elastic curve, bending moment diagram and wrinkling opening angle θ_w in wrinkled and non-wrinkled conditions.

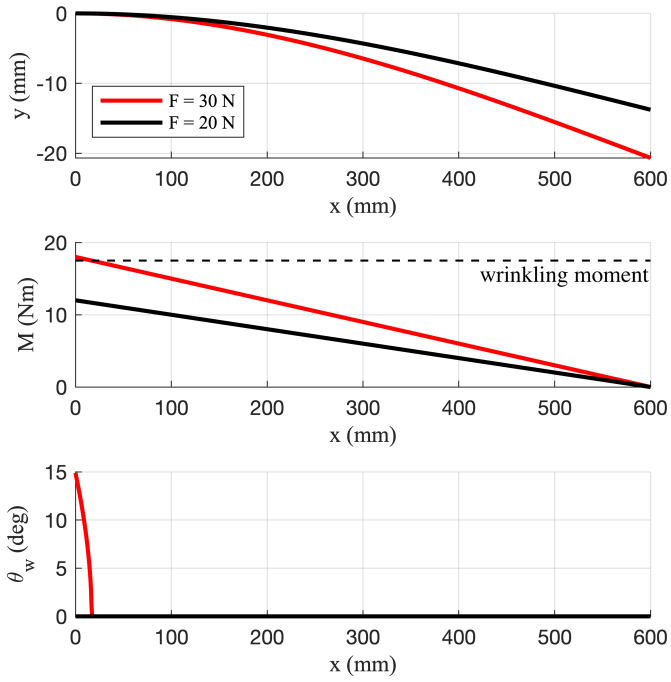

Fig. 2.11 Elastic curve, bending moment diagram and wrinkling opening angle θ_w at two load values, wrinkling moment in dashed line. Assumed parameters: $r = 55$ mm, $L = 600$ mm, $p = 50$ kPa, $t = 0.5$ mm, $E_x = E_\theta = 400$ MPa, $\nu = 0.2$.

Finally, an example of load-deflection curve, underlining the dependence on the internal pressure, considering the post-wrinkling behavior, is shown in Fig. 2.12.

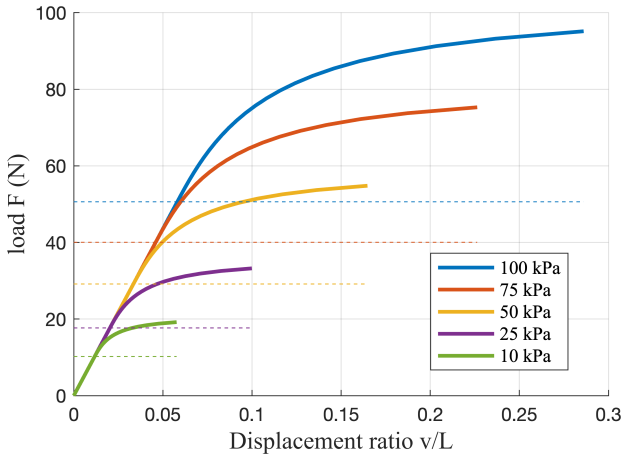

Fig. 2.12 Veldman load-deflection curve: displacement ratio v/L versus applied force F. Theoretical wrinkling moment in dashed line. Assumed parameters: $r = 55$ mm, $L = 600$ mm, $t = 0.5$ mm, $E_x = E_\theta = 400$ MPa, $\nu = 0.2$.

2.4 Link Modeling

Inflatable structures experience two stages of loading: inflation to pressure p that results in the pre-stressed configuration and application of external forces. The robot inflatable links can be considered as flexible cylindrical beams, with adjustments that account for pressure. To analyze their dynamic behavior, different methods can be employed [80], such as:

- Lumped-Parameters Method (LPM),
- Finite Element Method (FEM).

These methods differ in the way they discretize the beam and represent its kinematics.

The objective of this section is to introduce some aspects of modeling and adapting general flexible beam models to the case of inflatable beam, without going into the details of these well-known methods. Specifically, lumped-parameter methods, used especially in multibody models, and finite element methods will be examined with the goal of modeling the whole robotic structure. The methods are discussed considering the xy-plane, focusing on the flexural behaviour. The formulation can be easily extended to axial and torsional behaviour and in the xz-plane.

2.4.1 Lumped-Parameter Method

The dynamics of a flexible beam are governed by partial differential equations that pose computational challenges. Lumped parameter models reduce the complexity approximating the flexible beam with a finite number of degrees of freedom (DOFs) and parameters. These models discretize the beam into segments and assign joints to the middle points of each segment along the neutral axis, as shown in Fig. 2.13 [81].

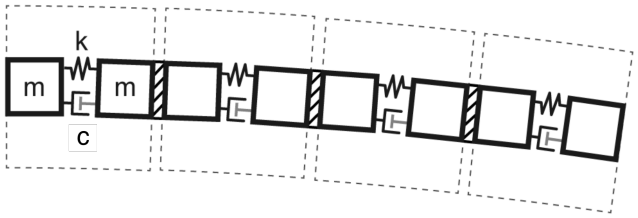

Fig. 2.13 A flexible body according to the lumped-parameter method.

The joints have rotational DOFs and are connected by springs and dampers that account for the stiffness and damping characteristics of the beam, such as material proprieties and geometry.

The lumped parameters, such as spring stiffness and damping coefficient, can be obtained from experimental data or analytical solutions [82]. Lumped parameter models enable the computation of static deflection, natural frequencies, mode shapes, and state-space representation of the beam dynamics. Moreover, they can be implemented in software tools such as Simscape Multibody and Simulink for simulation and analysis.

The equivalent stiffness of the beam, see Eq.(2.24), is used in the lumped parameter model. If just a element is considered, the spring is collocated at $x = L_0/2$ and the stiffness is:

$$k_{LPM} = \frac{FL_0/2}{\delta(L_0)} = \frac{E_p I_0}{L_0}, \tag{2.39}$$

This choice provides same angular deflection obtained analytically in Eq.(2.23), but not equal vertical deflection:

$$\delta_{LPM} = \frac{FL_0^2}{2E_p I_0}, \tag{2.40}$$

$$v_{LPM} = \frac{FL_0^3}{2E_p I_0}. \tag{2.41}$$

To enhance the accuracy of the lumped parameter model, the beam is discretized into n smaller elements, each with a length $\ell_0 = L_0/n$, and the lumped elements are interconnected to form the model of the beam, as in Fig. 2.13. The stiffness of a single beam segment is given by:

$$k_n = \frac{E_p I_0}{\ell_0}, \tag{2.42}$$

In general $k_n = k_n(p)$ depends on internal pressure of the beam since all the quantities E_p, I_0, ℓ_0 depend on pressure. However, this dependence can be slight and negligible in some applications.

Material damping is a complex phenomenon and difficult to measure precisely. A simple approximation is to assume a linear relationship between the damping coefficient and the spring coefficient $c_n = \beta k_n$, where β is an empirical damping factor. The damping coefficient then varies with the discretization level of the beam: a finer discretization leads to a higher damping coefficient. [81].

Pseudo-Rigid Body Model

The Pseudo-Rigid Body Model (PRBM) [83–85] follows the approach of Lumped-Parameter Models. The cylindrical beam, with length L, is represented as two rigid bodies, having same radius r and length l_1 and l_2, such as $L = l_1 + l_2$, as shown in Fig. 2.14. Notice that $L = L_0$ and $r = r_0$ are considered. The two rigid bodies are connected by a joint with a spring and damper. In general, the joint is positioned in an arbitrary position along the neutral axis of the beam.

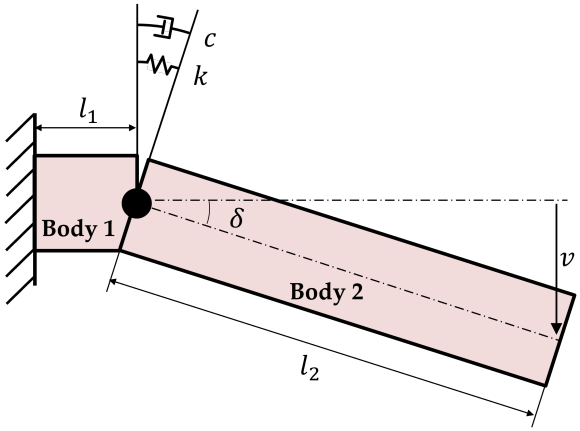

Fig. 2.14 Pseudo-Rigid Body Model

The beam dynamics can be described by the following ordinary differential equation:

$$I_{M,0}\ddot{\delta} + c(p)\dot{\delta} + k(p)\delta = \tau, \tag{2.43}$$

where $I_{M,0}$ is the moment of inertia, p the internal relative pressure and τ the external torque. Stiffness and damping coefficients are considered as depending on the internal pressure. In general $I_{M,0}$ depends on pressure, however if the length $L_0 \sim L_\varnothing$ and the radius $r_0 \sim r_\varnothing$, the moment of inertia can be assumed approximately equal to the nominal value $I_{M,0} \sim I_{M,\varnothing}$.

For inflatable beam the joint can be positioned close to the clamped face, where stress is higher. This choice is particularly suitable when post-wrinkling behavior is considered, and an experimental characterization for the estimation of stiffness and damping coefficients is performed.

The stiffness expression can account for non-linearities [41]. In the specific case, for inflatable beams, the stiffness can consider non-linear behavior after wrinkling moment resulting $k = k(p, \delta)$ dependent on both pressure and deflection δ. Let us introduce δ_w as the angular deflection of the beam under a load corresponding to wrinkling moment, that is $M = M_w$. If $\delta \leq \delta_w$ the beam expresses a linear behavior, while for $\delta > \delta_w$ post-wrinkling non linearities appear, as shown in Fig. 2.12.

An alternative choice, for $\delta \leq \delta_w$, consists in positioning the joint at $x = L/3$, so that $l_1 = L/3$. Assuming the equivalent stiffness $k = \frac{4EI}{3L}$, the angular deflection is $\delta = \frac{FL^2}{2EI}$. Considering Euler-Bernoulli beam theory, this choice allows to obtain consistent vertical deflection, since $v = \frac{2}{3}L\sin(\delta) \sim \frac{2}{3}L\delta = \frac{FL^3}{3EI}$.

2.4.2 Finite Element Methods

The finite element method (FEM) is a general numerical technique for approximating the solution of partial differential equations by discretizing the domain into finite elements. FEM is based on the subdivision of the structure into finite elements. Many formulations have been developed depending on their shape and characteristics [80], e.g., beam elements, plate elements, membrane elements, shell elements and many others.

Inflatable structures can be computed with 3D thin shell or membrane finite elements. However, a lot of structures, as the inflatable link of the robot, can be

analyzed with beam finite elements so as to significantly reduce the computing time. This section will not present a comprehensive overview of FEM, but only the practices and hypotheses that are necessary for accurately modeling inflatable beams.

1D Beam Element

The most common formulation for the beam elements are Euler-Bernoulli beam element, i.e., does not take into account shear deformation, and Timoshenko beam elements. These elements are classified as 1D elements, and their discretization is illustrated in Fig. 2.15. Each node of the beam has 6 DOFs: 3 displacements and 3 rotations. Hence, an element has 12 DOFs. The beam has the properties required to achieve a complete decoupling between axial, torsional and flexural behavior in each coordinate plane.

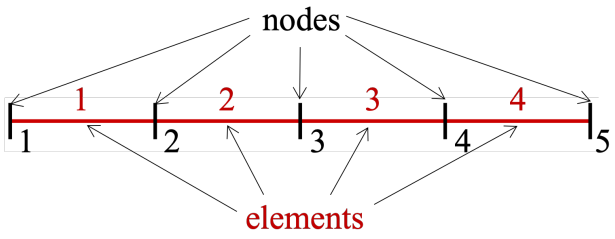

Fig. 2.15 FEM discretization using beam elements

This paragraph briefly describes the linearized problem for the flexural behavior of an element in the *xy*-plane, which can be generalized to characterize the overall behavior of the inflatable beam. In this case each element has 4 DOFs: displacements in the *y*-direction and the rotation about the *z*-axis of the two nodes. In this case, the vector of nodal displacements is:

$$\boldsymbol{q} = [v_{y1}, \delta_{z1}, v_{y2}, \delta_{z2}]^T. \tag{2.44}$$

The bending stiffness matrix is written according the classical Timoshenko beam theory as:

$$\boldsymbol{K}(p) = \frac{E_p I_0}{L_0^3(1+\Phi_p)} \begin{bmatrix} 12 & 6L_0 & -12 & 6L_0 \\ 6L_0 & L_0^2(4+\Phi_p) & -6L_0 & L_0^2(2-\Phi_p) \\ -12 & -6L_0 & 12 & -6L_0 \\ 6L_0 & L_0^2(2-\Phi_p) & -6L_0 & L_0^2(4+\Phi_p) \end{bmatrix}, \tag{2.45}$$

with

$$\Phi_p = \frac{12E_p I_0}{L_0^2 G_p S_0}. \tag{2.46}$$

The matrix for inflatable beam depends on the pressure p. Basically, it corresponds to the classical formulation [80] in which the equivalent Young's modulus E_p and shear modulus G_p are used. Moreover, the quantities with subscript 0 refers to the reference configuration that depends on pressure p. The mass matrix $\boldsymbol{M}$ can be derived from the classical formulation, using the same procedure. Then, the damping matrix can be expressed as linear combination of the mass and stiffness matrices:

$$\boldsymbol{D} = \alpha\boldsymbol{M} + \beta\boldsymbol{K}. \tag{2.47}$$

If the beam is slender the Euler-Bernoulli approach can be used setting $\Phi_p = 0$.

3D Membrane and Shell Element

The material layer of the beam can be discretized using finite element methods with different element shapes and formulations. In [86], the nonlinear responses of inflatable pillows are modeled using thin sheet elements based on the Kirchhoff-Love theory. In [87], the inflatable beam is modeled as a 3D membrane structure, as shown in Fig. 2.16. The membrane elements have no bending stiffness and satisfy the plane stress condition. The 3D constitutive law is the Saint-Venant Kirchhoff one, characterized by the Young's modulus E and Poisson ratio ν. The results show that the inflatable beam model and the 3D membrane finite element solution are coherent.

The membrane finite element solution starts from the natural configuration, where the internal pressure is zero. Then, the pressure p is applied to reach the pre-stressed

configuration. Finally, the external load F is applied. This procedure enables the incorporation of the internal pressure effect.

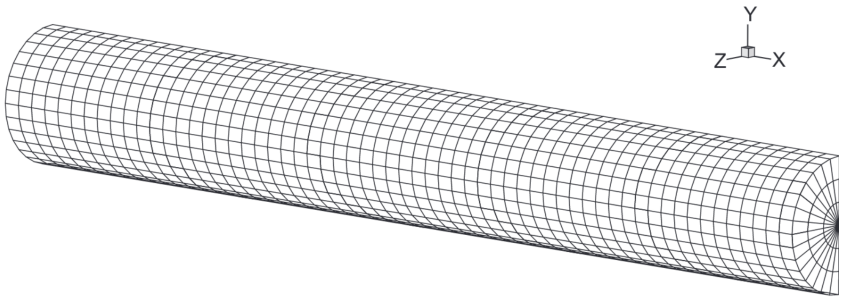

Fig. 2.16 Typical mesh used in 3D membrane finite element models.

3D Membrane and Shell Element models are computationally demanding and slow down the simulation process. A reduced order model can achieve lower computational complexity and faster simulation speed by eliminating the high-frequency, low-amplitude vibration modes that have negligible impact on the accuracy. A common model reduction technique for multibody problems is the Craig-Bampton method, introduced by R. Craig and M. Bampton in 1968 [88]. This method maps the boundary nodes to interface frames, which enables the finite-element import method, used in software such as Matlab/Simulink [81], see Fig 2.17. The Craig-Bampton method simplifies the model by discarding all fixed-boundary vibration modes above a certain frequency threshold. The resulting model has fewer variables and smaller mass and stiffness matrices.

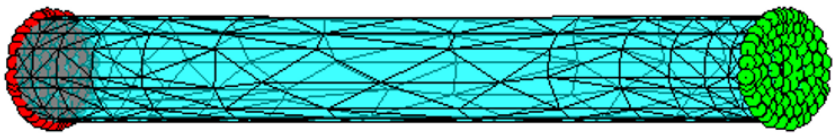

Fig. 2.17 Typical mesh used in a reduced order model in Matlab/Simulink.

2.5 Robot Modeling

The dynamic model of a robot with flexible links involves accounting for both the rigid body dynamics of the robot and the flexible dynamics of the links. Hence, the models for inflatable links, introduced in the previous section, are employed to develop correspondent models for the inflatable robot.

These models can share the same nomenclature and dynamic formulation. The vector $\boldsymbol{q}$ is defined as:

$$\boldsymbol{q} := [\boldsymbol{\theta}^T, \boldsymbol{\delta}^T]^T \in \mathbb{R}^{N+M} \tag{2.48}$$

where $\boldsymbol{\theta}$ is a vector of the N joint variables (or rigid coordinates), $\boldsymbol{\delta}$ is the vector of the M flexible coordinates.

The general dynamic model of robots with flexible link is [89]:

$$\begin{bmatrix} \boldsymbol{M}_{\theta\theta}(\boldsymbol{q}) & \boldsymbol{M}_{\theta\delta}(\boldsymbol{q}) \\ \boldsymbol{M}_{\theta\delta}^T(\boldsymbol{q}) & \boldsymbol{M}_{\delta\delta}(\boldsymbol{q}) \end{bmatrix} \begin{bmatrix} \ddot{\boldsymbol{\theta}} \\ \ddot{\boldsymbol{\delta}} \end{bmatrix} + \begin{bmatrix} \boldsymbol{c}_\theta(\boldsymbol{q}, \dot{\boldsymbol{q}}) \\ \boldsymbol{c}_\delta(\boldsymbol{q}, \dot{\boldsymbol{q}}) \end{bmatrix} + \begin{bmatrix} \boldsymbol{g}_\theta(\boldsymbol{q}) \\ \boldsymbol{g}_\delta(\boldsymbol{q}) \end{bmatrix} + \begin{bmatrix} \boldsymbol{0} \\ \boldsymbol{D}\dot{\boldsymbol{\delta}} + \boldsymbol{K}\boldsymbol{\delta} \end{bmatrix} = \begin{bmatrix} \boldsymbol{\tau} \\ \boldsymbol{0} \end{bmatrix}, \tag{2.49}$$

where $\boldsymbol{M}_{ij}$ is the mass matrix for rigid and flexible coordinates corresponding to the rigid $(i, j = \theta)$ or flexible $(i, j = \delta)$ coordinates and equations, $\boldsymbol{c}(\boldsymbol{q}, \dot{\boldsymbol{q}})$ contains the nonlinear Coriolis and centrifugal terms, $\boldsymbol{g}(\boldsymbol{q})$ is the gravity vector, which accounts for the gravitational forces acting on the robot and $\boldsymbol{\tau}$ is the vector of actuator torques at the joints. $\boldsymbol{K}$ and $\boldsymbol{D}$ are the stiffness and damping matrices, respectively, related to the behavior of the flexible links. Blocks have suitable dimensions, e.g., $\boldsymbol{M}_{\theta\delta}$ in the inertia matrix is $(N \times M)$.

The internal pressure p can be incorporated into the formulation by using methods discussed for the inflatable link modeling, subject to the approximations and validity region of each method. In general, the geometry of the robot is a function the internal pressure p, considering the pre-stressed configuration. Furthermore, the pressure affects the stiffness matrix $\boldsymbol{K}$ and consequently the damping matrix $\boldsymbol{D}$. The stiffness matrix can capture the non-linear behavior of the elastic properties of the link if it accounts for the post-wrinkling phenomenon. For OOS applications, the term $\boldsymbol{g}(\boldsymbol{q}) \simeq \boldsymbol{0}$, and can be simplified.

In compact form, the general model for a robot with inflatable links is:

$$\boldsymbol{M}(\boldsymbol{q},p)\ddot{\boldsymbol{q}}+\boldsymbol{c}(\boldsymbol{q},\dot{\boldsymbol{q}},p)+\boldsymbol{g}(\boldsymbol{q},p)+\begin{bmatrix}\mathbf{0}\\ \boldsymbol{D}(p)\dot{\boldsymbol{\delta}}+\boldsymbol{K}(p,\boldsymbol{\delta})\boldsymbol{\delta}\end{bmatrix}=\begin{bmatrix}\boldsymbol{\tau}\\ \mathbf{0}\end{bmatrix}. \tag{2.50}$$

This model is easily adaptable to different methodologies. For example, it can reduce to a conventional manipulator model with rigid links if $M = 0$ is set and pressure not considered.

The following models are discussed and utilized during the dissertation:

- Rigid Body Model (RBM), assuming traditional rigid links,
- Pseudo-Rigid Body Model (PRBM), introducing virtual joints,
- Flexible Beam Model (FBM), using Finite Element Method (FEM).

Each model has its own advantages and disadvantages in terms of computational efficiency, accuracy, and applicability. In order to provide a thorough explanation of these models, a robot with two inflatable links, with length L_1 and L_2, and three motors ($N = 3$) is considered in the following subsections. In particular, two axes for the shoulder and one axis for the elbow are considered. The wrist is omitted for simplicity, since it consists of rigid joints only.

2.5.1 Virtual Joints

The method of virtual joints adds M additional joints to the kinematic chain in order to consider link deflections. The PRBM of the link is used to evaluate the deflections along two orthogonal axes (xy and xz planes of links), considering same l_1, see Fig. 2.14. Torsional deformations are neglected. The robot kinematic chain reaches 7 DOFs, since $M = 4$. This description adds virtual uncontrolled joint variables, indicated as δ_i. In Fig. 2.18, the schemes of pseudo-rigid body model (PRBM) with virtual joints and 7 DOFs and the rigid body model (RBM) with 3 DOFs are illustrated. Base frame, EE frame given the RBM and EE frame given the PRBM are represented.

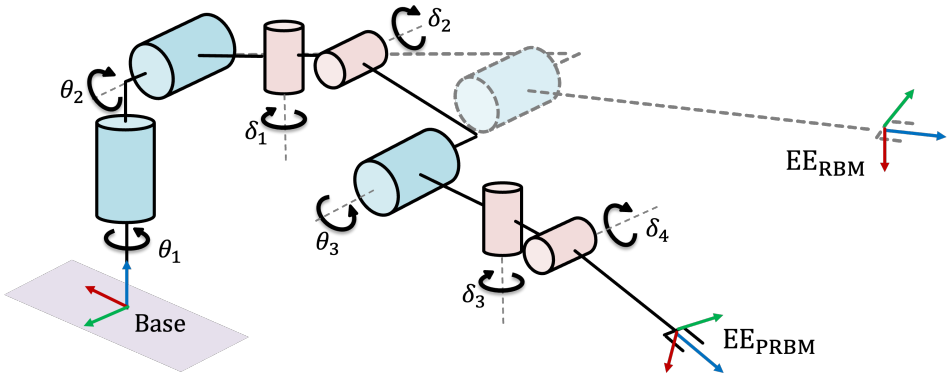

Fig. 2.18 Robot kinematic scheme considering pseudo-rigid body model with virtual joints (PRBM, solid line) and rigid body model (RBM, dashed line).

This model has a low computational cost and is suitable for real-time control of the robot. The flexural state of the link can be measured with sensors and used to update the model continuously. Furthermore, the stiffness of the link can be estimated with experimental tests, as a function of the pressure, taking into account the non-linear behavior of the inflatable link, so that

$$k_i = k_i(p, \delta_i). \tag{2.51}$$

However, this model may introduce errors due to its simplicity and the arbitrary positioning of the virtual joints.

2.5.2 FEM Links

Both lumped-parameter and finite element methods can be used to develop a flexible body model (FBM), that is characterized by a higher number M of flexible coordinates. Fig. 2.19 shows the scheme of RBM and FBM for the inflatable robot. Frames relative to the EE and the base are also reported.

This model has higher computational cost, mainly suitable for off-line analysis, with the aim of developing a digital twin of the robot.

In this dissertation the Euler-Bernoulli beam finite element model is adopted, referring to it as FBM. The model remains valid as long as the robot operates in the linear region of the links, away from the wrinkling condition, and exhibits small link

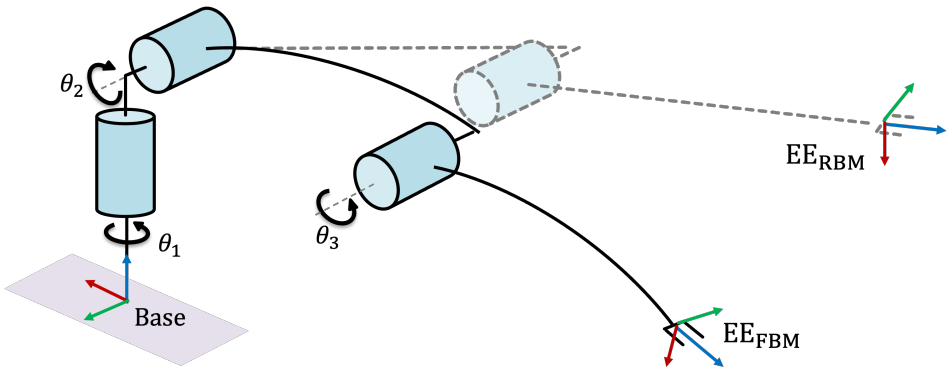

Fig. 2.19 Robot kinematic scheme considering flexible body model using finite elements (FBM, solid line) and rigid body model (RBM, dashed line).

deformations. The deformations of the link need to be monitored to evaluate the proximity to the wrinkling.

The model is developed using the software Simscape Multibody™, making use of the flexible beam element that makes use of the Euler-Bernoulli theory. It is used for control strategy validation in Chapter 4. Fig. 2.1 shows the render of a FBM of POPUP, mounted on a spacecraft.

Chapter 3

Proof of Concept

This chapter describes the development of the proof of concept for the inflatable robotic arm. The fabrication process of the first prototypes of inflatable link are described, underlining the evolution of the link design. Static and dynamic experimental tests are performed, verifying the theoretical behavior of inflatable beams described in Chapter 2.

The results of the experimental tests are implemented in a preliminary model of the robot, developed using Simscape Multibody™, a MATLAB®-based tool for physical modeling and simulation. The model is used to verify and validate the prototype robot geometry before its construction by simulating tasks with desired payload.

Therefore, the first prototype of POPUP is developed: it aims to validate the payload capacity of the structure according to theoretical analysis, study control strategies and evaluate the appropriate sensors for the application. The results demonstrate the feasibility of the project, achieving TRL 3–4, providing the proof of concept and functional verification of main components.

In this phase, materials are not the focus of the study. However, future steps for the improvement of the TRL plan the the development of a new prototype with suitable materials for space and the execution of tests in relevant environment.

3.1 Inflatable Links

The critical components of the robot are the inflatable links. Therefore, the feasibility of the project was demonstrated by the link proof-of-concept with the development of a prototype that exhibited good performance in terms of payload. In the initial stages of the project, analyses on the inflatable link were conducted to identify construction techniques, shape and appropriate materials for a proof of concept. Following works such as [41], the first attempts involved the construction of inflatable links with a pillow-like shape, as shown in Fig. 3.1.

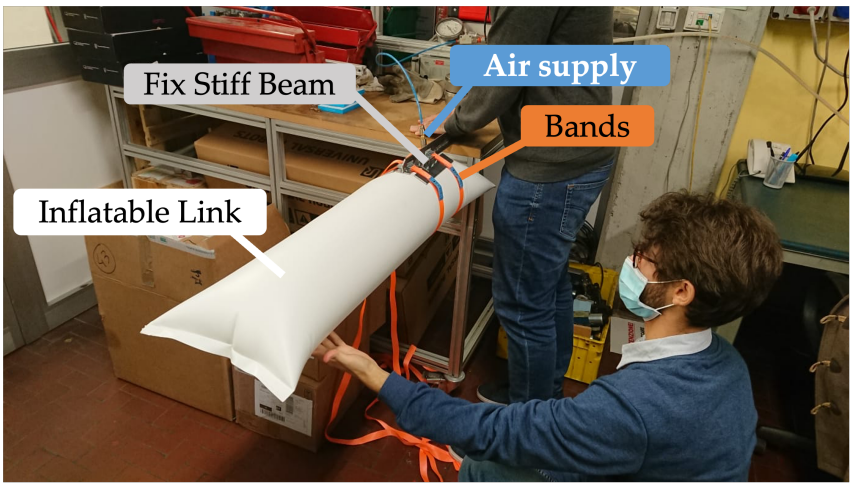

Fig. 3.1 First attempt and analysis of inflatable link.

This link could not withstand high air pressure due to the type of welding applied and it was challenging to attach it to a fixed support. Considering the inflatable robotic arm as a robot with rigid joints, it was convenient having rigid caps as the base for a cylindrical link, leading to the development of the link v1.

3.1.1 Link v1

The inflatable link prototype was designed as a cylindrical structure with pneumatic resistance. It is composed of a flexible cylindrical fabric made of polyvinyl chloride (PVC) coating, sealed by two rigid PVC caps at both ends. The caps are fastened by metal bands and gaskets to ensure structural integrity and prevent air leakage. Compressed air is injected through a valve on one of the caps. The link has a length $L = 600$ mm, radius $r = 55$ mm and wall thickness is $t = 0.5$ mm.

The static characterization of the link was performed by treating it as a cantilever beam. The objective of the tests was to determine the static behavior of the link as a function of inflation pressure, by measuring the stiffness constant k that appears in the robotic arm model. The main configuration of the components is illustrated in Fig. 3.2.

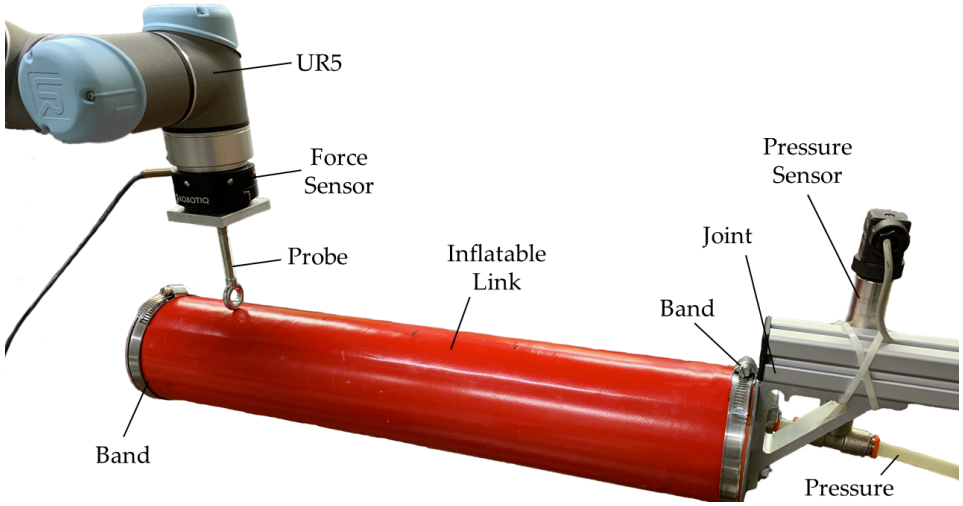

Fig. 3.2 Cantilever beam, experimental set-up.

The link is attached to a rigid structure, and the internal pressure p is measured by a pressure sensor. A pressure regulator is used to keep the pressure constant during a single test. A UR5 robot is employed to apply a position set v_{UR} to the link, which causes an angular deflection δ, as schematized in Fig. 3.3.

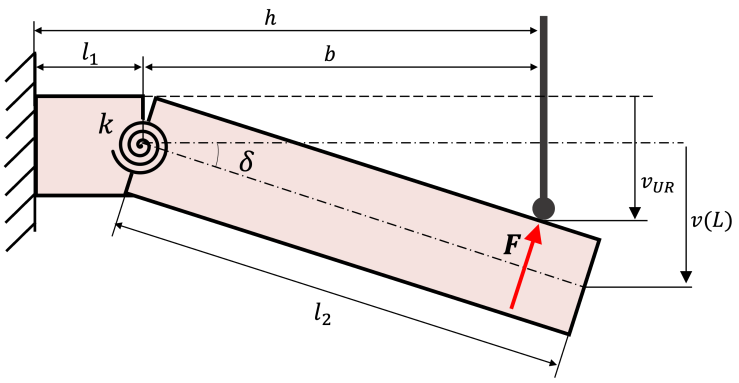

Fig. 3.3 PRBM for static tests for stiffness estimation, experimental set-up.

The rest position is defined as the zero position. The UR5 and the link interact through a probe, which reduces the contact surface and allows for a precise measurement of the distance h between the fixed joint and the probe axis. The UR5 end-effector moves orthogonally to the initial axis of the inflatable link during the tests. A force sensor is used to record the forces F exerted on the link.

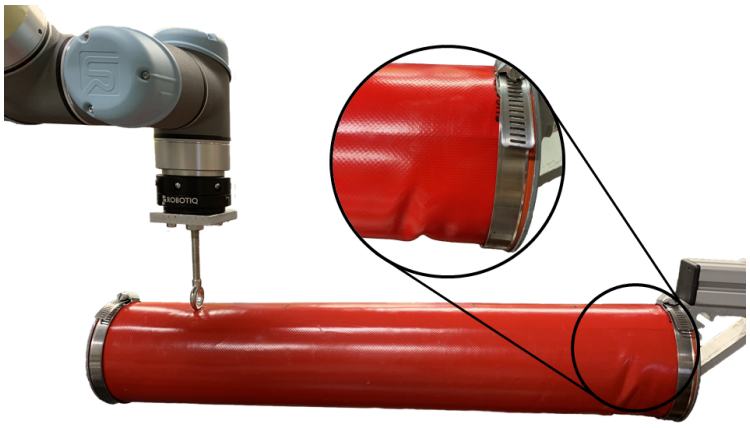

Fig. 3.4 Wrinkling phenomenon under load

The tests were conducted with a constant inflation pressure value, ranging from $p = 10$–60 kPa. The first wrinkle appeared at the distance $l_1 = 30$ mm from the fixed joint, which was considered as the length of the first body in the link model. The distance $h = 500$ mm was set for each test, and the angular deflection δ and the torque τ were computed from the measured force F and the position set v_{UR}, using trigonometric relations and small-angle approximation. The results are shown in Fig. 3.5.

To facilitate the integration of the elastic characteristic in multi-body models, an approximation can be done based on the experimental data. A linear region and a load saturation value can be identified. The saturation value identify the actual collapse moment, that is here identified as the experimental maximum moment M_{max}. The theoretical collapse moment M_c, based on a membrane approach by Wielsgosz in Eq.(2.5), underestimates the actual collapse in all tests, confirming its conservative estimation.

A linear regression is performed for each test to estimate the stiffness k. The regression is made for each test including the points under the arbitrary reference of the theoretical collapse moment M_c. The mean torque M_{max} of the points above

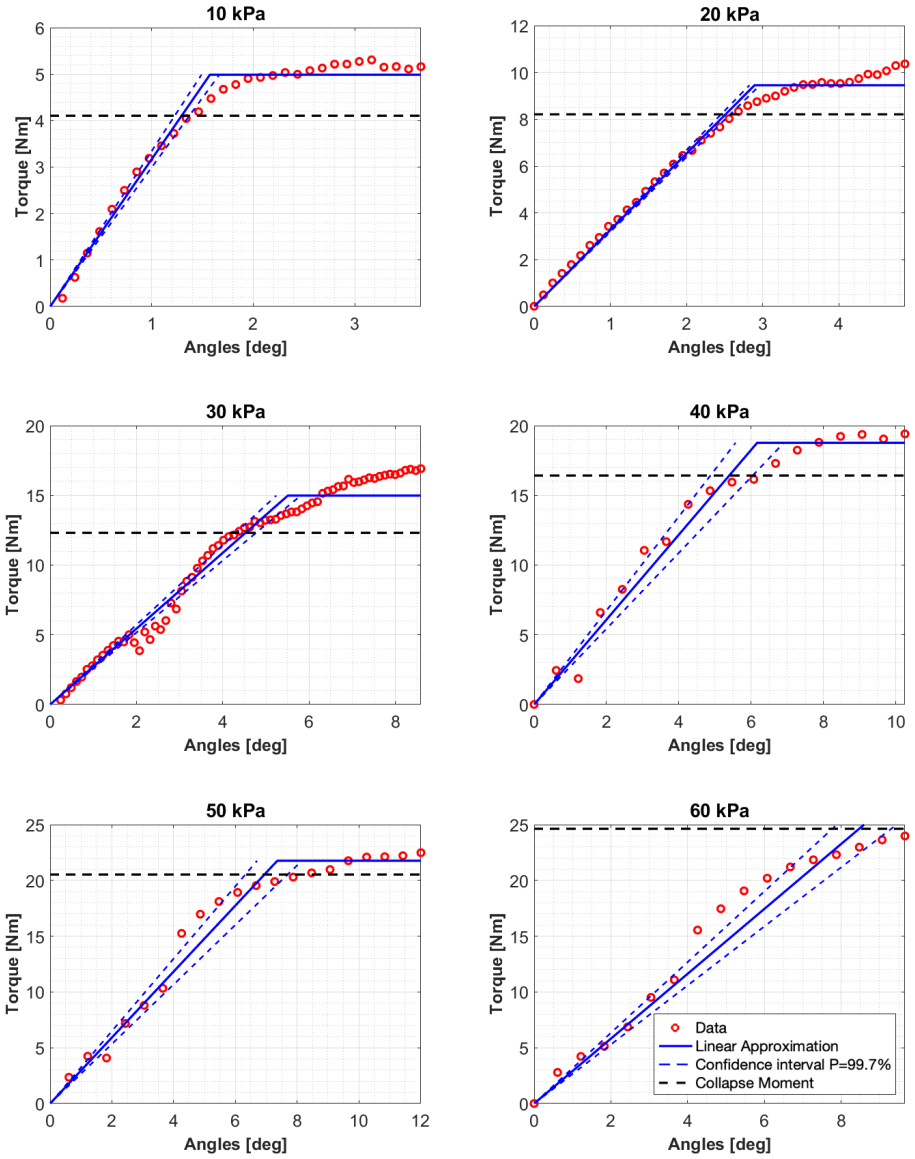

Fig. 3.5 Experimental data and linear model on varying pressures for the considered inflatable link v1.

the theoretical collapse moment M_c is used to draw a characteristic curve for the whole range of the tested angles, assuming M_{max} as a saturation value. The estimated stiffness k with its standard deviation σ_k, the theoretical collapse moment M_c and the mean maximum experimental torque M_{max} are presented in Table 3.1.

Table 3.1 Results from the static characterization of the inflatable link v1.

p (kPa)	k (Nm/rad)	σ_k (Nm/rad)	M_{max} (Nm)	M_c (Nm)
10	182.56	3.37	5.0	4.1
20	187.30	1.48	9.5	8.2
30	155.89	2.66	15.0	12.3
40	174.42	6.22	18.8	16.4
50	169.44	5.51	21.8	20.5
60	166.66	4.99	N/A	24.6

The experimental maximum moment M_{max} follows the trend of the theoretical collapse moment M_c. The internal pressure p determines the collapse moment, and thus the maximum torque the link can support. However, the estimated k values do not exhibit a clear correlation with the pressure, and their variations in the range 156–187 Nm/rad could be attributed to the quality of the support. This result is in line with the prediction by Wielsgosz in Eq. (2.5). A static characteristic of the link is obtained using the mean of the stiffness values $\bar{k} = 173$ Nm/rad.

The static characteristics exhibit some irregularities, particularly for the test at 30 kPa. A potential cause is that the cylindrical fabric is fastened to the fixed support by metallic bands that do not ensure the elimination of slippage. This factor contributes to the high variance in the stiffness estimation. Hence, a new version of inflatable link was necessary.

3.1.2 Link v2

A new version of the inflatable link was developed with the improvement of having the PVC flexible cylindrical fabric attached to the caps using glue, ensuring a better air insulation, and avoiding the use of metallic bands, resolving the problem of slippage that affected the previous version. To investigate the influence of pressure

on the bending behavior of the link, tests were conducted with a different approach. The experimental set-up is depicted in Fig. 3.6. A link prototype with the same size and material as link v1 was fixed at one end to simulate a cantilever configuration. The internal pressure of the link was controlled by a pressure reducing valve and monitored by a transducer. Both static and dynamic tests were conducted. The static tests consisted of applying a known load incrementally at the free end of the link and measuring the corresponding displacement for different pressure values. The dynamic tests aimed to evaluate the first damped natural frequency f_s of the link as a function of the internal pressure, by acquiring the power spectral density (PSD) and the frequency response function (FRF) of the link vibrations. Two accelerometers attached to the link were used to capture the free oscillations induced by an instrumented impact hammer.

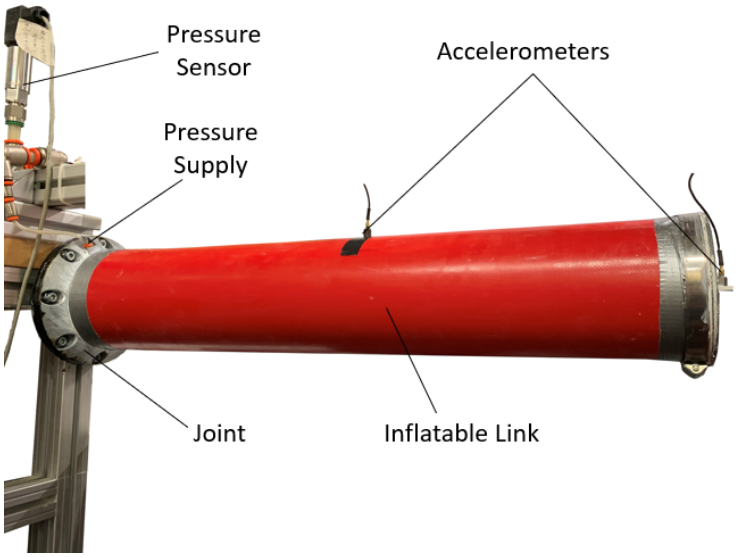

Fig. 3.6 Experimental set-up of dynamic tests on the inflatable link prototype.

The static measurements were converted in torque and angular deflection using the PRBM and setting $l_1 = 30$ mm and $l_2 = 570$ mm, based on the location where the first wrinkles appeared. The static tests, performed in the pressure range of 10–50 kPa are shown in Fig. 3.7. The static characteristic reveals a linear and a non-linear region. The collapse moment results reasonably proportional to the internal pressure, as for the collapse moment described with Eq. (2.5). On the other hand, the slope of the curves is not. Nevertheless, they show a slightly growing trend with the increase of the pressure.

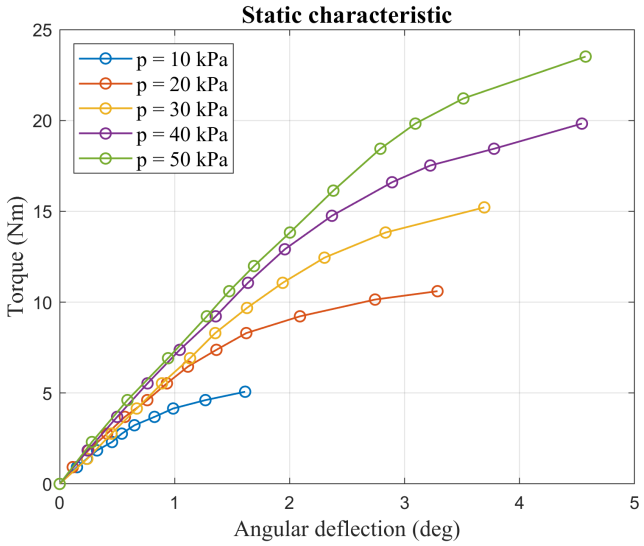

Fig. 3.7 Static characteristic of the link prototype depending on the internal pressure level.

The theoretical collapse moment M_c formulation by Wielsgosz in Eq. (2.5) underestimates the actual collapse moment, maintaining the right trend with respect with the pressure, as shown in Fig. 3.8. This result is consistent with the membrane-based formulation used in this study: the theoretical collapse moment M_c by Wielsgosz in Eq. (2.5) can be used as conservative parameter for the design of the link and the selection of the internal pressure. For instance, the theoretical collapse moment at 30 kPa is calculated as $M_c = 12$ Nm using Eq. (2.5); this demonstrates the validity of the formulation as a conservative design parameter.

The static tests showed a linear region, where a linear regression was applied to calculate the stiffness coefficient k. The theoretical collapse moment was used as an arbitrary parameter to select the points having a linear trend for all the tests. It was also used to define the saturation load of the elastic behavior. This choice is convenient for the implementation of the test results in multi-body models. Note that, theoretically, the wrinkling moment M_w delineates the linear and non-linear region. However, to approximate the elastic behavior in two segments, one for the linear region and one for the load saturation, an objective parameter is needed to select enough points in all tests for the regression. Therefore, the theoretical collapse moment of Eq. (2.5) was used.

The results indicate the dependence of the link static characteristic on the internal pressure, confirming the importance of the collapse moment M_c as indicator for the maximum load admissible, underlining its proportionality with pressure.

The dynamic tests are performed with the internal pressure in the range $p = 10$–90 kPa. From the dynamic tests, the damped natural frequency f_s is obtained from the PSD for each pressure level. As an example, In Fig. 3.9 the PSD at $p = 30$ kPa is shown.

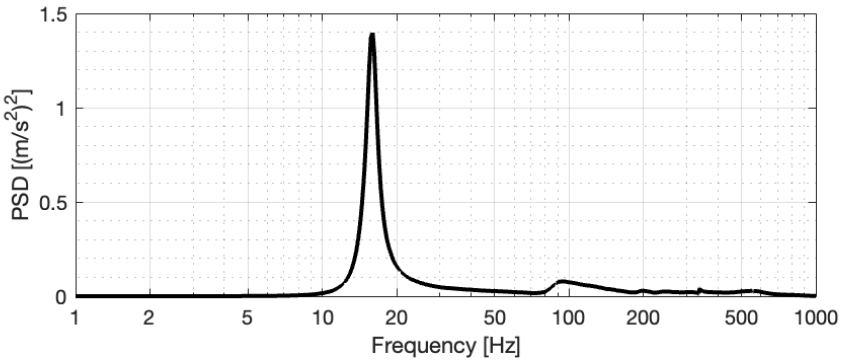

Fig. 3.9 PSD at pressure 30 kPa

The damping ratio ζ was estimated using the logarithmic decrement method:

$$\zeta = \frac{\Delta}{\sqrt{4\pi^2 + \Delta}}, \quad \text{with} \quad \Delta = \ln\left(\frac{x_n}{x_{n+1}}\right). \tag{3.1}$$

where x_n and x_{n+1} are the amplitude of subsequent peaks of the acceleration signal. an example of acquisition from an accelerometer for the test $p = 30$ kPa is shown in Fig. 3.10. The initial peaks are ignored since the signal is affected by the hammer impact.

To determine the moment of inertia I_M associated with the virtual hinge in Fig. 2.14, an iterative process was employed. The moment of inertia I_M was estimated for each test using the un-damped natural frequency f_n and the stiffness coefficient k calculated from the static tests, knowing that

$$\omega_n = 2\pi f_n = \sqrt{k/I_M} \tag{3.2}$$

and

$$\omega_s = 2\pi f_s = \omega_n\sqrt{1-\zeta^2}. \tag{3.3}$$

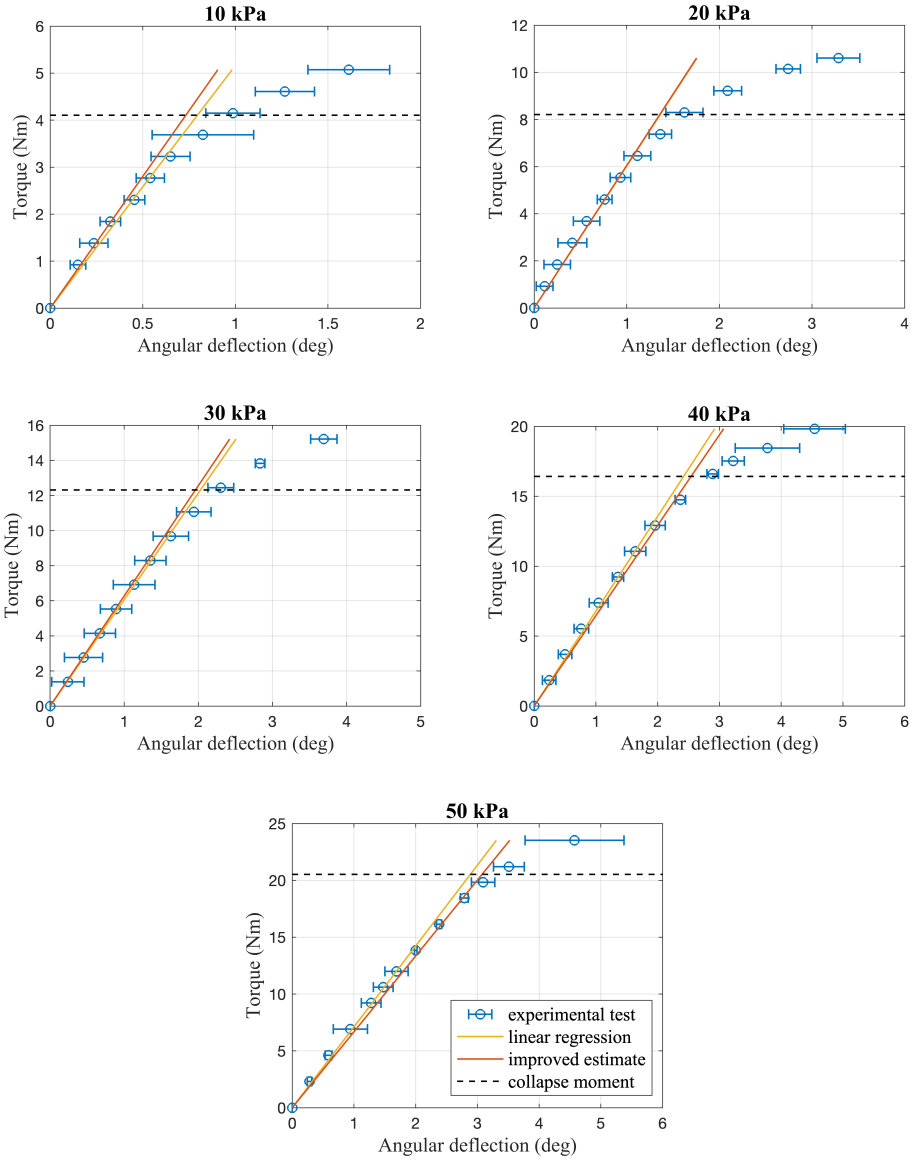

Fig. 3.8 Experimental data from static tests for each level of pressure with 99% of confidence intervals; linear regression; improved estimate; theoretical collapse moment.

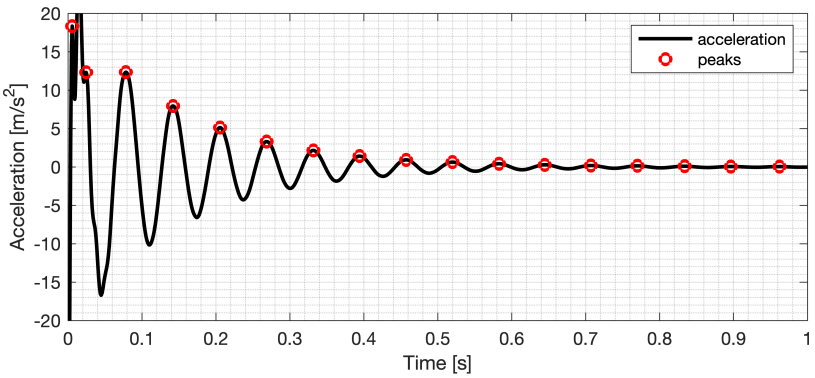

Fig. 3.10 Accelerometer signal at 30 kPa, $t = 0$ correspond to the impact instant.

Then, the average of the moments of inertia $\bar{I}_M$ was taken as a better estimate, assuming that the moment of inertia constant for each pressure level, neglecting the effect of mass increase and geometry change due to air pressure increase, i.e., $\Omega_{\varnothing} \simeq \Omega_0$ and $I_{M,\varnothing} \simeq I_{M,0}$. Backwards, from the moment of inertia $\bar{I}_M$ and the un-damped natural frequencies f_n, a refined estimate of the stiffness coefficients $\widehat{k}$ was calculated by Eq. (3.2), correcting the previous estimate, and yielding values for each pressure level of dynamic tests. Finally, the damping coefficients $\widehat{c}$ were evaluated using the damping ratio ζ and moment of inertia $\bar{I}_M$ by

$$c = \frac{\zeta}{2I_M\omega_n}. \tag{3.4}$$

The results, presented in Table 3.2, highlight the non-linear dependence of stiffness and damping coefficient on pressure, which differs from the wrinkling moment relation.

The static tests were enhanced by performing both loading and unloading of the link to reveal the presence of hysteresis. Results are shown in Fig. 3.11, where the average value of three measurements is reported. The maximum span of the hysteresis is about 0.5 deg, which corresponds to around 5 mm as the extremity displacement of the link.

Table 3.2 Results from the static and dynamic characterization of the inflatable link v2.

p (kPa)	f_s (Hz)	$\widehat{c}$ (Nms/rad)	k (Nm/rad)	$\widehat{k}$ (Nm/rad)
10	15.04	0.557	296	321
20	15.63	0.547	346	347
30	15.94	0.463	348	360
40	16.17	0.450	389	370
50	16.44	0.433	407	382
60	16.56	0.429	N/A	388
70	16.65	0.412	N/A	392
80	16.83	0.407	N/A	401
90	16.93	0.406	N/A	405

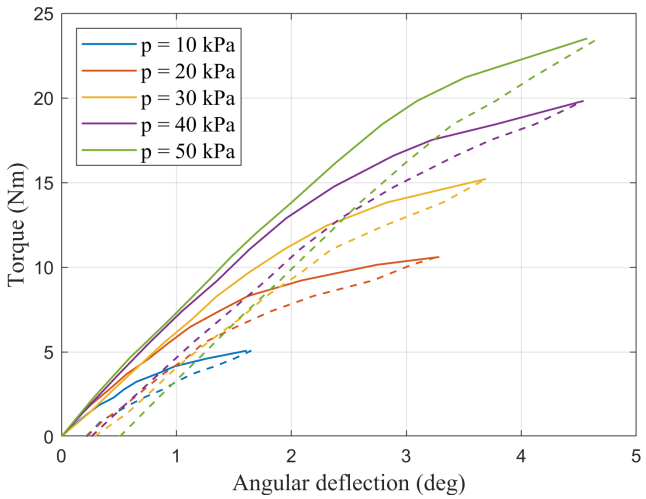

Fig. 3.11 Static characteristic of the link prototype as a function of internal pressure level, derived from progressive loading (solid line) and unloading (dashed line) tests.

3.2 Robot Prototype

This section describes the design and development process of the POPUP prototype for laboratory experiments, which aims to investigate control strategies and structural dynamics. The prototype, shown in Fig. 3.12, has a hybrid structure consisting of two inflatable links, three electric motors and rigid joints fabricated by additive manufacturing. The basic configuration of the prototype has 3 DOFs, which is the simplest feasible for a manipulator to enable position control. However, the architecture can be upgraded to 6 DOFs by adding a wrist to enable orientation control. The end-effector (EE) has a flange that allows the attachment of a robotic wrist and/or a generic tool, enhancing the degrees of freedom (DOFs) of the robot. The system includes a pneumatic line for the inflation of the links, an electronic circuit and built-in sensors.

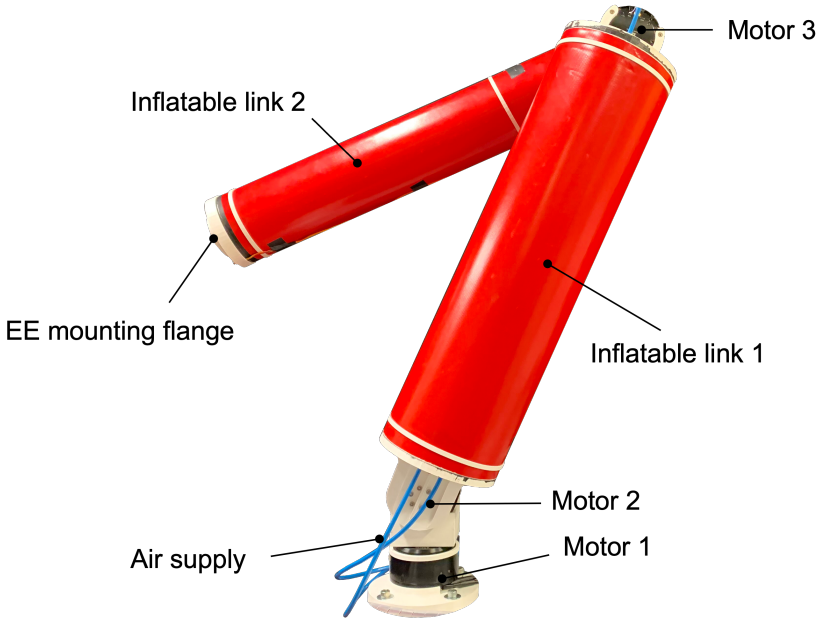

Fig. 3.12 POPUP robot prototype: inflatable links, rigid joints, electric motors and air supply.

This section presents the design process of the robot, which involves modeling the robot and analyzing its performance as a function of the pressure. The deployment is tested and the feasibility of the project is demostrated. A discussion on the sensorization and control strategy of the robot is provided, further details are given in the next chapter. Moreover, a remote control system using a joypad is implemented and tested.

3.2.1 Mechanical Parts and Models

The design process started with the robot architecture that consisted of 3 motors and 2 inflatable links, as shown in Fig. 3.13.

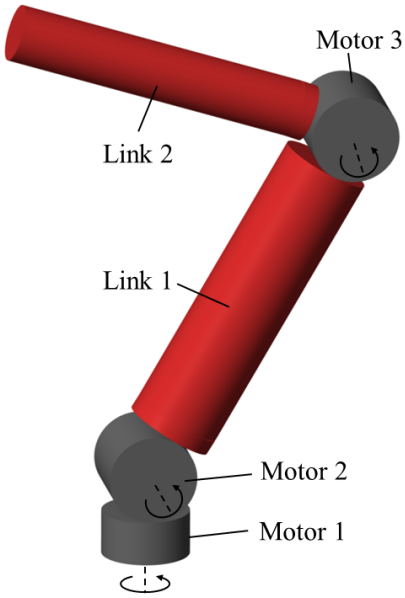

Fig. 3.13 POPUP preliminary architecture.

The robot prototype was designed based on the results of the link testing. The wrinkling moment $M_w = M_c/2$ derived by Wielsgosz in Eq. (2.5) was used for sizing, since it predicts in a conservative way the operating region for the robot where wrinkles do not occur. It is essential that the robot operates far from the wrinkling conditions in order to be approximated to a conventional manipulator with flexible links and using linear models for links, e.g., Euler-Bernoulli beam theory.

The specifications of the first prototype of the robot are presented in Table 3.3. The link length was set to $L = L_1 = L_2 = 600$ mm, the link 1 radius to $r_1 = 85$ mm, and the link 2 to the same as the prototype used for the tests, with a radius $r_2 = 55$ mm. Dimensions was calculated using the wrinkling moment formulation in order to reach a payload of 20 N, without showing wrinkles, at a pressure of 60 kPa. Since robot links have been successfully tested in the range 10–90 kPa, the prototype payload can reach 30 N. The payload is evaluated considering a fully extended configuration of the robot, that is the configuration where the maximum external moment is applied to the robot links. Robot prototype links are attached to the plugs using glue, as for link

v2. The robot reaches a full extended length of 1.4 m. To support a payload of 20 N, the shoulder motor must explicate a torque of 42 Nm. The selected motors for the joints are brushless, with 80:1 reduction ratio, having a radius of 49 mm, a thickness of 62 mm and, mass of about 0.8 kg each, rated torque of 48 Nm and peak torque of 144 Nm. Since the biggest contribution to the mass is due to the motors, the robot mass is under 4 kg. The mass account does not consider power supply generators or the tank, since not yet available as ad-hoc allocation. The structure of the three joints of the robot, which is designed to accommodate the motor, was initially made in PLA by additive manufacturing, to expedite the prototyping process.

Table 3.3 Specifications of the robot prototype for laboratory testing.

Parameter	Value
Nominal Pressure	60 kPa
Link 1 length	600 mm
Link 2 length	600 mm
Link 1 radius	85 mm
Link 2 radius	55 mm
Payload	20 N
Weight	4 kg

Since the wrinkling formula is derived from a static analysis, a dynamic model was developed, incorporating the design specifications, to evaluate its performance in dynamic tasks. The dynamic simulation of the robot with flexible links was performed using Simscape Multibody™ software. The pseudo-rigid body model (PRBM) was adopted, incorporating the designed geometry, and deriving the elastic and dissipative parameters from the experimental data. In Fig. 3.14, the POPUP robot rendering with PRBM is shown. The robot kinematics respects the PRBM scheme illustrated in Fig. 2.14.

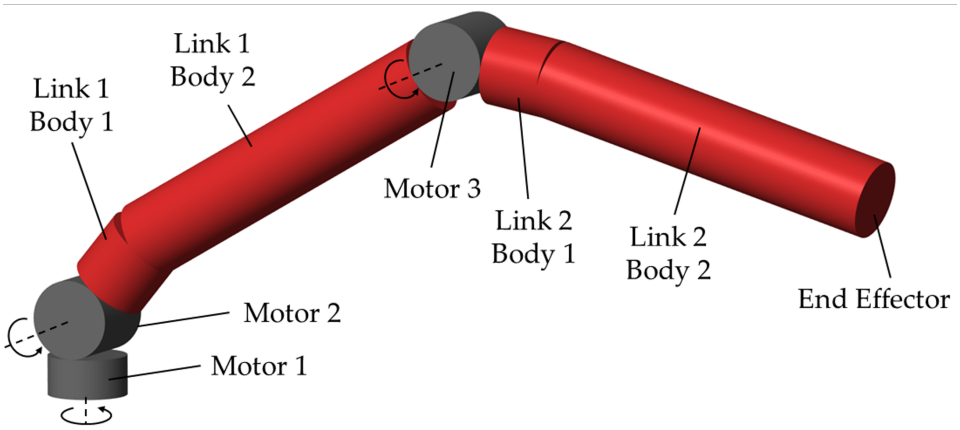

Fig. 3.14 POPUP robot rendering with a preliminary PRBM.

The stiffness coefficients of link 1 were derived from those of link 2, using the well-known formula used for lumped-parameter methods $k = EI/\ell$, where E the material Young's modulus, I the second moment of area and ℓ the length of the beam unity, i.e., l_2 in this case. Since the only difference between link 1 and link 2 is their cross-sectional area, the stiffness coefficients were scaled by the ratio of the area moments of inertia of the links: $k_1 = k_2 \cdot I_1/I_2$. The stiffness value is a function of the pressure, as reported in Table 3.2. The elastic behavior is approximated by adding a saturation term to account for the collapse moment, which is the point at which the reaction moment does not increase with increasing deflections, as illustrated in Fig. 3.15 for the specific case of $p = 30$ kPa. Therefore, the stiffness is non-linear and $k = k(p, \delta)$. The damping coefficient of link 1 was assumed to be proportional to the stiffness coefficient as a first approximation.

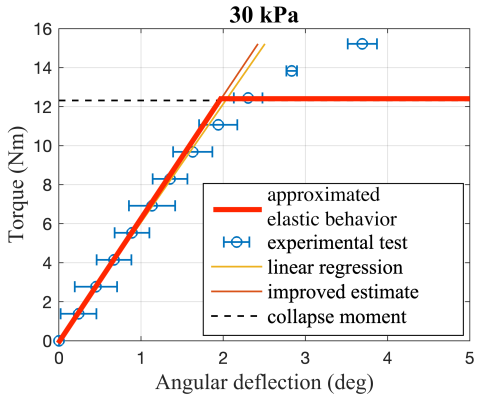

Fig. 3.15 Estimation of the stiffness of the link for the virtual joints for $p = 30$ kPa.

Tasks are executed with different pressure levels and different masses attached to the end-effector to assess the robot dynamic performance and prevent the collapse of the links. As an example, in Fig. 3.16 the angular deflection δ_4 is shown during the execution of a robotic movement with two different pressure levels: at $p = 10$ kPa the link cannot sustain the load and collapses, exhibiting high deformation, while at $p = 30$ kPa the performance is acceptable and the link shows linear behaviour.

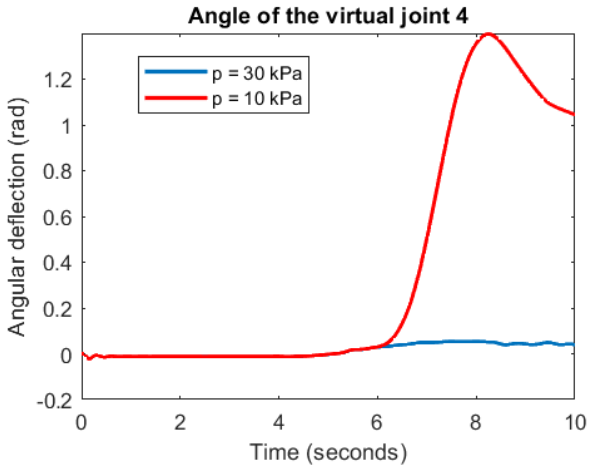

Fig. 3.16 Angular deflection of the virtual joint 4 for a task performed with mass of 2 kg on the EE, at different pressure levels.

The use of the dynamic model is fundamental to properly set maximum joint accelerations and link pressure level in relation to a specific task. Simulations validated the preliminary link dimensions, enabling the advancement of the definitive CAD design and robot manufacturing.

Rigid parts are made by additive manufacturing, using PLA for the first prototype. The cylindrical surface of the links is made by wounding a sheet of polymeric material. On the extremities two rigid rings are glued. The rings permit the links to be fixed through screws to the other joints, as shown in Fig. 3.17, allowing the possibility to add elements, e.g., sensors, inside the links during development stages. The motor joints represent the link tops and guarantee their isolation by using seals.

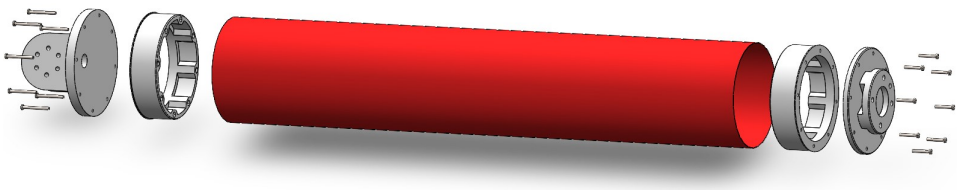

Fig. 3.17 Exploded view drawing of the inflatable link 2 prototype.

Finally, the robot prototype for laboratory testing was ready, as shown in Fig. 3.12. The PRBM was updated in Simscape Multibody™, including the accurate masses and the developed CAD, as shown in Fig. 3.18.

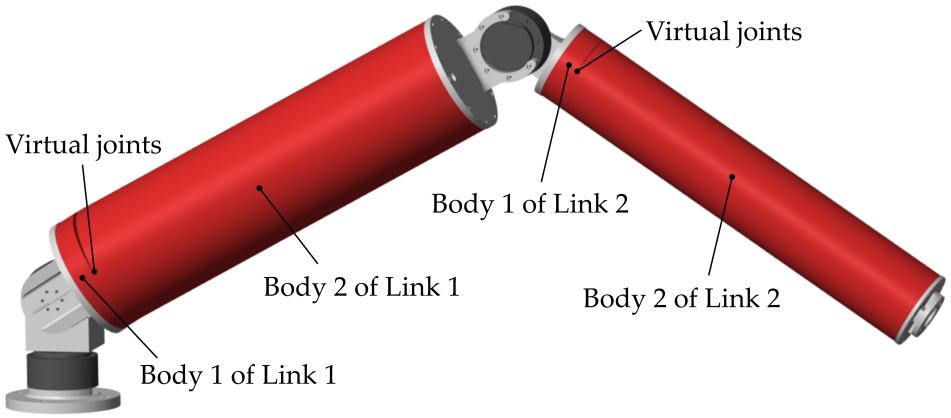

Fig. 3.18 Graphic output of multi-body model.

Although dynamic parameters were estimated by tests on the individual links, the estimations may not reflect the behavior of the new link due to the lack of repeatability of the link elastic behavior in the current manufacturing process. Hence, an identification of robot dynamic parameters, performed using robot movements, is required to enhance the accuracy of the system model. Alerts indicating a wrinkling condition was implemented, monitoring virtual joint reaction torques.

The Denavit–Hartenberg (D-H) parameters of the robot PRBM are shown in Table 3.4.

Table 3.4 Prototype D-H parameters, PRBM with virtual joints.

Link	a_i (mm)	α_i (rad)	d_i (mm)	ϑ_i (rad)
0	0	$\pi/2$	152.7	θ_1
1	94	$-\pi/2$	39.4	θ_2
1.1	0	$\pi/2$	0	δ_1
1.2	634	π	0	δ_2
2	94	$\pi/2$	157.8	θ_3
2.1	0	$-\pi/2$	0	δ_3
2.2	590	0	0	δ_4

Using the RBM, the Unified Robot Description Format (URDF), which is an XML format for describing a robot model, was created to facilitate the import of the POPUP prototype model in software such as Gazebo, as shown in Fig. 3.19. This aims to establish the foundation of a robot control developed in the ROS environment, which is essential for modern robotic applications.

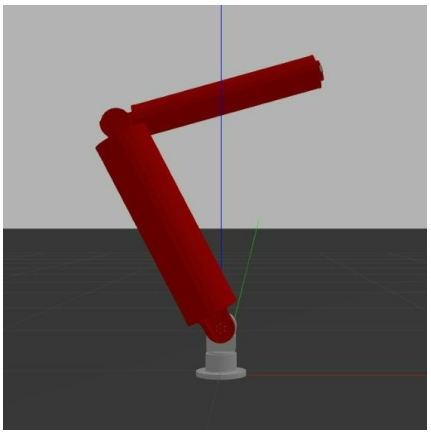

Fig. 3.19 Graphic output of Gazebo model.

Finally, a wrist can be attached to the end of the robot to achieve 6 DOFs. A spherical wrist is preferred since it simplifies the inverse kinematics problem by separating the position and orientation subproblems. Thus, the first three joints are responsible for position control and the spherical wrist for orientation control. A spherical wrist consists of three revolute joints with the actuation axes that converge at a common point. A preliminary wrist design, actuated by stepper motors and shown in Fig. 3.20, was developed to be mounted on the prototype.

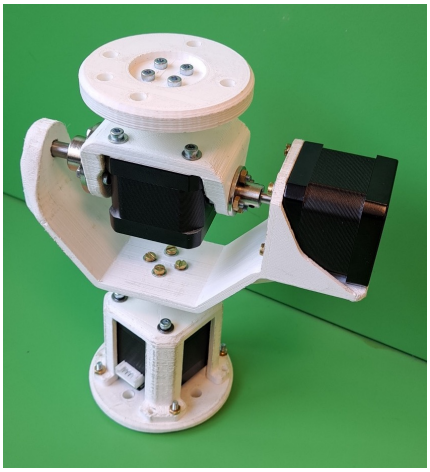

Fig. 3.20 Spherical Wrist prototype.

3.2.2 Pneumatic Line and Deployment

The system architecture is shown in Fig. 3.21 where the pneumatic line and the electronic circuit are schematized.

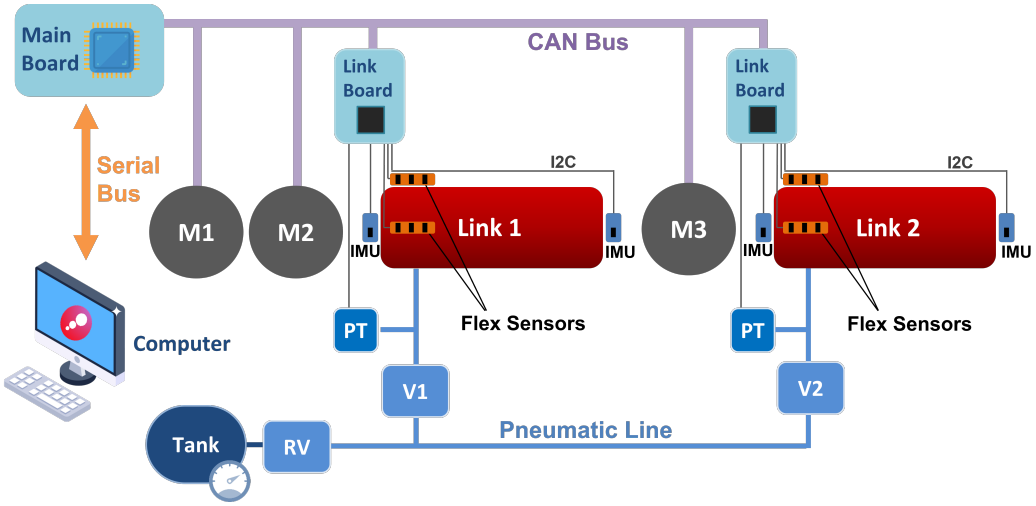

Fig. 3.21 System architecture scheme: motors (M), links, inertial measurements units (IMUs), flex sensors, pneumatic line, main and link boards, computer.

A pneumatic line controls the inflation and deflation of the links. Pressure supply is regulated by a pressure reducing valve (RV) that provides pressure in the tested working range of 10–90 kPa. Internal pressure is measured through pressure transducers (PTs) mounted in proximity of the links. Compressed air can be supplied

by a pressurized tank or an external pneumatic plant. Two valve groups, V1 and V2 for link 1 and 2 respectively, can provide pressure or deflate each link separately. Valve groups consists of two digital valves: one connects the link with supply and the other one empties it. Valves are normally closed to avoid energy waste, since they are activated only for inflation and deflation stages.

Links can be independently inflated and deflated to optimise the control of the deployment procedure. Once deployed and reached the working configuration, the pneumatic supply can be disconnected, although a by-pass should be considered to compensate for air losses and maintain constant internal pressure. The tank, pressurized at 30 MPa and having a volume of 2 dm^3, enables inflating both links at a pressure of 50 kPa more than 10 times.

A demonstration of the deployment stage was performed and shown in Fig. 3.22. The robot can be compactly stored in a box with a volume $0.3 \times 0.3 \times 0.4$ m when it is deflated, while it can reach an operational workspace of 1.4 m in radius when it is fully inflated and approximated by a sphere. The deployment process consists of several steps that ensure the proper alignment and stability of the robot. First, link 1 is inflated until the pressure sensor indicates the desired internal pressure value. Then, link 2 is inflated to complete the deployment. The robot is equipped with sensors that monitor the status and outcome of the operation. In the current prototype, the robot requires manual assistance for packing after deflation.

3.2.3 Sensors and Control Strategy Concepts

Fig. 3.21 illustrates the initial hardware and sensor configuration that was subject to continuous evaluation and modification over time, in relation to the control strategy that was intended to be further developed.

A computer is connected to the main board and manage robot tasks. The main board, responsible of the robot control, communicates with link boards and motors by CAN-bus. Generally, each link is equipped with a dedicated board, called link board. Link boards acquire information from different transceivers and sensors, using I2C communication bus. These boards can be by-passed depending on the complexity of signals from link sensors to manage.

Two control strategies for the robot are considered and further discussed in Chapter 4: one based on link state estimation and the other based on visual servoing.

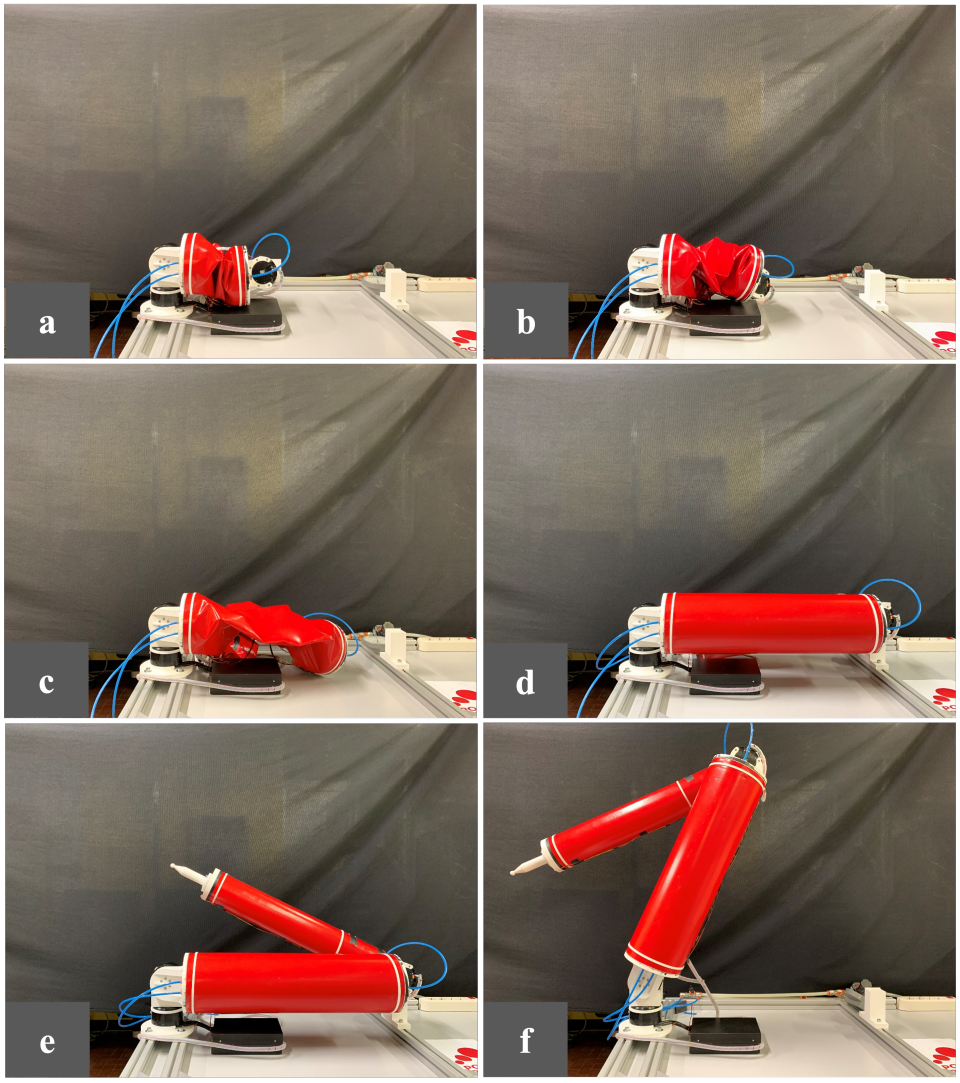

Fig. 3.22 Deployment stage of the inflatable robot prototype. Deflated configuration (a), start of the inflation of link 1 (b), continuation of the inflation (c), inflation of link 1 completed and start of inflation od the link 2 (d), links inflated and stabilizing (e), robot inflated and in working configuration (f).

The first strategy focuses on the estimation of the link state to construct the inverse and forward kinematics of the robot by the PRBM. The PRBM was chosen as a suitable compromise between accuracy and computational effort, especially regarding the inverse kinematics. In this case, the sensors must estimate link deflections $\boldsymbol{\delta}$ and corresponding velocities $\dot{\boldsymbol{\delta}}$.

Hence, each link was equipped with sensors that provide an estimation of link deflections. Inertial measurement units (IMUs) were mounted on link extremities providing accelerations and absolute orientations from which the link deflections can be computed. Four flex sensors were positioned around the link cylinder region with higher static stress, i.e., the extremity closer to robot base in the kinematic chain. Additionally, as shown in Fig. 3.23, a camera system was assessed to be placed inside the link on the extremity closer to the base, facing towards the opposite side, where a 2-dimension marker, e.g., an Aruco marker [90], could be positioned. A similar strategy was conducted in [91], where a built-in vision sensor was used for the deformation estimation of an inflatable link. Throughout vision algorithms the transformation matrix between camera and marker can be built.

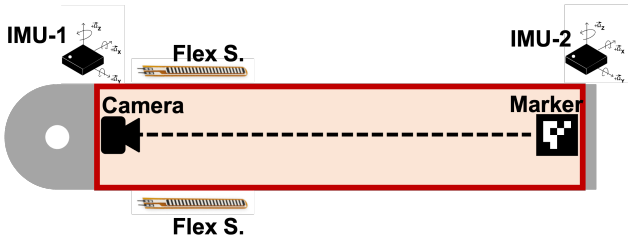

Fig. 3.23 Link sensors for link state estimation: IMUs, flex sensors and camera with marker.

Sensor fusion and state estimation techniques, e.g., Kalman filter (KF) [92], using information by sensors, can be employed to estimate actual link state to properly control the robot, reducing inaccuracies due to the non-linearities of the system.

Fig. 3.24 shows an example of control strategy based on link state estimation. In this strategy, the PRBM estimates the link deflections and velocities from the sensor measurements and constructs the inverse and forward kinematics of the robot. An optimal control technique, such as Model Predictive Control (MPC) or Linear Quadratic Regulation (LQR), can be used to optimize the parameters of the robot dynamic model, and to ensure high performance in positioning.

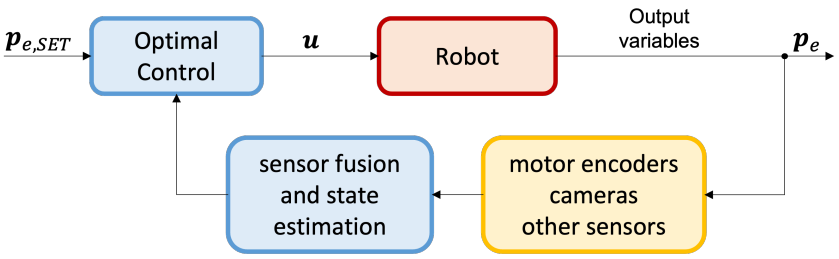

Fig. 3.24 Scheme of the control strategy: end-effector set position $\boldsymbol{p}_{e,SET}$, motor input $\boldsymbol{u}$ and end-effector actual position $\boldsymbol{p}_e$.

The deformations measured by the sensors are useful for two purposes: first, to obtain a more accurate estimate of the end-effector (EE) position through direct kinematics, and second, to monitor the link condition and detect the occurrence of wrinkling.

The installed IMU was the MPU-9250 by TDK InvenSense. It combines two chips: the MPU-6500 that contains a three-axis gyroscope, a three-axis accelerometer, and an onboard processor able of processing sensor fusion algorithms; and the AK8963, a three-axis digital compass. The resistive flex sensors by Spectra Symbol with length of 95 mm was tested. The flat resistance is 10 $k\Omega \pm 30\%$. The resistance increases in the circuit following the component bending, however a precise characterization is not supplied. To assess the performance of the flex sensors, static tests were carried out to measure their accuracy in detecting the virtual joint angles. The flex sensor was installed on an harmonic steel foil. For static tests the sensor output was measured for progressive static deflections, using a screw mechanism. The results showed that the flex sensors had a large error margin and were not suitable for the intended application, which required high precision and reliability. A strong dependence on temperature was detected and non-linear behavior for angles smaller than 20 degrees was measured. Therefore, alternative sensors should be explored for future work. One possible option is to use optical fiber sensors, which have high accuracy and sensitivity in measuring bending and deformation. However, these sensors are also expensive and complex to implement, which poses a challenge for their integration into the system, and the possibility of their use is not investigated in this phase.

The second strategy relies on visual servoing. A depth camera can be mounted on EE to identify the target and performing grasping operations with an accuracy that does not depend on the link state estimation: the camera can evaluate a relative

positioning error between EE and target, producing a velocity set with respect to EE, allowing target following. More complex cameras systems can be evaluated, e.g., additional cameras can be positioned on base to develop advanced logic for robot state estimation and for target identification, following and grasping.

Fig. 3.25 illustrates an example of experimental set-up for the visual servoing control. A Intel® RealSense™ camera is mounted on the EE of the robot and another one is mounted on a support in a fixed position with respect to the robot base frame. The camera can provide both 2D and depth 3D images. In this example, the 2D-RGB camera is used to detect an Aruco marker that represents the target to grasp. By using vision algorithms in the software tool OpenCV the four corners of the marker in the image are detected and, after a calibration procedure, the pose of the marker relative to the camera can be estimated [90]. This pose information can then be used to compute the desired EE velocity based on the pose error, guiding the robot EE toward the target, compensating for small link deformations. The strategy is further discussed in Chapter 4.

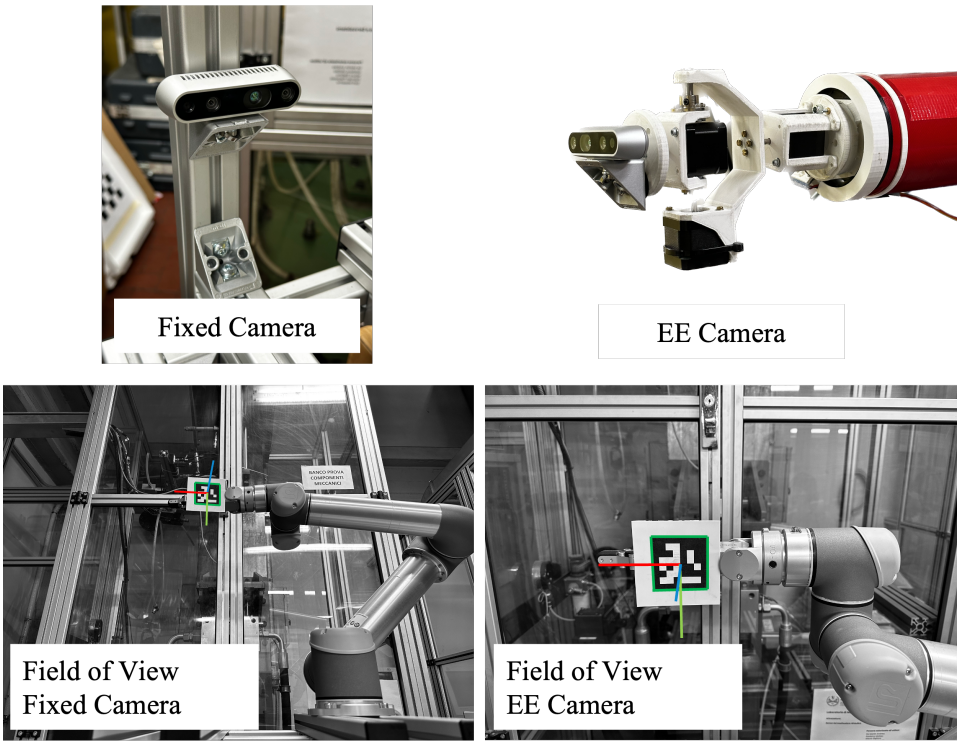

Fig. 3.25 Visual servoing based on Aruco markers

A 3D tracking system, OptiTrack, is on the way to be installed in the laboratory workspace to monitor and record the deformations of the inflatable robot during various tasks. OptiTrack is a high-precision system that uses depth cameras and physical markers to track the position and orientation of objects in 3D space. Therefore, markers need to be attached to the robot, forming rigid bodies that can be recognized by the depth cameras. An example of marker placement on the robot flange is shown in Fig. 3.26. The data collected by OptiTrack can be used to evaluate the robot performance and to compare it with the developed model, which aims to capture the dynamic behavior of the robot. The data is also useful for estimating the dynamic parameters of the robot and for developing a digital twin model.

Fig. 3.26 OptiTrack Markers mounted on the robot flange

3.2.4 Teleoperation and Control Implementation

To control the robot, the first step is to send velocity commands to the motors that actuate its joints. A teleoperation system is designed to enable the remote control of the robot using a joypad device as the human interface. The control algorithms are developed in the ROS (robot operating system) framework, which facilitates the integration and scalability of the software components.

The main board of the robot, a STM32H7 microcontroller, runs a ROS node written in C language that subscribes to the velocity commands and publishes the motor feedbacks. The motor drivers, VESC boards, implement PID (proportional-integral-derivative) controllers to regulate the speed of the motors. The main board

and the motor drivers communicate via CAN (controller area network) protocol, exchanging setpoints and measurements.

The main board is connected via USB to a computer that runs another ROS node written in Python language, which handles the teleoperation logic. Two control modes can be enabled: in the joint space and in the cartesian space. This node reads the signals from the joypad device and converts them into velocity commands for each joint of the robot, with values that can range from -0.1 to 0.1 rad/s. In the cartesian space control mode the conversion into joint commands is made using the Jacobian matrix of the rigid body model (RBM). The joypad axes are mapped to the corresponding joints of the robot according to a predefined scheme. In Fig. 3.27 the scheme of the telecontrol logic is shown.

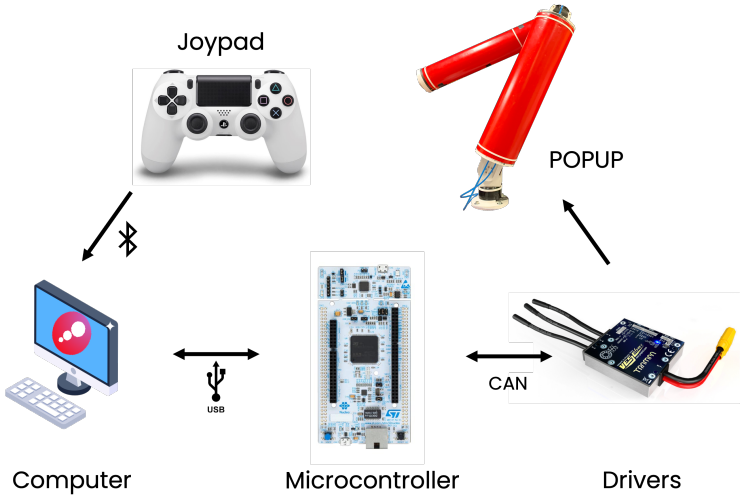

Fig. 3.27 Telecontrol scheme.

The inflatable links showed high resilience and stability in different robot motions. The robot demonstrated to support a payload of 2 kg. However, the implementation of control strategies based on visual servoing was hindered by some technical problems with the motor drivers, which prevented the integration of the vision system with the robot. These control strategies were previously tested on conventional robots and proved to be feasible and effective, as described in Chapter 4.

3.2.5 Microgravity test rig

Demonstrated the feasibility of the proposed solution from a structural and mechanical point of view using generic purpose materials, links with appropriate materials for space applications are currently in development. These links have to be integrated in a new robot prototype, with larger dimensions, aimed to simulate a relevant space environment. A preliminary design is developed for the construction of an inflatable robot with planar motion, using a test rig able to simulate microgravity conditions by using air bearings, as shown by Fig. 3.28.

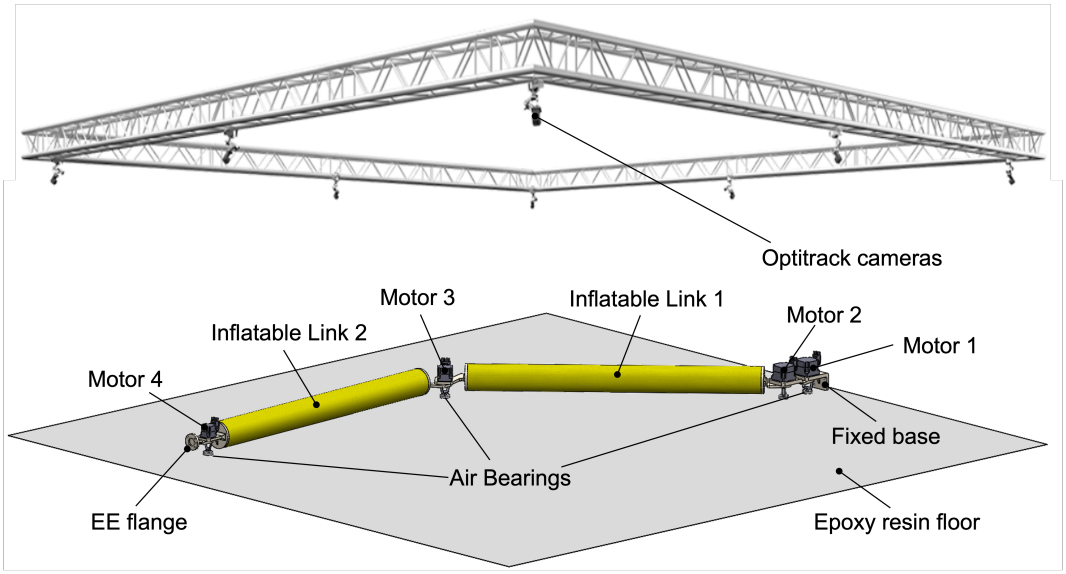

Fig. 3.28 Microgravity test rig: planar robot prototype and OptiTrack camera system.

The robot will have four axes to provide redundancy of DOFs. Each links will have $L = 1.0$–1.5 m and $r = 50$–70 mm. OptiTrack tracking system will be installed to provide precise data about the robot motion, which can be used for the model validation. Cameras will be integrated on the robot EE and base for the implementation of visual servoing control, which can compensate for the link deflection and achieve accurate positioning, as further discussed in Chapter 4.

Chapter 4

Control

This chapter explores how to control the robot effectively despite its flexibility and inflatable nature. The control algorithms were validated using simulation models. The models were developed concurrently with the prototype of the robotic arm, mitigating practical issues related to the project, such as delays in the procurement of components, e.g., electric motors and electronic boards. The use of models facilitates the modular integration of different code segments and algorithms for various applications in an agile manner. Furthermore, models allow the simulation of microgravity conditions and the creation of a space environment with the robot mounted on a spacecraft for space application tasks, aiming for advanced control strategies.

Various approaches and techniques have been explored to monitor and control the state of the inflatable links. As presented in Chapter 3, the initial focus was on using embedded sensors and simplified models, such as PRBM, to estimate the link states. The estimates of link deflections by the sensors mounted on the link could be combined with deflection estimation based on motor torques and positions. To improve the link state estimation, the sensor fusion can be applied by using Bayesian estimators, such as Kalman filters [93, 92]. In Section 4.1, an elastostatic approach based on PRBM is employed to estimate the load and pose of the links, as well as to compute the inverse kinematics of the robot [94]. This approach has some limitations, such as high computational cost, dependency on uncertain parameters, and potential inaccuracies due to model simplifications. Another challenge faced during the development of the robot was the implementation of reliable and accurate

sensors to compensate for possible link deflections. However, the idea of using motor torques to estimate the link state is still valid and requires further investigation, especially for detecting critical conditions such as wrinkling or excessive load.

This considerations led to the study of vision-based methods for the control of POPUP, that has proven to be effective. The advantages of this method are that it does not strictly require link deflection information or simplified models.

Visual servoing is a technique that uses visual feedback from a camera or other vision sensor to control the motion of a robot. It can be seen as a sensor-based control method that combines image processing, computer vision, and control theory [95]. In this work, a position-based visual servoing (PBVS) is considered: the control law is based on the error between the current and desired poses of the target object or the robot end-effector in Cartesian space. PBVS requires a model of the target object and a method to estimate its pose from visual features. It can handle large motions and changes in viewpoint with respect to image-based visual servoing (IBVS), where the the error between the current and desired positions of visual features on the image plane, such as points, lines, or moments, without requiring the estimate of the pose. PBVS is accurate and easy to implement. As drawbacks, it is sensitive to calibration errors, sensor noise and occlusions.

There are different ways to perform pose estimation of an object thought vision-based algorithms. Basically, two different kind of camera can be used: RGB cameras that capture only the color information of a scene, and RGB-D cameras that also capture the depth information, i.e. the distance of each pixel from the camera. RGB-based methods can rely on markers on the target object, e.g., Aruco markers [90], extrapolating the 3D pose knowing the dimension of the marker and the camera parameters. In absence of markers, the top-performing methods rely on RGB-D image channels. However, the progress in deep neural networks (DNNs) allow to achieve good results results when only RGB channel are used [96]. The use of vision-based control is common in robotics [97–99], and the details of the pose estimation procedure are beyond the scope of this work, as they are well-established in the literature.

The objective of the proposed vision-based control strategy simulation is not to evaluate and quantify the sensor precision or accuracy of pose estimation techniques, since these depend on the sensors and artificial intelligence (AI) algorithms, which have high variability in the literature as shown by the examples mentioned. The

simulation aims to verify the control strategy under the assumption that the vision system provides the correct estimation, in order to validate the strategy considering only the complexity of the robot architecture. Experimental tests are expected to be performed by using Aruco markers as described in Chapter 3.

In Section 4.2 the vision-based control strategy is presented, using current prototype models [100]. The tests carried out with the control for the prototype showed interesting results for the final application, with the addition of the fact that gravity is present, representing a worsening condition in terms of performance.

In Section 4.3 the developed control strategies were adapted to models designed for one of the possible space applications. In particular, a chaser spacecraft is equipped with the inflatable robotic manipulator to capture a resident space object (RSO) using a grapple fixture [101]. The aim is to demonstrate that the inflatable robot, for the space applications it is designed for, can be treated as a conventional robot under certain assumptions. What may differ from conventional robots are the issues that stem from the nature of the robot that unfolds during the deployment or from manufacturing defects that result in geometric errors after the robot development, such as imperfect seams. By employing a material with a high elastic modulus, such as Kevlar™, the robot can achieve low deflections in space applications where the accelerations are properly set. Furthermore, as discussed in Section 4.3, the link stiffness is not significantly affected by the internal pressure, unlike existing robots with stiffness-controllable links [46] made with materials having low elastic modulus. Finally, It is shown how such vision-based control techniques are compatible with the inflatable robot and can be successfully applied.

4.1 Elastostatic approaches

Elastostatic approaches are used to estimate load and pose estimation of the robot accounting for deflection or to perform the inverse kinematics if load is known. In the following, the PRBM is used, as described in Fig. 2.18. A robot with 3 actuated joints is considered, resulting in a 7-DOF robot using PRBM. The main hypotesis is that joint torques $\boldsymbol{\tau}$ are composed by the motor torques $\boldsymbol{\tau}_\theta$ and virtual spring torques $\boldsymbol{\tau}_\delta$ are defined as:

$$\boldsymbol{\tau}_\delta = -\boldsymbol{K}(p) \cdot \boldsymbol{\delta}, \tag{4.1}$$

where $\boldsymbol{K}(p)$ is the stiffness matrix depending on pressure p, containing the stiffness values k_i of each joint i. The joint variables are expressed by

$$\boldsymbol{q} = [\theta_1, \theta_2, \delta_1, \delta_2, \theta_3, \delta_3, \delta_4]^T. \tag{4.2}$$

Moreover $\boldsymbol{g}(\boldsymbol{q}) = \boldsymbol{0}$, since a space application is considered. Set the pressure, the stiffness value of each joint is a scalar number and the model is linear, with the assumption that:

$$\|\boldsymbol{\tau}_\delta\| \leq M_w. \tag{4.3}$$

This condition must be continuously monitored and respected during the simulated tasks. In alternative the non-linear model could be implemented, considering the post-wrinkling condition. However, the robot should never operate in such a condition, so the analysis is focused on the linear area.

4.1.1 Load and Pose estimation

The external load acting on the system can be estimated by a recursive algorithm based on the elastostatic approach. Known the load, the deformation of the flexible link can be calculated, and the pose estimation of the robot can be performed.

The motor torques $\boldsymbol{\tau}_\theta$ and positions $\boldsymbol{\theta}$ are considered as known parameters. In a real case, appropriate sensors can be used to provide these quantities. The external forces $\boldsymbol{f}_e = [f_{e,x}, f_{e,y}, f_{e,z}]^T$ act on the robot end-effector (EE) and the external torques are assumed null $\boldsymbol{\mu}_e = [0,0,0]^T$. In addition, space application is considered, so weight force is set to zero in the algorithm. An elastostatic approach is adopted to solve the problem. The Jacobian matrix is $\boldsymbol{J} = [\boldsymbol{J}_1, ..., \boldsymbol{J}_7]$, with

$$\boldsymbol{J}_i = \begin{bmatrix} \boldsymbol{z}_{i-1} \times (\boldsymbol{p}_e - \boldsymbol{p}_{i-1}) \\ \boldsymbol{z}_{i-1} \end{bmatrix}, \tag{4.4}$$

where $\boldsymbol{z}_{i-1}$ is given by the third column of the rotation matrix $\boldsymbol{R}^0_{i-1}$, $\boldsymbol{p}_e$ is the position vector of the EE and $\boldsymbol{p}_{i-1}$ are the position vectors of the origins of frames $i-1$, according to the Denavit–Hartenberg convention [102]. The following equation is valid:

$$\boldsymbol{\tau} = \boldsymbol{J}^T \cdot \boldsymbol{\gamma}_e, \tag{4.5}$$

where $\boldsymbol{\tau}$ is the torque vector and $\boldsymbol{\gamma}_e = [\boldsymbol{f}_e^T, \boldsymbol{\mu}_e^T]^T$ represents the external load. Considering only the motor torques $\boldsymbol{\tau}_\theta$:

$$\boldsymbol{\tau}_\theta = \boldsymbol{J}_\theta^T \cdot \boldsymbol{\gamma}_e, \tag{4.6}$$

where $\boldsymbol{J}_\theta = [\boldsymbol{J}_1, \boldsymbol{J}_2, \boldsymbol{J}_5]$. For the PRBM the virtual spring torques $\boldsymbol{\tau}_\delta$ are:

$$\boldsymbol{\tau}_\delta = -\boldsymbol{K} \cdot \boldsymbol{\delta}, \tag{4.7}$$

where $\boldsymbol{K}$ is the virtual joint stiffness matrix. The virtual springs have all the same stiffness $k = k_1 = k_2 = k_3 = k_4$, as the system is assumed to be orthotropic and the link to have same geometrical properties. Therefore, the virtual spring torques are:

$$\boldsymbol{\tau}_\delta = -k \cdot \boldsymbol{\delta}. \tag{4.8}$$

A recursive algorithm is developed, as illustrated in Fig. 4.1. It needs as input the motor torques $\boldsymbol{\tau}_\theta$ and positions $\boldsymbol{\theta}$ and the virtual spring stiffness k_i, and it estimates the external load $\boldsymbol{\gamma}_e$, the joint variable related to the link deformations $\boldsymbol{\delta}$ and relative torques $\boldsymbol{\tau}_\delta$.

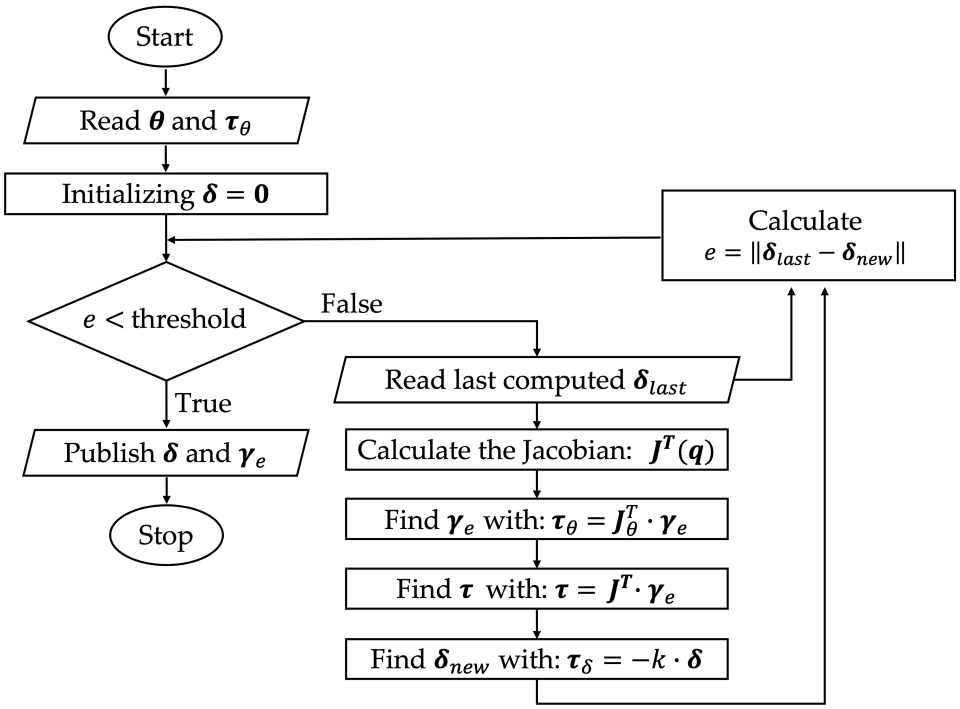

Fig. 4.1 Load and Pose Estimation Algorithm.

4.1.2 Elastostatic Inverse Kinematics

In the previous subsection, an algorithm to evaluate the deformations of the flexible structure and the forces acting on the EE, knowing only the value of motor torques and positions, is proposed. Assuming the same hypotheses, the problem of positioning the EE from the starting point $\boldsymbol{x}_{Start}$ to an end point $\boldsymbol{x}_d$, with certain speed $\boldsymbol{v}_d$, is approached. In this case, the external load $\boldsymbol{\gamma}_e$ is considered known and constant.

Fig. 4.2 shows how the algorithm works. It can be divided in two main parts: first, the motor joint variables $\boldsymbol{\theta}$ are calculated to be used for the motor control; then, the virtual spring joint variables $\boldsymbol{\delta}$ are estimated, given the external load $\boldsymbol{\gamma}_e$ and the virtual spring stiffness matrix $\boldsymbol{K}$, though a recurrent algorithm, based on the same elastostatic approach previously described.

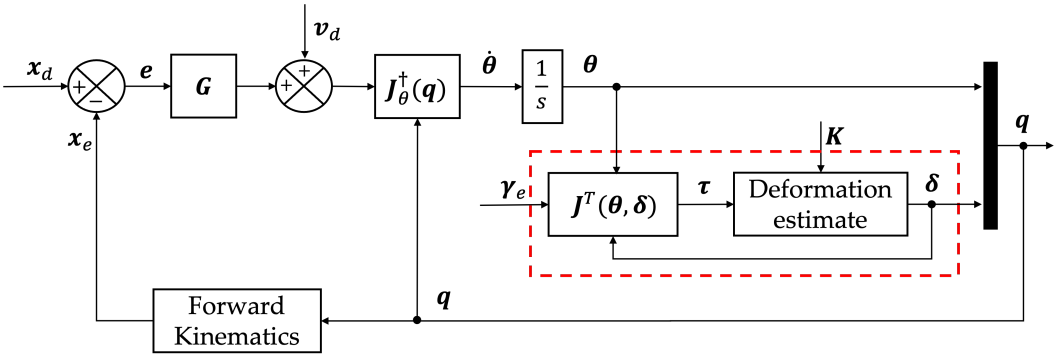

Fig. 4.2 Recursive algorithm for inverse kinematics and state estimation using an elastostatic approach.

Once the deformations $\boldsymbol{\delta}$ are estimated, the vector of all the joint variables $\boldsymbol{q}$ is built to perform the forward kinematics and calculate the expected EE position $\boldsymbol{x}_e$, to be compared with its set value $\boldsymbol{x}_d$. The error $\boldsymbol{e}$ can be calculated and multiplied by the symmetric positive definite matrix $\boldsymbol{G}$, that can be tuned to enhance the performance.

Having defined the right pseudo-inverse of the Jacobian matrix:

$$\boldsymbol{J}^\dagger = \boldsymbol{J}^T(\boldsymbol{J}\cdot\boldsymbol{J}^T)^{-1}, \tag{4.9}$$

the joint velocity variables can be calculated with:

$$\dot{\boldsymbol{\theta}} = \boldsymbol{J}_\theta^\dagger \cdot (\boldsymbol{v}_d + \boldsymbol{G}\cdot\boldsymbol{e}), \tag{4.10}$$

where $\boldsymbol{J}_{\theta}^{\dagger}$ is a $[3 \times 6]$ dimension matrix composed by the 3 motor-associated rows of $\boldsymbol{J}^{\dagger}$. Finally, throughout numerical integration, the inverse kinematics is completed by calculating the motor joint variable $\boldsymbol{\theta}$. Therefore, this algorithm allows the robot to reach a point in the workspace by calculating the deformation of the inflatable links and consequently considering them to modify the set rotations of the actuated joints.

In Fig. 4.3 the configurations of the inflatable robot during a movement of the EE from a starting point $\boldsymbol{x}_{Start}$ to an end point $\boldsymbol{x}_d$, following a planned trajectory, using the elastostatic inverse kinematics algorithm, are shown. The simulation considers the average of experimental stiffness values $\bar{k} = 173$ Nm/rad of Link v1 tests. An external load of $\boldsymbol{f}_e = [0, 10, -15]^T$ N is applied.

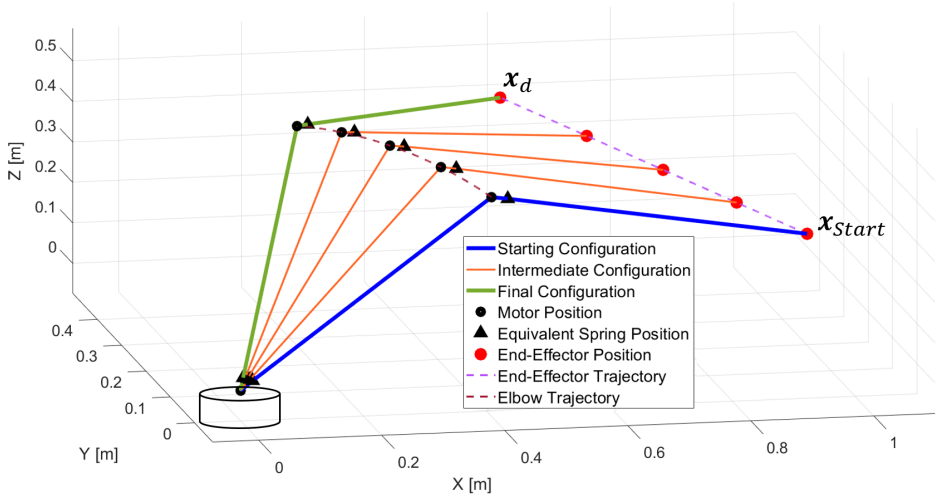

Fig. 4.3 Results of elastostatic inverse kinematics algorithm.

The robot model effectively follows the planned trajectory, setting the rotations of the motor joints to compensate the deformations of the inflatable links. This aspect is underlined in Fig. 4.4, where the values of motor joints angles computed by the elastostatic algorithm are compared with those defined by a rigid body inverse kinematic algorithm. Note that this algorithm does not manage kinematics singularities: the problem can be resolved using the so-called damped least-squares inverse of the Jacobian matrix, as discussed in [102].

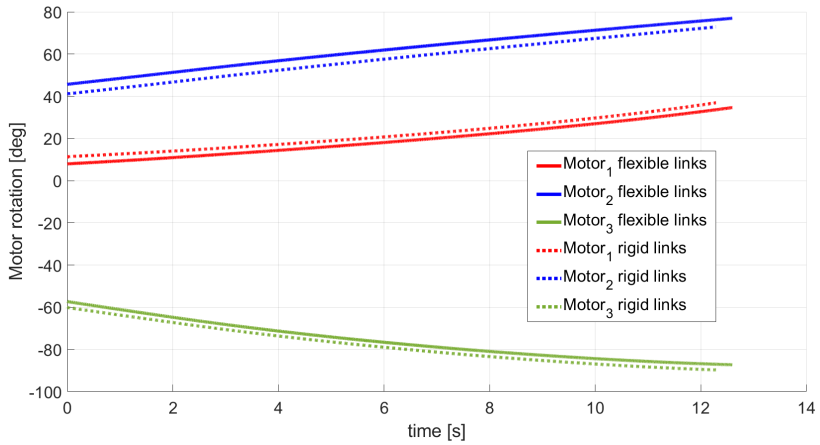

Fig. 4.4 Motor joint variable set in the case of robot with flexible and rigid links.

4.2 Prototype Simulation with Visual Servoing

A PRBM has been developed in Simscape Multibody™, aiming at testing the controls. A task, consisting in a target reaching, has been defined to underline main issues for the POPUP robot control. The target position $\boldsymbol{x}_d$ has been chosen to move the robot toward a more extended configuration, highlighting deflections due to the gravity. The robot control consists in a differential kinematics approach based on the Jacobian matrix $\boldsymbol{J}(\boldsymbol{q})$ of the rigid body model, with 3 DOFs, that relates joint and EE velocities. A trapezoidal velocity profile for EE can be obtained writing the desired velocity $\boldsymbol{v}_d(t)$ as:

$$\boldsymbol{v}_d(t) = min\left(a_0 t, v_0, \sqrt{2a_0\|\boldsymbol{d}(t)\|}\right)\frac{\boldsymbol{d}(t)}{\|\boldsymbol{d}(t)\|}, \tag{4.11}$$

where $\boldsymbol{d}(t) = \boldsymbol{x}_d - \boldsymbol{x}_e$ is the relative distance between target position $\boldsymbol{x}_d$ and EE position $\boldsymbol{x}_e$, a_0 is the maximal initial acceleration and v_0 is the maximal velocity. This law of motion produces a rectilinear path from the EE initial position to the target position. This approach can be easily extended and applied in different tasks, as following of a target in movement, e.g., space debris grasping. In Fig. 4.5 a scheme of the simulated tasks is shown: the robot, represented in the starting configuration $\boldsymbol{q}_0 = [0, 60, -120]^T$ deg, has to reach the desired EE position, that is $\boldsymbol{x}_d = \boldsymbol{x}_A = [-800, 800, 400]^T$ mm in base frame in the specific case. Yellow and green spheres highlight EE position $\boldsymbol{x}_e$ and target position $\boldsymbol{x}_d$ respectively. Two targets

have been considered to perform simulations: target A $\boldsymbol{x}_A = [-800, 800, 400]^T$ and target B $\boldsymbol{x}_B = [-800, 800, 1000]^T$. The starting configuration of all simulations is $\boldsymbol{q}_0$.

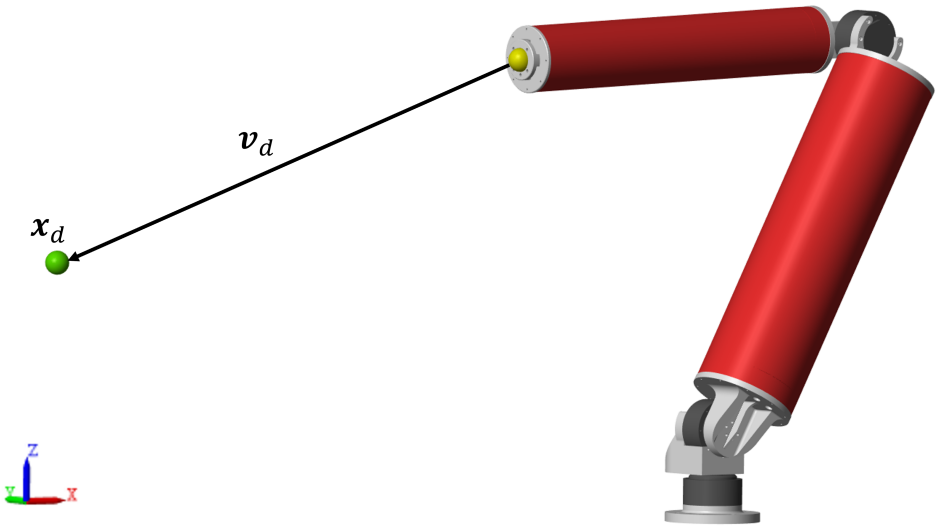

Fig. 4.5 Scheme of the simulated task with robot in the starting configuration and target A.

The following parameters have been set: mass of 2 kg on the EE, internal pressure $p = 60$ kPa, maximal velocity $v_0 = 0.1$ m/s and maximal acceleration of $a_0 = 0.05$ m/s^2.

First simulations aims to underline differences in EE positioning between the flexible link robot and an equivalent rigid link robot, having same joint state. The virtual robot with flexible links has been controlled as a traditional rigid link robot, as shown in Fig. 4.6.

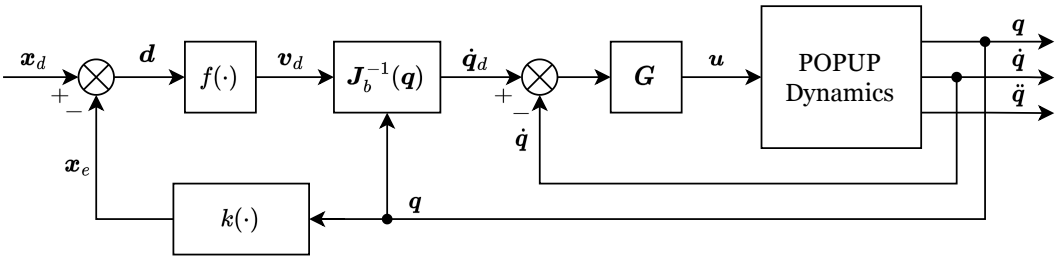

Fig. 4.6 Block scheme of the control using RBM.

EE position $\boldsymbol{x}_e$ is calculated by direct kinematics $k(\cdot)$ of RBM and expressed in base frame, function $f(\cdot)$ represents Eq. (4.11), $\boldsymbol{J}_b(\boldsymbol{q})$ is the Jacobian matrix of RBM

in base frame, $\dot{\boldsymbol{q}}_d$ is the desired joint velocity, $\boldsymbol{G}$ is the matrix gain, $\boldsymbol{u}$ is the reference input for POPUP system consisting in actuator, driver, and multi-body model, $\boldsymbol{q}$, $\dot{\boldsymbol{q}}$ and $\ddot{\boldsymbol{q}}$ are the motor joint position, velocity and acceleration respectively.

Results are shown in Fig. 4.7 and Fig. 4.8, where paths of RBM and PRBM are compared, reaching target A and B, respectively. Since the control algorithm uses RBM direct kinematics to calculate the EE position $\boldsymbol{x}_e$, the equivalent robot with rigid link reaches correctly the targets. Using PRBM, the path is influenced by link deformations, as expected.

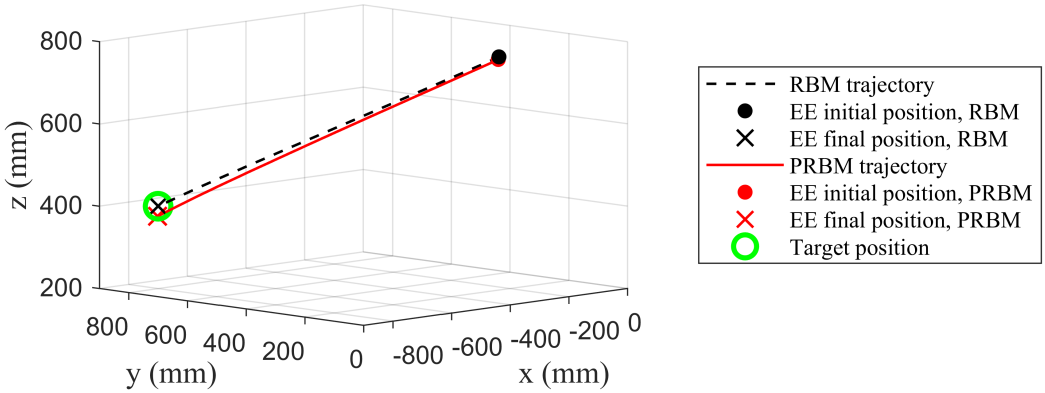

Fig. 4.7 Path of PRBM compared to RBM reaching the target A using RBM-based control.

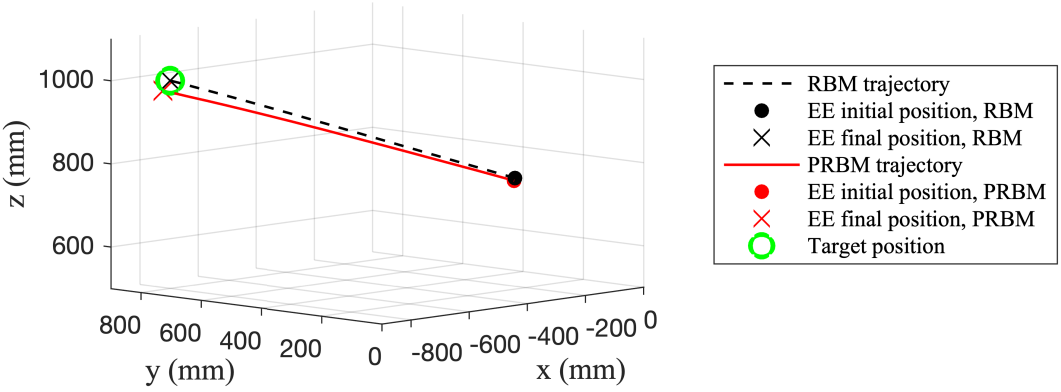

Fig. 4.8 Path of PRBM compared to RBM reaching the target B using RBM-based control.

In Fig. 4.9 the absolute difference of EE position between RBM and PRBM during the two simulated tasks is shown.

The PRBM shows an error that depends on the configuration and payload, due to gravity that bends the links. A difference of 6.6 mm for the EE position is exhibited

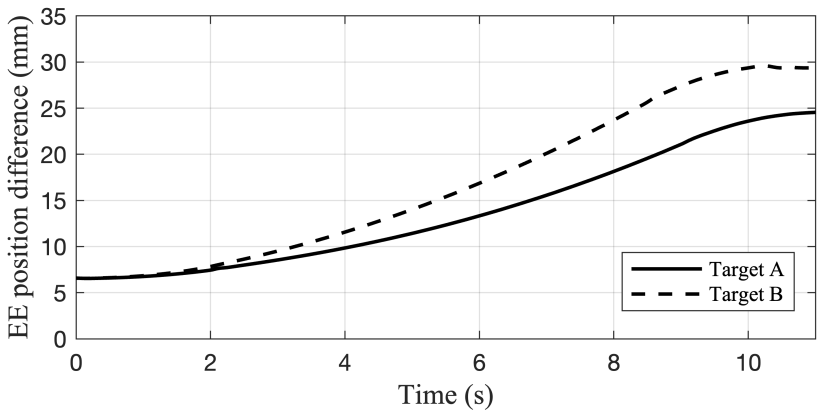

Fig. 4.9 EE position difference of PRBM with respect to RBM during the tasks reaching target A and target B.

in the starting configuration, corresponding to joint variables $\boldsymbol{q}_0$. The difference grows during the task up to 24.4 mm when target A is reached and up to 29.6 mm when target B is reached, as the final robot configuration is more extended for both scenarios, intensifying the deflections caused by payload. The positioning error can be reduced with different strategies, as estimating the EE position with PRBM recurring to link sensor data. However this estimate depends on sensor accuracy, data fusion technique and simplification due to the adopted model.

Last simulations aims to validate a control strategy based on visual servoing (VS), with a camera mounted on the EE of the virtual robot with flexible link. Block scheme of robot control is shown in Fig. 4.10.

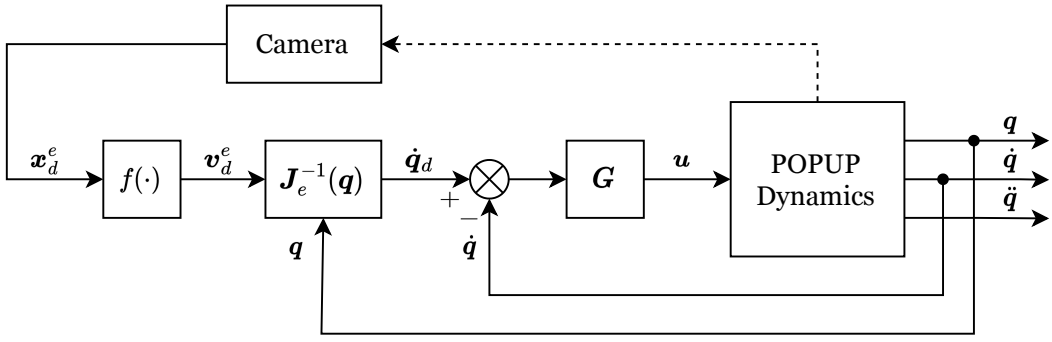

Fig. 4.10 Block scheme of the control using VS with camera mounted on EE.

Using computer vision algorithms, the camera can identify the target position in EE frame $\boldsymbol{x}_d^e$. Then, the desired velocity in EE frame $\boldsymbol{v}_d^e$ is calculated by Eq. (4.11), known $\boldsymbol{x}_e^e = \boldsymbol{0}$. Finally, using Jacobian matrix of RBM in EE frame $\boldsymbol{J}_e(\boldsymbol{q})$, the desired

joint velocity $\dot{\boldsymbol{q}}_d$ is calculated. Simulation provides exact feedback for target position $\boldsymbol{x}_d^e$, validating the control algorithm independently from vision system errors.

Results are shown in Fig. 4.11 and Fig. 4.12, for target A and target B reaching, respectively. The robot with flexible links using PRBM, on which camera is virtually positioned, correctly reaches the targets, demonstrating how this strategy is able to compensate link deflections minimizing the positioning error between target and EE. Paths calculated using PRBM and RBM with same joint state are plotted, underlining the difference in positioning between the virtual robot with flexible links and an equivalent robot with rigid links. With reference to Figure 2.18, since Jacobian matrix of RBM is used, EE_{RBM} frame is evaluated as actual EE frame. On the other hand, measured target position $\boldsymbol{x}_d^e$ is referred to EE_{PRBM} frame. Nonetheless, the control algorithm effectively compensates errors due to small deflections.

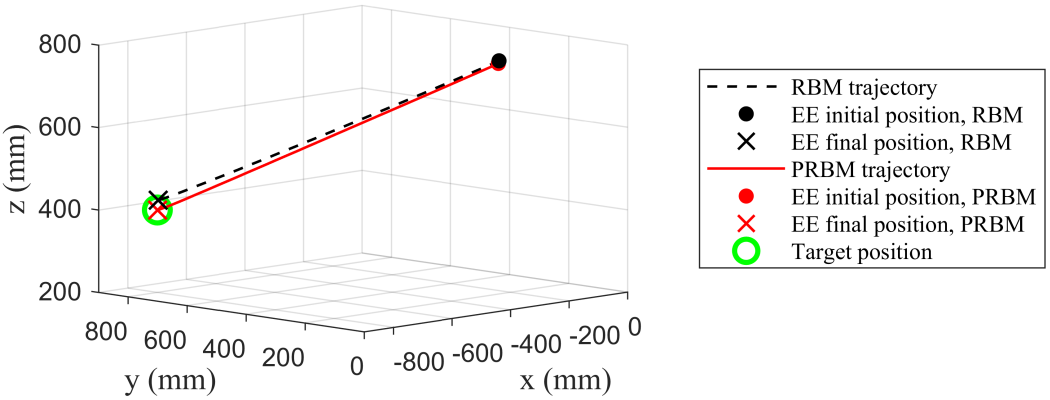

Fig. 4.11 Path of PRBM compared to RBM reaching the target A using PRBM-based control.

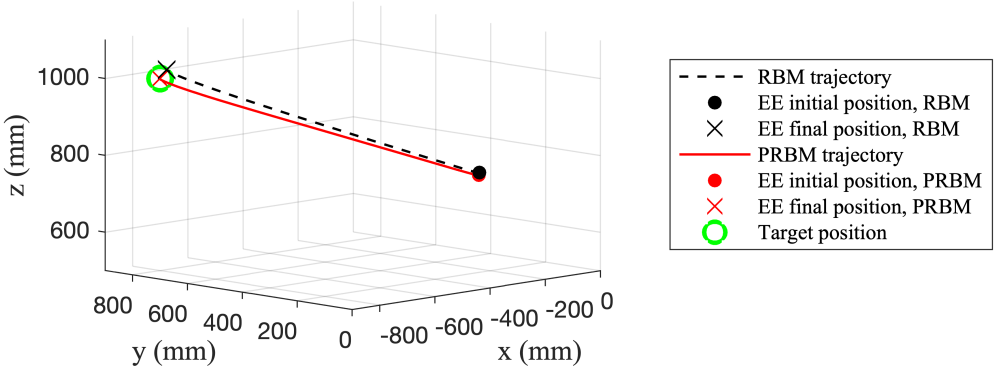

Fig. 4.12 Path of PRBM compared to RBM reaching the target B using PRBM-based control.

In Fig. 4.13 and Fig. 4.14 motor joint position values $\boldsymbol{\theta}$ are shown during the tasks reaching target A and target B, respectively, highlighting corrections provided by the camera-based algorithm with respect to a traditional robot control in order to precisely reach the targets.

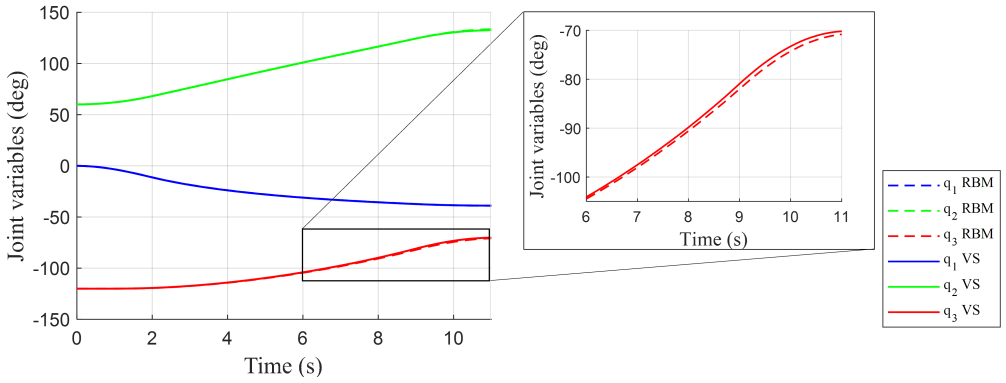

Fig. 4.13 Motor joint position during the simulations with RBM-based and VS control for target A reaching.

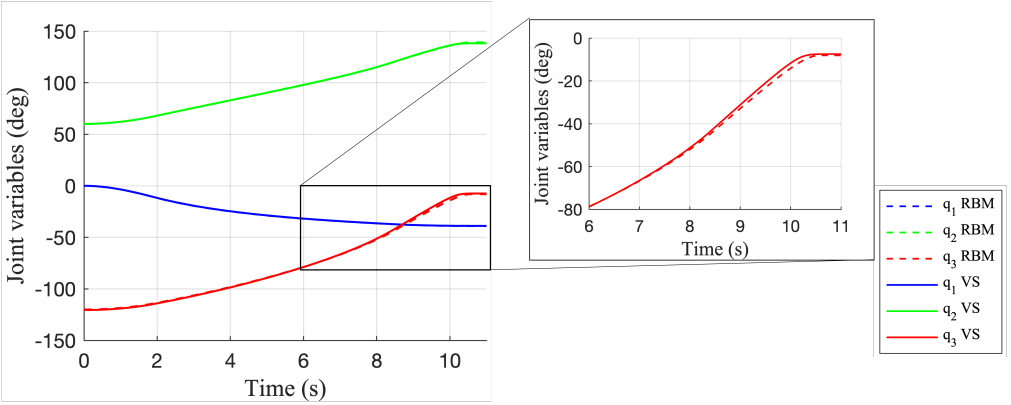

Fig. 4.14 Motor joint position during the simulations with RBM-based and VS control for target B reaching.

Results demonstrate the effectiveness of the presented control strategy based on visual servoing. Moreover, the algorithm potentially allows us to follow a target in movement. Since the desired position is correctly reached in the simulated environment providing exact feedback, the accuracy in positioning of the inflatable robot depends on computer vision algorithms that have to be developed.

4.3 Space Application

4.3.1 Visual Servoing in Space Robotics

To perform OOS missions and debris removal operation, a robot must approach targets. Therefore, a space robot needs a visual system that can recognize and measure the relative pose between the robot EE and the target in real time. Visual perception technologies can be categorized as cooperative or non-cooperative based on the characteristics of the targets [103, 104]. Cooperative technologies relies in visual markers, have been successfully used in many space robots, e.g., for SSRMS. However, most of the actual OOS missions for faulty satellites involve targets without artificial markers. Therefore, non-cooperative visual perception is required but more difficult due to the unknown target characteristics. The typical features of a non-cooperative target can be the satellite adapter ring, the solar panel boom, and the satellite nozzle [104].

The vision system can be mounted on the end-effector (eye-in-hand configuration) and/or on the base satellite (eye-to-hand configuration). For eye-in-hand visual perception system, the camera can be placed closer to the target by moving the position of the EE, which enhances the target measurement accuracy. However, the motion can cause image blurring, and the risk of losing the target from the field of view (FOV). The eye-to-hand configuration puts the sensor in the robot working area, which allows global monitoring but reduces accuracy and might be occluded by robot motion [103].

The eye-to-hand camera can be a mobile camera if attached to actuators [105]. The controller generates commands for the manipulator based on the camera system feedback. The controller can also take into account the dynamics of the free-floating system, such as the coupling between the manipulator and the base, and the orbital perturbations. One possible approach is to use an optimal control method that minimizes a cost function that includes the image error, the motor commands and the attitude disturbances. Another possible approach is to use a finite-state machine logic that switches between different strategies, such as commanding only linear or angular velocity of the camera, depending on the situation [106, 107].

In the specific case of debris removal operations, a visual guidance and navigation system can autonomously identify the non-cooperative target debris and realize a

controlled rendezvous maneuver with it using visual features extracted from the images. One of the challenges of visual servoing for debris mitigation is to cope with the uncertainties and variations of the target debris, such as its shape, size, motion and reflectivity. To address these challenges, some researchers have proposed using learning-based methods to enhance the robustness and adaptability of visual servoing systems. For example, a deep convolutional neural network (CNN) model can be used to detect and estimate the pose of objects in 3D space using an effective deep-CNN model architecture [108, 109]. An example of debris pose estimation [110] is shown in Fig. 4.15.

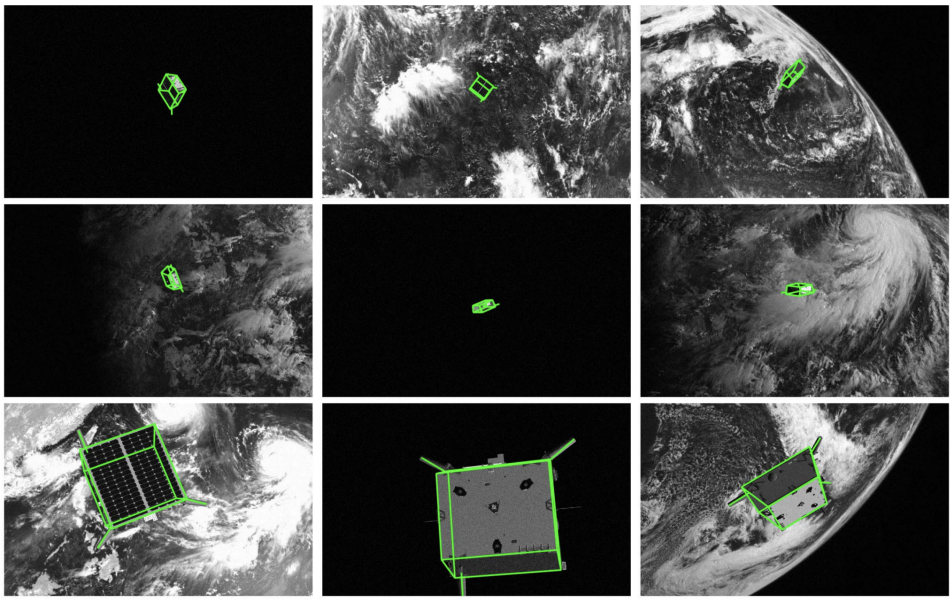

Fig. 4.15 A montage of random test images with the predicted poses shown as green wireframes.

Another challenge regards possible occlusions of key features of the target used by vision system: the target motion can cause some features to become visible or invisible. However, the target motion can also be used to estimate the position of the occluded features by using predictive algorithms, as proposed in [111].

4.3.2 Simulation of a debris removal task

The vision-based control strategy presented in Section 4.2 is applied to Active Debris Removal (ADR). A new architecture of POPUP, suitable for this specific task, has been developed. It has 7 DOFs: three axes for the shoulder, one axis for the elbow and three axes for the wrist. The DOF redundancy enables solving optimization problems or perform additional tasks, such as minimizing velocity norms or reducing forces exchanged with spacecraft. The arm is equipped with a gripper at the end-effector to manipulate objects. The two links have same characteristics, with length $L = 4$ m and radius $r = 85$ mm. The inner pressure is set to $p = 50$ kPa, which gives a wrinkling moment $M_w = 39$ Nm using Eq. (2.5) by Wielsgosz. Setting the maximum EE acceleration $a_0 = 0.001$ m/s^2, the maximum payload the links could sustain is 4500 kg, assuming a fully extended robot configuration.

The dynamic physical model of the robot, mounted on a free-floating chaser spacecraft, is developed using Simscape Multibody™. The robot task is to reach and grasp a handle on a space debris, which is modeled as a cube to preserve position and orientation information. The Hertzian contact between the gripper fingers and the handle is considered. The render of the simulated environment is shown in Fig. 4.16, including the chaser spacecraft, the POPUP and debris with the handle to grasp.

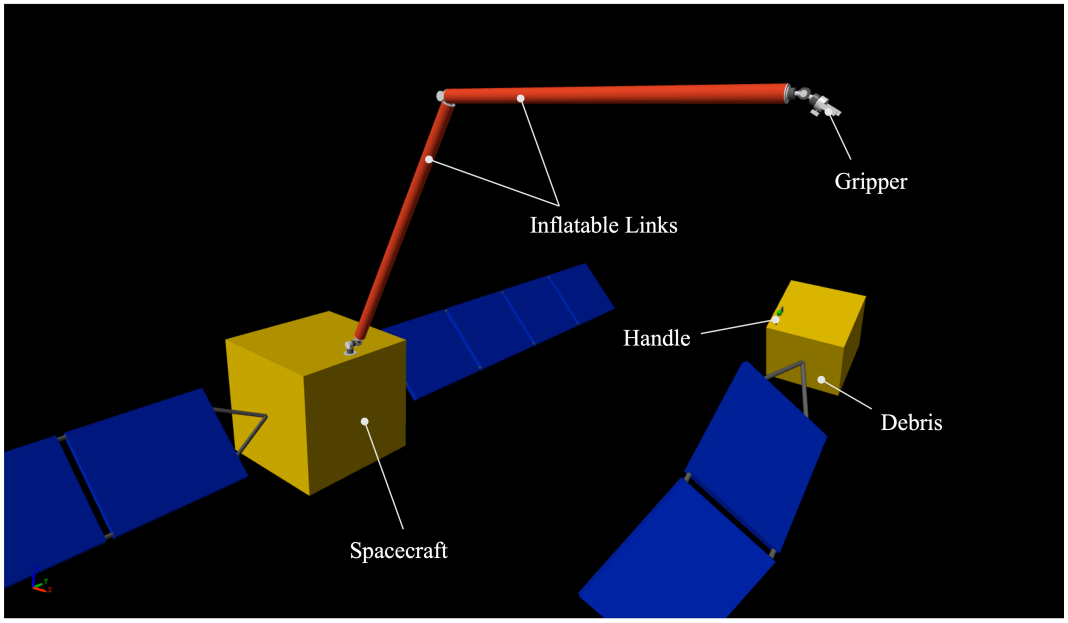

Fig. 4.16 POPUP robot concept.

In this work, the rigid body model (RBM), which treats the inflatable links as rigid elements, and the flexible body model (FBM), which accounts for the link deformations using finite elements, have been considered. The RBM and FBM schemes for the specific configuration of the inflatable robot are illustrated in Fig 4.17.

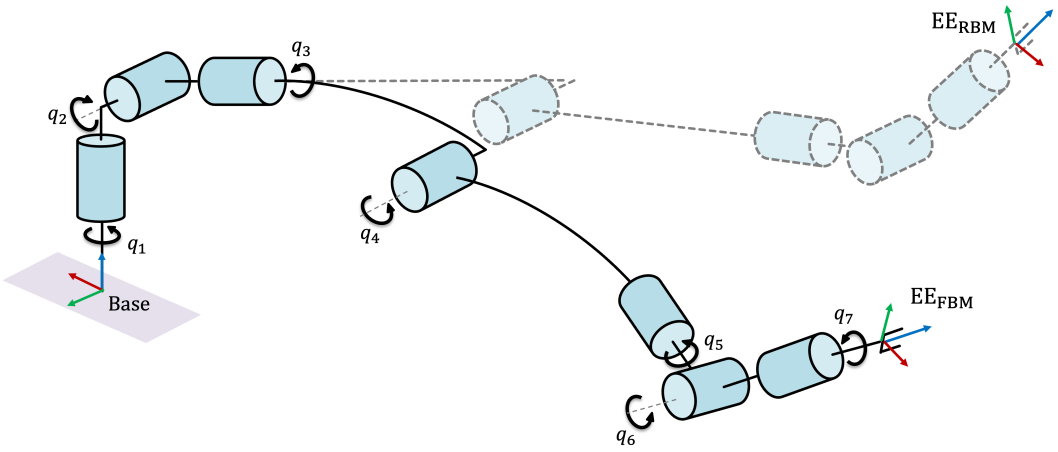

Fig. 4.17 Robot kinematics, Base and EE frames using RBM and FBM.

The physical model of the robot developed in Simscape Multibody™ is a FBM that can include possible small misalignments due to the inflation process or hysteresis effects. These errors could compromise the kinematic chain representation, resulting in the loss of the correspondence between the robot base and the EE.

When an inflatable link is subjected to a bending load under the wrinkling condition, its behavior is linear and can be modeled as a flexible beam following the Euler-Bernoulli theory. The links are assumed to be slender, homogeneous, isotropic, and made of linearly elastic material. A trade-off between simulation accuracy and speed is achieved by using 10 finite elements per link. If the load produces high deformations that are incompatible with the linearity region imposed by the wrinkling moment condition, an alarm is triggered by the model indicating that the analysis is not feasible. In general, the robot must operate within the linearity area, far from the wrinkling condition. The design process must determine the appropriate pressure level and size of the robot for the space mission.

Vectran™ is considered as the material providing structural mechanical resistance in the following simulations. Its elastic modulus is assumed $E = 75$ GPa [60] and its thickness is assumed to be 2 mm. For inflatable beams, the equivalent elastic

modulus E_p is estimated from Eq. (2.18). Since $E \gg pA/S$, it results $E_p \sim E$. Therefore, if a high stiffness material is used for link manufacturing with a low-pressure level, the stiffness of the beam does not significantly depend on pressure in non-wrinkling conditions. The stiffness matrix $\boldsymbol{K}$ is defined using elastic modulus and geometrical element properties. A proportional damping matrix $\boldsymbol{D}$ is set as $\boldsymbol{D} = \beta \boldsymbol{K}$, with $\beta = 0.05$ s.

The debris capture procedure consists of four phases, as illustrated in Fig. 4.18. The first phase is the approach operation, where the chaser executes a rendezvous manoeuvre to align its position with the target within the manipulator workspace. The second phase is the inflation and deployment of the manipulator, which is controlled by a joint position control that regulates the desired initial configuration $\boldsymbol{q}_0$. The third phase is the target following, which is accomplished by the robot using algorithms, based on visual servoing, that are detailed in the following. Finally, when the target pose is reached by the EE, the handle of the debris is grasped by the gripper of the manipulator.

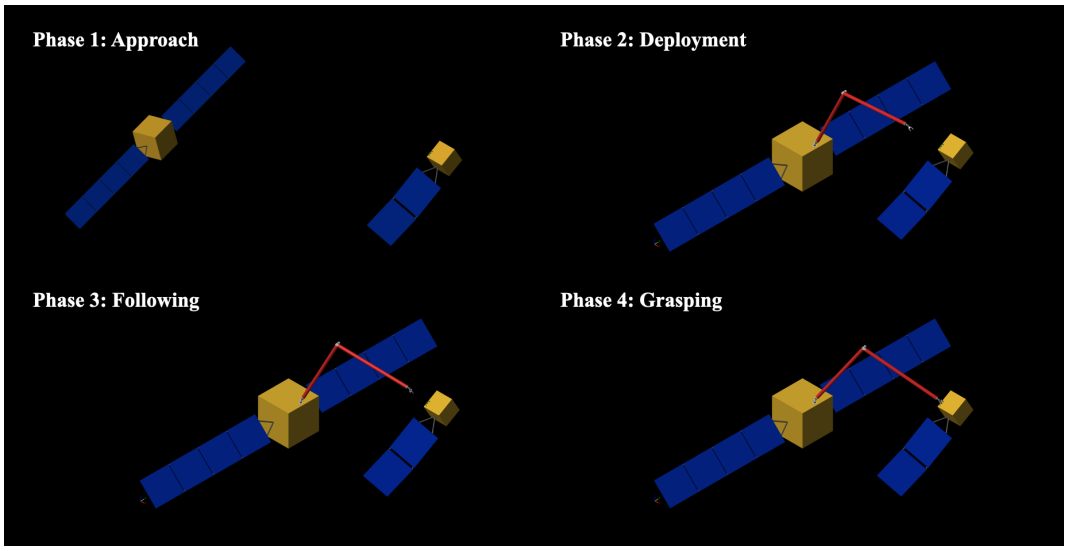

Fig. 4.18 Debris capture phases: approach, deployment, following and grasping.

This work focuses on the capture operation performed by the inflatable robot, assuming that the deployment phase has been completed and the initial configuration $\boldsymbol{q}_0$ has been reached. Grasping strategies for the inflatable robot are more challenging than those for conventional robots, due to the link flexibility and the kinematics uncertainty inherent to the system due to the inflation procedure. The capture strategy

relies on visual servoing using two camera systems. The first system is attached to the chaser, where the arm is installed, and enables the detection of the target relative to the robot base frame. The second system is located on the EE flange and provides the position of the target relative to the gripper.

The effects of environmental forces, such as gravity gradient and solar radiation pressure, and relative orbital dynamics are neglected. This assumption is valid due to the short duration of the maneuver and close proximity between the two vehicles [112]. The target is steady during the simulation.

The spacecraft and the robot are treated as separate systems for control purpose, and the forces exerted by the robot are considered as a disturbance to the spacecraft and vice versa. The spacecraft needs to be maintained in a steady state for all the following and capture phase. Therefore, a simple proportional-integral-derivative (PID) controller with pose and velocity loops is implemented, employing the target pose identified by the base camera system as reference frame for spacecraft pose and attitude control. The response dynamic of the thrusters is approximated as a first order transfer function with $\tau_s = 50$ ms, consistent with typical values [113].

The robot control algorithm, schematized in Fig. 4.19, employs the RBM to compute the direct kinematics $k(\cdot)$ and the Jacobian matrix $\boldsymbol{J}$ while the robot dynamics is modeled according to the FBM in Simscape Multibody$^{\text{TM}}$.

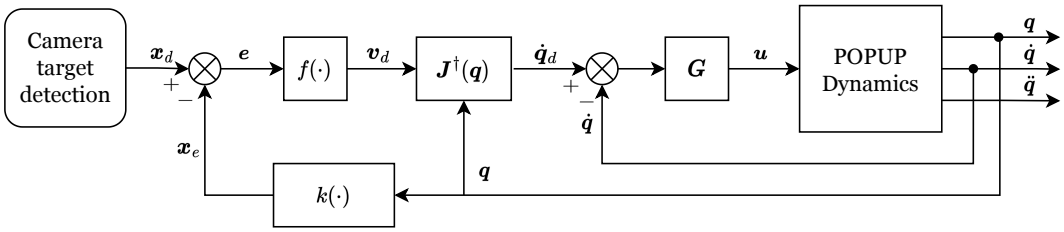

Fig. 4.19 Scheme of the control with differential kinematics and visual servoing.

The desired EE pose, denoted by $\boldsymbol{x}_d = [\boldsymbol{p}_d^T, \boldsymbol{\phi}_d^T]^T$, consisting of position $\boldsymbol{p}_d$ and orientation $\boldsymbol{\phi}_d$, is assumed to be always available with respect to the robot base frame, as it is needed for the chaser spacecraft position and attitude control.

The algorithm continuously monitors whether the target is detected by the EE camera. The camera detection criterion is simulated using the pinhole camera model, which projects a generic point in space with coordinates $\boldsymbol{p} = [X, Y, Z]^T$, expressed in camera frame, onto the camera sensor plane $\boldsymbol{p}' = [fX/Z, fY/Z, f]^T$, where f is the

focal length and the camera z-axis is orthogonal to the sensor. If the projection falls within the sensor area, the point is considered visible to the camera. The position and orientation problems are solved separately. The position error is defined as:

$$\boldsymbol{e}_P = \Delta\boldsymbol{p} = \boldsymbol{p}_d - \boldsymbol{p}_e, \tag{4.12}$$

where $\boldsymbol{p}_d$ is the desired position and $\boldsymbol{p}_e$ the EE position. These subscripts are used consistently throughout the dissertation. The desired linear velocity for the EE, which follows a trapezoidal profile, is computed as:

$$\dot{\boldsymbol{p}}_d = \min(a_0 t, v_0, \sqrt{2a_0\|\Delta\boldsymbol{p}\|})\frac{\Delta\boldsymbol{p}}{\|\Delta\boldsymbol{p}\|}, \tag{4.13}$$

where $a_0 = 0.001$ m/s^2 and $v_0 = 0.01$ m/s are the maximum linear acceleration and velocity, respectively. The orientation error $\boldsymbol{e}_0$ is calculated exploiting quaternion in the form $Q = (\eta, \boldsymbol{\varepsilon})$:

$$\boldsymbol{e}_0 = \Delta\boldsymbol{\varepsilon} = \eta_e(\boldsymbol{q})\boldsymbol{\varepsilon}_d - \eta_d\boldsymbol{\varepsilon}_e(\boldsymbol{q}) - \boldsymbol{S}(\boldsymbol{\varepsilon}_d)\boldsymbol{\varepsilon}_e(\boldsymbol{q}), \tag{4.14}$$

where $\boldsymbol{S}(\cdot)$ is the skew-symmetric operator. As before, the angular desired velocity:

$$\dot{\boldsymbol{\phi}}_d = \min(\alpha_0 t, \omega_0, \sqrt{2\alpha_0\|\Delta\boldsymbol{\varepsilon}\|})\frac{\Delta\boldsymbol{\varepsilon}}{\|\Delta\boldsymbol{\varepsilon}\|}, \tag{4.15}$$

where $\alpha_0 = 0.001$ rad/s^2 and $\omega_0 = 0.01$ rad/s are the maximum angular acceleration and velocity, respectively. The desired velocity $\boldsymbol{v}_d = [\dot{\boldsymbol{p}}_d^T, \dot{\boldsymbol{\phi}}_d^T]^T$ is calculated from the error $\boldsymbol{e} = [\boldsymbol{e}_P^T, \boldsymbol{e}_0^T]^T$. By performing differential inverse kinematics, the desired joint velocity is calculated as:

$$\dot{\boldsymbol{q}}_d = \boldsymbol{J}^{\dagger}(\boldsymbol{q})\boldsymbol{v}_d, \tag{4.16}$$

where the matrix

$$\boldsymbol{J}^{\dagger} = \boldsymbol{J}^T(\boldsymbol{J}\cdot\boldsymbol{J}^T)^{-1}, \tag{4.17}$$

is the right pseudo-inverse of $\boldsymbol{J}$. This expression aims to use the redundancy of the manipulator to locally minimize the norm of joint velocities [102]. When the target is not detected by EE camera, the Jacobian in EE frame $\boldsymbol{J}_b$ is used. The control loop is closed using $\boldsymbol{x}_e = [\boldsymbol{p}_e^T, \boldsymbol{\phi}_e^T]^T$, calculated by the direct kinematics $k(\cdot)$ of the RBM. If the target is detected by EE camera, a control switch occurs. The target

position is expressed in the EE frame from EE camera frame. In this case $k(\cdot)$ is a rigid transform that does not depend on robot model and status. This information is used to close the loop directly, avoiding errors due to direct kinematics from base to EE. The Jacobian in EE frame is calculated as:

$$\boldsymbol{J}_e = \begin{bmatrix} \boldsymbol{R}^e & \boldsymbol{O} \\ \boldsymbol{O} & \boldsymbol{R}^e \end{bmatrix} \boldsymbol{J}_b, \tag{4.18}$$

where $\boldsymbol{R}^e$ is the rotation matrix from base to EE frame using the RBM. When the target handle is reached, the gripper grasps it using a force control scheme.

Two simulation scenarios are considered. In both scenarios the spacecraft pose exhibits little variation during the robot motion due to the low speeds and accelerations of the robot. Results are shown using the base frame of the robot at the initial condition as reference frame. The first scenario involves the camera switch control applied to POPUP with a FBM without misalignments in the robot structure. In Fig. 4.20 the path of the EE is shown, indicating the type of control used. Fig. 4.21 shows the link angular deflections along two orthogonal rotation axes and the joint velocities during the control switch.

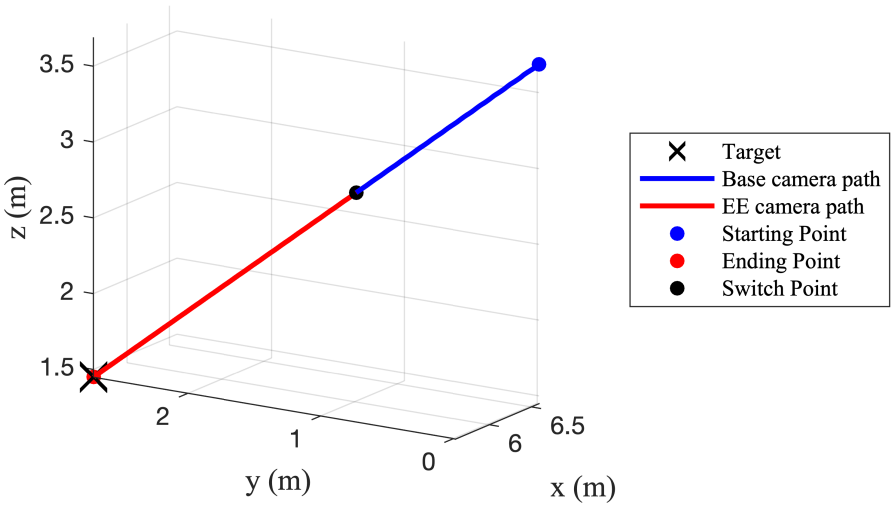

Fig. 4.20 Robot without defects, EE path.

The vertical grey line indicates the instant when the control switch occurs. Deflections are negligible since accelerations on the links are moderate. The switch does not imply significant change in the EE desired velocity, then EE acceleration is

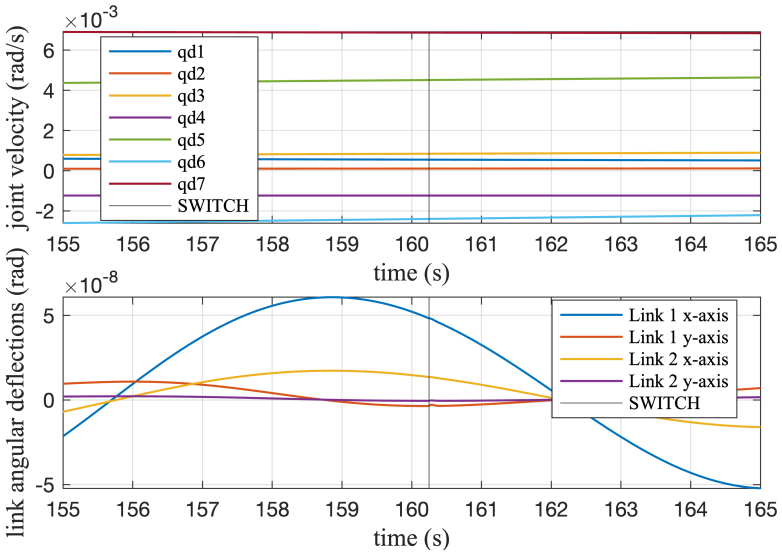

Fig. 4.21 Robot without defects, joint velocities and link angular deflections during control switch.

null. Therefore, joint velocities are always continuous, even during the transition between the two control modes.

The second scenario is simulated with an angular error of 4 deg between the joint 3 and the first inflatable link. Fig. 4.22 illustrates the path of the robot EE.

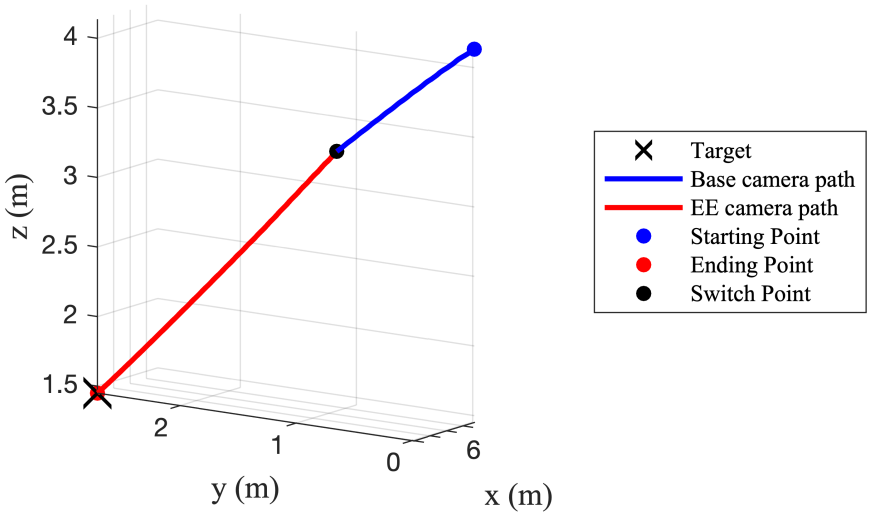

Fig. 4.22 Robot with defects, EE path.

When the switch is enabled, the robot control effectively compensates for the errors and reaches the target. The path exhibits a discontinuity when the switch occurs, which leads to joint velocity discontinuities, and consequently accelerations that induce link deflections, as shown in Fig. 4.23. These defections are moderate due to the low robot speed.

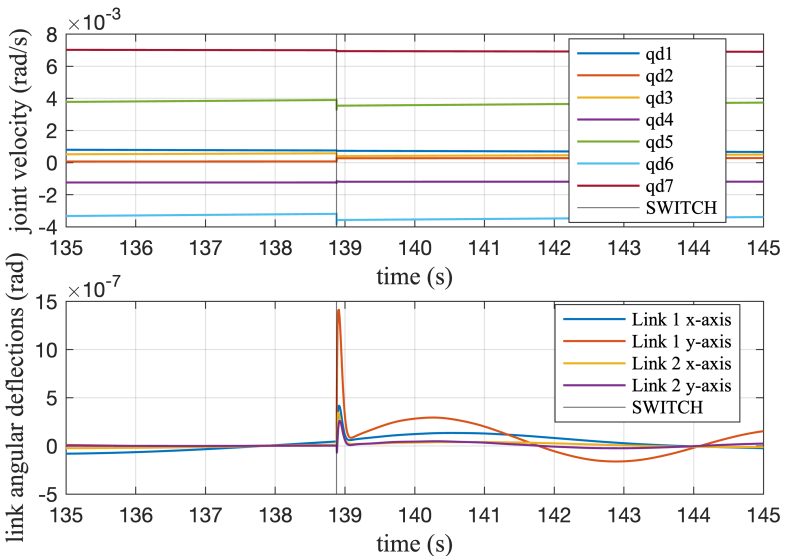

Fig. 4.23 Robot with defects, joint velocities and link angular deflections during control switch.

Despite the Jacobian is computed based on the EE frame using the RBM, the errors due to link deflections, misalignments, and defects can be effectively compensated by having a camera mounted on the EE, since it provides the accurate value for the error. Further works expect to implement a smoother transition between the two control signals to avoid the discontinuity generated by the switch.

Chapter 5

Discussion and Conclusions

In this work, a novel space robotic manipulator with inflatable links has been proposed. This solution combines the simple control of traditional manipulator with the advantages of inflatable structures. The robot can be stored in compact form and deployed when required. When the task is completed it can be withdrawn and stored again in a limited volume. The inflatable links are lightweight and they are expected to be made with high elastic modulus material in order to improve dynamic performance of the robot in terms of deflections. Moreover, the selected candidate structural materials show protection against micro-meteorites impact and provide great vibration damping properties.

The growing demand for space activities motivates the development of new systems to reduce costs: this system is cost effective for the launch due to its lightness and low stowed volume. The inflatable manipulator is a versatile system that can be used for various space domains. It can be used onboard spacecrafts, where it can be stored in a compact form when not needed, and deployed for specific tasks. It can also be used for In-space Service, Assembly and Manufacturing (ISAM) activities, such as repairing and fueling of satellites, assembling of large structures from components, or manufacturing complex infrastructures in orbit. Moreover, it can be used for active debris removal missions.

This work proposes a design framework for the development of the robot. The design objective is to avoid the wrinkling of the inflatable links during the tasks. The robot parameters, such as geometry, payload, maximum acceleration, and internal pressure, are obtained from semi-empirical formulations for inflatable beams based

on membrane theory. This theory enables a simple and conservative calculation of critical values without needing detailed information on the material properties of the link, ideal for a preliminary robot sizing and design. However, for a more accurate validation of the robot performance and behavior, more refined formulations and dynamic models are needed, which take into account the nonlinearities and uncertainties of the inflatable system. When there are no wrinkles, inflatable links can be modeled using conventional linear models for flexible beams, such as the Euler-Bernoulli theory with suitable adjustments for the elastic modulus that account for the internal pressure. However, it is shown that the internal pressure has a negligible effect on the elastic properties when using low operational pressures of 10–100 kPa and high elastic modulus materials with $E = 50$–150 GPa: the equivalent elastic modulus of the inflatable link is essentially the same as the elastic modulus of the layer for the structural mechanical resistance.

The use of high elastic modulus materials is a key feature of the proposed solution, which differs from other inflatable link manipulators that employ low elastic modulus materials and depend on the internal pressure to control the link stiffness. This aspect simplifies the control problem, and makes the inflatable robot more similar to conventional space manipulators that use rigid or flexible links. The high elastic modulus materials provide a high bending stiffness, which is desirable for accurate manipulation tasks. Internal pressure is a parameter used to regulate the achievable load of the robot, as it determines the critical value for the onset of wrinkling. Moreover, the chosen high modulus materials for the structural layer, such as Kevlar™ and Vectran™, already used for the construction of inflatable space habitats, have additional advantages such as resistance to impact from micrometeoroids and orbital debris (MMOD), radiation protection, low/high temperature resistance, vibration damping, creep and abrasion resistance, minimal off- and out-gassing characteristics.

A crucial component of the robotic system is the method and mechanism for the proper deployment and retraction of the links. A possible strategy is presented, but a more advanced mechanism with enhanced features is currently being patented and it is not disclosed in this dissertation.

Different robot modeling approaches are presented based on the previous considerations about the working region of the inflatable link, which defines the range of applicability of the solutions. Essentially, two main models are employed to account

for the link flexibility: a model based on pseudo-rigid bodies, which approximates the link as two rigid segments connected by revolute virtual joints, and a model based on finite elements using Euler-Bernoulli theory, which discretizes the link as a set of beam elements with bending stiffness. Both models are developed using Simscape™ as a software tool, which allows for an easy integration with Simulink® and MATLAB® environments.

The models enable various analyses. In an initial stage, they assist the design of the robot by testing it with different control laws, payloads, and geometries. They can also reproduce the behavior of an existing robot after properly estimating its parameters: the goal is to create a digital twin of the robot. They can simulate space applications that are challenging to test on Earth, such as micro-gravity. Moreover, models allow for the testing of control strategies and algorithms for the subsequent implementation on the real robotic system.

The development of the first inflatable link prototype and the tests for its static and dynamic characterization are described. The tests confirm the validity of the most conservative wrinkling moment formulation based on the membrane theory. The link prototype is made of polymeric material, which is different from the materials required for the final application. However, it provides valuable insights into the feasibility of the project. After building the inflatable links, the robotic system is constructed using additive manufacturing for the rigid joints, and integrating electric motors, pneumatic lines, sensors, and electronic devices needed for the control. The robot prototype has 3 DOFs with two inflatable links, and it can be extended to 6 DOFs with the addition of a spherical wrist. A remote teleoperated control is implemented as a first step towards the integration of advanced control algorithms that can autonomously reach a target in space.

Different control strategies are discussed. A first strategy is based on an elastostatic approach and a virtual joint model: this strategy aims to estimate the link deflections based on known parameters using only the motor position and torques. This approach can be used to complement the better estimation provided by built-in sensors mounted on the inflatable links, which measure the link deformations. However, this method requires iterative procedures and an approximate model, which make it difficult to implement on the real robot. Using the virtual joint model of the robot prototype, a visual servoing control based on kinematic inversion algorithms is tested to evaluate its ability to compensate for the link deformation even with 2 kg

payload on Earth. The control strategy uses two camera systems: one attached to the end-effector of the robot and one located on its base. The results demonstrate that this technique is effective and enables the robot to successfully reach the target, without depending on the link deformation estimation.

Visual servoing is a common technique in the space sector for ISAM activities, as it enables the accurate positioning of spacecrafts, satellites, and conventional manipulators. This work shows its applicability for the control of the inflatable manipulator. A space application for active debris removal is simulated, where the inflatable robot is used as a manipulator to grasp a fixture on the debris. A large inflatable robot with 7 DOFs is modeled using finite elements for the 4-m-long inflatable links. The robot is attached to a free-floating spacecraft. In this simulation, geometrical deviations are introduced to account for possible misalignment or error from the nominal configuration due to the inflation and deployment process. The results demonstrate that the control based on cameras can compensate for the link deflection and possible reasonable link deviations.

In conclusion, this work introduced a novel inflatable and deployable robotic arm for space applications, aiming to provide a cost-effective solution for the expansion of the space sector. A design framework and a material selection are presented, based on the wrinkling criterion and the high elastic modulus requirement. A first robot prototype for on-Earth testing is developed and tested, demonstrating the feasibility and potential of the project. Different modeling techniques are investigated and applied, based on pseudo-rigid bodies and finite elements. The implementation of visual servoing techniques is validated on the inflatable manipulator model, showing that these control methods, which are commonly used on conventional manipulators, can also be effective on the manipulator made of inflatable links.

This work aimed to start the development of the inflatable robotic arm, providing first analyses, design methodologies and control strategies, that need to be further explored and refined for the improvement of the technology readiness level (TRL), which is currently assessed between 3 and 4, since the proof-of-concept was provided and functional verification of all the robot components in laboratory environment is in progress.

The visual servoing control has to be implemented on the robot prototype for performing grasping tasks. A tracking system should monitor the motion of the prototype and compare it with the simulated task using the models developed. The

robot tracking can enable the estimation of the dynamic parameters of the robot, which can be used to improve the models and fit the parameters for creating a digital twin. Inflatable links with appropriate materials for space applications, e.g., Kevlar™, have to be developed and the deployment and retraction process has to be tested and validated. A new test rig for simulating microgravity environment using air bearings is planned to be built. Therefore, a new prototype of the robot with links made of space materials and capable of automatic deployment and retraction is under development. The validation of the inflatable link with tests in relevant environment, such as vacuum and extreme temperature, is required to achieve TRL 6, along with the development of the digital twin. Finally, this work lays the foundation for the establishment of an academic spin-off, that has the inflatable manipulator as its main product.

References

[1] Alina Orlova, Roberto Nogueira, and Paula Chimenti. The Present and Future of the Space Sector: A Business Ecosystem Approach. *Space Policy*, 52, 5 2020.

[2] Norbert Frischauf, Rainer Horn, Tilo Kauerhoff, Manfred Wittig, Ingo Baumann, Erik Pellander, and Otto Koudelka. NewSpace: New Business Models at the Interface of Space and Digital Economy: Chances in an Interconnected World. *New Space*, 6(2):135–146, 2018.

[3] Borna Monazzah Moghaddam and Robin Chhabra. On the guidance, navigation and control of in-orbit space robotic missions: A survey and prospective vision. *Acta Astronautica*, 184:70–100, 2021.

[4] Marcello Romano. Space robotics. In John Baillieul and Tariq Samad, editors, *Encyclopedia of Systems and Control (Second Edition)*, pages 2090–2097. Springer-Verlag London, 2020.

[5] Yang Gao and Steve Chien. Review on space robotics: Toward top-level science through space exploration. *Sci. Robot*, 2:28, 2017.

[6] NASA. In-Space Servicing, Assembly, and Manufacturing (ISAM). nexis.gsfc.nasa.gov/isam [Online; Last Accessed June, 2023].

[7] Angel Flores-Abad, Ou Ma, Khanh Pham, and Steve Ulrich. A review of space robotics technologies for on-orbit servicing. *Progress in Aerospace Sciences*, 68:1–26, 2014.

[8] Joshua P Davis, John P Mayberry, and Jay P Penn. On-orbit servicing: Inspection repair refuel upgrade and assembly of satellites in space. *The Aerospace Corporation, report*, page 25, 2019.

[9] Xi Lun Ding, Ye Cong Wang, Yao Bing Wang, and Kun Xu. A review of structures, verification, and calibration technologies of space robotic systems for on-orbit servicing. *Science China Technological Sciences*, 64:462–480, 2021.

[10] Evangelos Papadopoulos, Farhad Aghili, Ou Ma, and Roberto Lampariello. Robotic manipulation and capture in space: A survey. *Frontiers in Robotics and AI*, 8, 7 2021.

[11] V.V. Svotina and M.V. Cherkasova. Space debris removal - Review of technologies and techniques. Flexible or virtual connection between space debris and service spacecraft. *Acta Astronautica*, 3 2022.

[12] Federico Basana and Francesco Branz. Simulation of robotic space operations with minimum base reaction manipulator. *Journal of Space Safety Engineering*, 9:440–448, 9 2022.

[13] Bruce A. Aikenhead, Robert G. Daniell, and Frederick M. Davis. Canadarm and the space shuttle. *Journal of Vacuum Science & Technology A*, 1(2):126–132, 1983.

[14] Yaobing Wang. Current state of space robots. In *Space Robotics*, pages 345–352. Springer Singapore, Singapore, 2021.

[15] C. Sallaberger. Canadian space robotic activities. *Acta Astronautica*, 41:239–246, 1997.

[16] Patten Laryssa, Evans Lindsay, Oshinowo Layi, Ochisor Marius, Kazuharu Nara, Lodewijk Aris, and Tabarah Ed. International Space Station robotics: a comparative study of ERA, JEMRMS and MSS. In *7th ESA Workshop on Advanced Space Technologies for Robotics and Automation*, pages 19–21, 2002.

[17] G. Gibbs and S. Sachdev. Canada and the International Space Station program: overview and status. *Acta Astronautica*, 51 (1-9):591–600, 2002.

[18] Canadian Space Agency and NASA. Canadarm, Canadarm2, and Canadarm3 – A comparative table. www.asc-csa.gc.ca [Online; modified on 2019-05-20].

[19] Naoki Sato and Yasufumi Wakabayashi. JEMRMS Design Features and Topics from Testing. In *6th International Symposium on Artificial Intelligence and Robotics & Automation in Space: i-SAIRAS*, 2001.

[20] Japan Aerospace Exploration Agency. Japanese Experiment Module Remote Manipulator System. https://iss.jaxa.jp [Online; Last Updated: August 29, 2008].

[21] European Space Agency. European Robotic Arm. www.esa.int [Online; Last Accessed: March, 2023].

[22] Kazuya Yoshida. Engineering Test Satellite VII Flight Experiments for Space Robot Dynamics and Control: Theories on Laboratory Test Beds Ten Years Ago, Now in Orbit. *The International Journal of Robotics Research*, 22(5):321–335, 2003.

[23] Robert B. Friend. Orbital Express program summary and mission overview. In Richard T. Howard and Pejmun Motaghedi, editors, *Sensors and Systems for Space Applications II*, volume 6958, page 695803. International Society for Optics and Photonics, SPIE, 2008.

[24] Thomas Debus and Sean Dougherty. Overview and Performance of the Front-End Robotics Enabling Near-Term Demonstration (FREND) Robotic Arm. In *AIAA Infotech@Aerospace Conference*, 2009.

[25] Carl Glen Henshaw. The DARPA Phoenix Spacecraft Servicing Program: Overview and Plans for Risk Reduction. In *Proceedings of International Symposium on Artificial Intelligence, Robotics and Automation in Space (i-SAIRAS)*, 2014.

[26] D. Reintsema, J. Thaeter, A. Rathke, W. Naumann, P. Rank, and J. Sommer. DEOS – the German robotics approach to secure and de-orbit malfunctioned satellites from low earth orbits. In *Proceedings of the i-SAIRAS*, pages 244–251. Japan Aerospace Exploration Agency (JAXA) Japan, 2010.

[27] NASA's Goddard Space Flight Center. NASA's Robotic OSAM-1 Mission Completes its Critical Design Review. www.nasa.gov [Online; Last Updated: Dec 21, 2022].

[28] NASA. OSAM-1 Mission. nexis.gsfc.nasa.gov/osam-1 [Online; Last Accessed: June, 2023].

[29] Josep Virgili-Llop and Marcello Romano. Simultaneous capture and detumble of a resident space object by a free-flying spacecraft-manipulator system. *Frontiers in Robotics and AI*, 6, 2019.

[30] Giulia E. Fenci and Neil G.R. Currie. Deployable structures classification: A review. *International Journal of Space Structures*, 32:112–130, 2017.

[31] Christopher H.M Jenkins. *Gossamer Spacecraft: Membrane And Inflatable Structures Technology For Space Applications*. American Institute of Aeronautics and Astronautics, Inc., 2001.

[32] Patrick K. Malone and Geoffrey T. Williams. Lightweight inflatable solar array. *Journal of Propulsion and Power*, 12(5):866–872, 1996.

[33] D. Cadogan, C. Sandy, and M. Grahne. Development and evaluation of the mars pathfinder inflatable airbag landing system. *Acta Astronautica*, 50(10):633–640, 2002.

[34] Aman Chandra and Jekanthan Thangavelautham. Modular inflatable composites for space telescopes. In *2019 IEEE Aerospace Conference*, pages 1–9, 2019.

[35] R.E. Freeland, G.D. Bilyeu, G.R. Veal, M.D. Steiner, and D.E. Carson. Large inflatable deployable antenna flight experiment results. *Acta Astronautica*, 41(4-10):267–277, 1997.

[36] Horacio de la Fuente, Jasen Raboin, Gerard Valle, and Gary Spexarth. TransHab - NASA's large-scale inflatable spacecraft. In *41st Structures, Structural Dynamics, and Materials Conference and Exhibit*, 2000.

[37] Sierra Space. Large Integrated Flexible Environment. sierraspace.com [Online; Last Accessed: March, 2023].

[38] L. Puig, A. Barton, and N. Rando. A review on large deployable structures for astrophysics missions. *Acta Astronautica*, 67:12–26, 7 2010.

[39] Yaobing Wang. Future prospects of space robots. In *Space Robotics*, pages 354–356. Springer Singapore, Singapore, 2021.

[40] Josie Hughes, Utku Culha, Fabio Giardina, Fabian Guenther, Andre Rosendo, and Fumiya Iida. Soft manipulators and grippers: A review. *Frontiers in Robotics and AI*, 3, 2016.

[41] Siddharth Sanan, Justin B. Moidel, and Christopher G. Atkeson. Robots with inflatable links. *2009 IEEE/RSJ International Conference on Intelligent Robots and Systems, IROS 2009*, pages 4331–4336, 2009.

[42] Xiang Zhang, Zhuoqun Liu, Hongwei Liu, Lu Cao, Xiaoqian Chen, and Yiyong Huang. Design and experiment of a foldable pneumatic soft manipulator. In Haibin Yu, Jinguo Liu, Lianqing Liu, Zhaojie Ju, Yuwang Liu, and Dalin Zhou, editors, *Intelligent Robotics and Applications*, pages 183–192, Cham, 2019. Springer International Publishing.

[43] Ryuma Niiyama, Young ah Seong, Yoshihiro Kawahara, and Yasuo Kuniyoshi. Blower-powered soft inflatable joints for physical human-robot interaction. *Frontiers in Robotics and AI*, 8, 2021.

[44] XueAi Li, Honghao Yue, Dapeng Yang, Kui Sun, and Hong Liu. A large-scale inflatable robotic arm toward inspecting sensitive environments: Design and performance evaluation. *IEEE Transactions on Industrial Electronics*, 70(12):12486–12499, 2023.

[45] Charles M. Best, Joshua P. Wilson, and Marc D. Killpack. Control of a pneumatically actuated, fully inflatable, fabric-based, humanoid robot. In *2015 IEEE-RAS 15th International Conference on Humanoid Robots (Humanoids)*, pages 1133–1140, 2015.

[46] Agostino Stilli, Helge A. Wurdemann, and Kaspar Althoefer. A novel concept for safe, stiffness-controllable robot links. *Soft Robotics*, 4(1):16–22, 2017. PMID: 29182102.

[47] Christoph H. Belke, Kevin Holdcroft, Alexander Sigrist, and Jamie Paik. Morphological flexibility in robotic systems through physical polygon meshing. *Nature Machine Intelligence*, 2023.

[48] MacDonald Dettwiler Space and Advanced Robotics Ltd. The Shuttle Remote Manipulator System – The Canadarm. https://ewh.ieee.org/reg/7/index.htm [Online; Last accessed May, 2023].

[49] Arianespace. Vega. arianespace.com/vehicle/vega [Online; Last Accessed: June, 2023].

[50] Our World in Data. Cost of space launches to low Earth orbit. ourworldindata.org [Online; Last Accessed: June, 2023].

[51] Pierpaolo Palmieri, Matteo Gaidano, Andrea Ruggeri, Laura Salamina, Mario Troise, and Stefano Mauro. An Inflatable Robotic Assistant for Onboard Applications. *Proceedings of the International Astronautical Congress, IAC*, A5:25–29, 2021.

[52] European Cooperation for Space Standardization. ECSS-E-HB-11A – Technology readiness level (TRL) guidelines (1 March 2017).

[53] Pierpaolo Palmieri, Matteo Gaidano, Mario Troise, Laura Salamina, Andrea Ruggeri, and Stefano Mauro. A deployable and inflatable robotic arm concept for aerospace applications. *2021 IEEE International Workshop on Metrology for AeroSpace, MetroAeroSpace 2021 - Proceedings*, pages 453–458, 2021.

[54] ESA. Flexible Storage Solutions for Human Spaceflight Activities. esa.int [Online; Published: February, 2023].

[55] Mark Schenk, Andrew D. Viquerat, Keith A. Seffen, and Simon D. Guest. Review of inflatable booms for deployable space structures: Packing and rigidization. *Journal of Spacecraft and Rockets*, 51(3):762–778, 2014.

[56] Yasuyuki Miyazaki and Michiharu Uchiki. Deployment dynamics of inflatable tube. *43rd AIAA/ASME/ASCE/AHS/ASC Structures, Structural Dynamics, and Materials Conference*, 2002.

[57] Houfei Fang, Michael Lou, and John Hah. Deployment study of a self-rigidizable inflatable boom. *Journal of Spacecraft and Rockets*, 43(1):25–30, 2006.

[58] Gerard D. Valle, Doug Litteken, and Thomas C. Jones. *Review of Habitable Softgoods Inflatable Design, Analysis, Testing, and Potential Space Applications*. 2019.

[59] Kriss J. Kennedy. ISS TransHab: Architecture Description. In *International Conference On Environmental Systems*. SAE International, jul 1999.

[60] Kuraray. Vectran. vectranfiber.com [Online; Last Accessed: May, 2023].

[61] DuPont. Technical Guide for Kevlar Aramid Fiber. dupont.com [Online; Last Accessed: May, 2023].

[62] Livio Narici, Marco Casolino, Luca Di Fino, Marianna Larosa, Piergiorgio Picozza, Alessandro Rizzo, and Veronica Zaconte. Performances of Kevlar and Polyethylene as radiation shielding on-board the International Space Station in high latitude radiation environment. *Scientific Reports*, 7, 12 2017.

[63] Michel Lambert and Eberhard Schneider. Shielding against space debris. a comparison between different shields: The effect of materials on their performances. *International Journal of Impact Engineering*, 17(4):477–485, 1995. Hypervelocity Impact Proceedings of the 1994 Symposium.

[64] E. Beruto, R. Destefanis, M. Faraud, and P. Buchwald. Debris Shielding development for the Columbus Orbital Facility. In *2nd European Conference on Space Debris*, 1997.

[65] M Tanaka and Y Moritaka. Single bumper shields based on vectran fibers. *Advances in Space Research*, 34(5):1076–1079, 2004. Space Debris.

[66] J. Hinkle, Anshu Dixit, John K.H. Lin, Karen Whitley, Judith Watson, and Gerard Valle. Design development and testing for an expandable lunar habitat. *Space 2008 Conference*, 2008.

[67] S.L. Veldman. *Design and Analysis Methodologies for Inflated Beams*. PhD thesis, Technische Universiteit Delft, 2005.

[68] M. Stein and J. Hedgepeth. Analysis of partly wrinkled membranes. *NASA TN D-2456*, 1961.

[69] C. Wielgosz and J.C. Thomas. Deflections of inflatable fabric panels at high pressure. *Thin-Walled Structures*, 40(6):523–536, 2002.

[70] L. G. Brazier. On the Flexure of Thin Cylindrical Shells and Other "Thin" Sections. *Proceedings of the Royal Society of London Series A*, 116(773):104–114, September 1927.

[71] George W. Zender. The bending strength of pressurized cylinders. *Journal of the Aerospace Sciences*, 29:362–363, 3 1962.

[72] I Weingarten, V, P. Seide, and J. P. Peterson. Buckling of Thin-Walled Circular Cylinders. *NASA-SP-8007*, 1968.

[73] S. L. Veldman, O. K. Bergsma, and A. Beukers. Bending of anisotropic inflated cylindrical beams. *Thin-Walled Structures*, 43:461–475, 2005.

[74] J. D. Wood. The flexure of a uniformly pressurized, circular, cylindrical shell. *Journal of Applied Mechanics*, 25:453–458, 1958.

[75] M. Baruch, J. Arbocz, and Zhang G.Q. Imperfection sensitivity of the Brazier effect for orthotropic cylindrical shells. *Delft University of Technology: Report LR-687*, 1992.

[76] S. L. Veldman. Wrinkling prediction of cylindrical and conical inflated cantilever beams under torsion and bending. *Thin-Walled Structures*, 44:211–215, 2006.

[77] A. Le Van and C. Wielgosz. Bending and buckling of inflatable beams: Some new theoretical results. *Thin-Walled Structures*, 43:1166–1187, 2005.

[78] G. R. Cowper. The Shear Coefficient in Timoshenko's Beam Theory. *Journal of Applied Mechanics*, 33(2):335–340, 06 1966.

[79] Andreas Öchsner. Timoshenko beam theory. In *Classical Beam Theories of Structural Mechanics*, pages 67–104. Springer International Publishing, Cham, 2021.

[80] Giancarlo Genta. The Finite Element Method. In *Vibration Dynamics and Controls*, volume 57. Springer New York, NY, 2009.

[81] S. Miller, T. Soares, Y. Van Weddingen, and J. Wendlandt. Modeling Flexible Bodies with Simscape Multibody Software, An Overview of Two Methods for Capturing the Effects of Small Elastic Deformations. *Technical Paper*, 2017.

[82] Dipendra Subedi, Ilya Tyapin, and Geir Hovland. Modeling and analysis of flexible bodies using lumped parameter method. In *2020 IEEE 11th International Conference on Mechanical and Intelligent Manufacturing Technologies (ICMIMT)*, pages 161–166, 2020.

[83] L. L. Howell, A. Midha, and T. W. Norton. Evaluation of Equivalent Spring Stiffness for Use in a Pseudo-Rigid-Body Model of Large-Deflection Compliant Mechanisms. *Journal of Mechanical Design*, 118(1):126–131, 03 1996.

[84] Ashok Midha, Larry L Howell, and Tony W Norton. Limit positions of compliant mechanisms using the pseudo-rigid-body model concept. *Mechanism and Machine Theory*, 35(1):99–115, 2000.

[85] Venkatasubramanian Kalpathy Venkiteswaran and Hai-Jun Su. A parameter optimization framework for determining the pseudo-rigid-body model of cantilever-beams. *Precision Engineering*, 40:46–54, 2015.

[86] Roman Vetter, Norbert Stoop, Falk K. Wittel, and Hans J. Herrmann. Simulating thin sheets: Buckling, wrinkling, folding and growth. *Journal of Physics: Conference Series*, 487, 2014.

[87] Anh Le van and Christian Wielgosz. Finite element formulation for inflatable beams. *Thin-Walled Structures*, 45:221–236, 2007.

[88] Roy R. Craig and Mervyn C.C. Bampton. Coupling of substructures for dynamic analyses. *AIAA Journal*, 6(7):1313–1319, 1968.

[89] Alessandro De Luca and Wayne Book. Robots with flexible elements. In Bruno Siciliano and Oussama Khatib, editors, *Springer Handbook of Robotics*, pages 287–319. Springer Berlin Heidelberg, Berlin, Heidelberg, 2008.

[90] Rafael Munoz-Salinas. Aruco: a minimal library for augmented reality applications based on opencv. *Universidad de Córdoba*, 386, 2012.

[91] João Oliveira, Afonso Ferreira, and João C.P. Reis. Design and experiments on an inflatable link robot with a built-in vision sensor. *Mechatronics*, 65:102305, 2020.

[92] S. Y. Chen. Kalman Filter for Robot Vision: A Survey. *IEEE Transactions on Industrial Electronics*, 59(11):4409–4420, 2012.

[93] Pierpaolo Palmieri, Matteo Melchiorre, Leonardo Sabatino Scimmi, Stefano Pastorelli, and Stefano Mauro. Human Arm Motion Tracking by Kinect Sensor Using Kalman Filter for Collaborative Robotics. In Vincenzo Niola and Alessandro Gasparetto, editors, *Advances in Italian Mechanism Science*, pages 326–334, Cham, 2021. Springer International Publishing.

[94] Mario Troise, Matteo Gaidano, Pierpaolo Palmieri, and Stefano Mauro. Preliminary Analysis of a Lightweight and Deployable Soft Robot for Space Applications. *Applied Sciences*, 11:2558, 2021.

[95] François Chaumette. Visual servoing. In Marcelo H. Ang, Oussama Khatib, and Bruno Siciliano, editors, *Encyclopedia of Robotics*, pages 1–9. Springer Berlin Heidelberg, Berlin, Heidelberg, 2020.

[96] Tomáš Hodaň, Martin Sundermeyer, Bertram Drost, Yann Labbé, Eric Brachmann, Frank Michel, Carsten Rother, and Jiří Matas. Bop challenge 2020 on 6d object localization. In Adrien Bartoli and Andrea Fusiello, editors, *Computer Vision – ECCV 2020 Workshops*, pages 577–594, Cham, 2020. Springer International Publishing.

[97] Matteo Melchiorre, Leonardo Sabatino Scimmi, Stefano Mauro, and Stefano Paolo Pastorelli. Vision-based control architecture for human–robot hand-over applications. *Asian Journal of Control*, 23(1):105–117, 2021.

[98] Fangli Mou, Hao Ren, Bin Wang, and Dan Wu. Pose estimation and robotic insertion tasks based on yolo and layout features. *Engineering Applications of Artificial Intelligence*, 114:105164, 2022.

[99] Andreas ten Pas, Marcus Gualtieri, Kate Saenko, and Robert Platt Jr. Grasp pose detection in point clouds. *CoRR*, abs/1706.09911, 2017.

[100] Pierpaolo Palmieri, Matteo Melchiorre, and Stefano Mauro. Design of a Lightweight and Deployable Soft Robotic Arm. *Robotics*, 11:88, 8 2022.

[101] Pierpaolo Palmieri, Mario Troise, Matteo Gaidano, Matteo Melchiorre, and Stefano Mauro. Inflatable Robotic Manipulator for Space Debris Mitigation by Visual Servoing. *2023 9th International Conference on Automation, Robotics and Applications, ICARA 2023*, page 175 – 179, 2023.

[102] Bruno Siciliano, Lorenzo Sciavicco, Luigi Villani, and Giuseppe Oriolo. Differential Kinematics and Statics. In *Robotics: Modelling, Planning and Control*, pages 105–160. Springer London, London, 2009.

[103] Yaobing Wang. Space robot perception system. In *Space Robotics*, pages 213–225. Springer Singapore, Singapore, 2021.

[104] Boyu Ma, Zainan Jiang, Yang Liu, and Zongwu Xie. Advances in space robots for on-orbit servicing: A comprehensive review. *Advanced Intelligent Systems*, n/a(n/a):2200397.

[105] A. Muis and K. Ohnishi. Eye-to-hand approach on eye-in-hand configuration within real-time visual servoing. *IEEE/ASME Transactions on Mechatronics*, 10(4):404–410, 2005.

[106] C. Marchionne, M. Sabatini, and P. Gasbarri. Gnc architecture solutions for robust operations of a free-floating space manipulator via image based visual servoing. *Acta Astronautica*, 180:218–231, 2021.

[107] Javier Pérez Alepuz, M. Reza Emami, and Jorge Pomares. Direct image-based visual servoing of free-floating space manipulators. *Aerospace Science and Technology*, 55:1–9, 2016.

[108] Jinhui Wu, Zhehao Jin, Andong Liu, Li Yu, and Fuwen Yang. A survey of learning-based control of robotic visual servoing systems. *Journal of the Franklin Institute*, 359(1):556–577, 2022.

[109] Abdulrahman Al-Shanoon and Haoxiang Lang. Robotic manipulation based on 3-d visual servoing and deep neural networks. *Robotics and Autonomous Systems*, 152:104041, 2022.

[110] Bo Chen, Jiewei Cao, Alvaro Parra, and Tat-Jun Chin. Satellite pose estimation with deep landmark regression and nonlinear pose refinement. In *2019 IEEE/CVF International Conference on Computer Vision Workshop (ICCVW)*, pages 2816–2824, 2019.

[111] Gabriele Biondi. *Fault-tolerant feature-based estimation of space debris motion and inertial properties*. PhD thesis, Politecnico di Torino, 2017.

[112] Josep Virgili-Llop, Costantinos Zagaris, II Richard Zappulla, Andrew Bradstreet, and Marcello Romano. A convex-programming-based guidance algorithm to capture a tumbling object on orbit using a spacecraft equipped with a robotic manipulator. *The International Journal of Robotics Research*, 38(1):40–72, 2019.

[113] Raymond Kristiansen and David Hagen. Modelling of actuator dynamics for spacecraft attitude control. *Journal of Guidance, Control, and Dynamics*, 32(3):1022–1025, 2009.